

EXPERIMENTAL STUDY OF A TRANSCRITICAL THERMOACOUSTIC ENGINE WITH POWER EXTRACTION APPLICATIONS

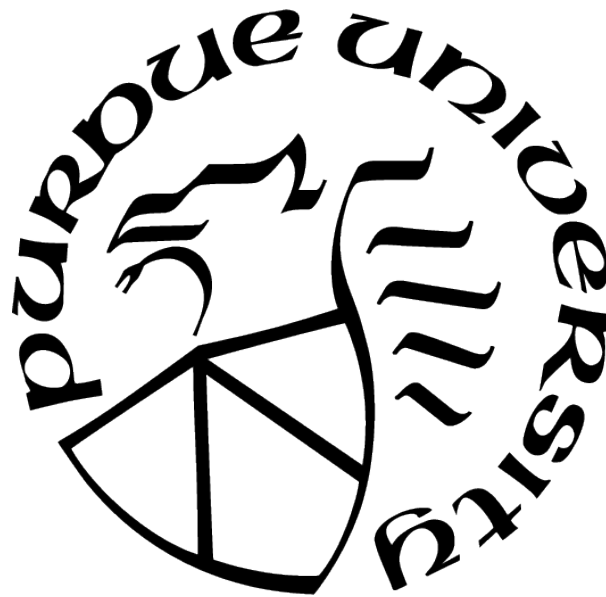
by
Benjamin Kuras

A Thesis

Submitted to the Faculty of Purdue University

In Partial Fulfillment of the Requirements for the degree of

Master of Science in Aeronautics and Astronautics



School of Aeronautics and Astronautics

West Lafayette, Indiana

May 2021

**THE PURDUE UNIVERSITY GRADUATE SCHOOL
STATEMENT OF COMMITTEE APPROVAL**

Dr. Stephen Heister, Chair

School of Aeronautics and Astronautics

Dr. Carlo Scalò

School of Mechanical Engineering

Dr. Carson Slabaugh

School of Aeronautics and Astronautics

Approved by:

Dr. Gregory Blaisdell

ACKNOWLEDGMENTS

I would like to thank Dr. Scalo and Dr. Migliornio for helping me understand the concepts behind this project and for providing their insight into my results. I would also like to thank Karl Jantze and Ariana Martinez for welcoming me to Zucrow labs and for their help in understanding how to use and modify the existing experiment. Finally, I would like to thank Dr. Heister, I am incredibly grateful for his guidance through this project and am lucky to have him as my advisor.

TABLE OF CONTENTS

LIST OF TABLES	6
LIST OF FIGURES	7
LIST OF SYMBOLS	11
ABBREVIATIONS	13
ABSTRACT	14
1 INTRODUCTION	15
1.1 Motivation	16
1.2 Literature Review	16
1.2.1 History of Thermoacoustics	16
1.2.2 Recent Work in Thermoacoustics	22
1.2.3 Previous Work in Thermoacoustics with R-218	25
1.2.4 Energy Extraction via Turbines	27
1.3 Document Overview	34
2 EXPERIMENTAL FACILITY	36
2.1 Experimental Objectives	36
2.2 Experimental Design	37
2.2.1 System Overview	37
2.3 Changes Made to the Experimental Setup	44
2.3.1 Removing Coils from the Resonator	45
2.3.2 Adding Functionality to Support Varying Resonator Diameter	48
2.4 Instrumentation	51
2.4.1 Uncertainty Analysis	53
3 EXPERIMENTAL RESULTS	56
3.1 Testing and Analysis Methods	56

3.2	Study on Repeatability of Previous Results	58
3.2.1	Repeatability of Results	59
3.2.2	Waveform Comparison	60
3.3	Parametric Study on Resonator 2 Length and Diameter	62
3.3.1	Condition Repeatability	62
3.3.2	Influence of Resonator Length and Diameter	65
3.3.3	Influence of Coils	67
3.4	Leak Rate Analysis	68
4	BIDIRECTIONAL TURBINE DESIGN	73
4.1	Motivation	73
4.2	Preliminary Analyses	73
4.3	Turbine Design Case Study	80
4.4	Mechanical Design	82
4.5	Proposed Experiment	91
5	CONCLUSION	93
5.1	Project Summary	93
5.1.1	Testing Results	93
5.1.2	Turbine Design	94
5.2	Future Work	95
5.2.1	Bi-Directional Turbine Testing	95
5.2.2	Direct Measurement of Acoustic Power	95
5.3	Lessons Learned	96
	REFERENCES	97
A	APPENDIX	101

LIST OF TABLES

2.1	Critical Conditions of R-218 from the National Institute of Standards and Technology (NIST)	36
2.2	Rig Dimensions	45
2.3	Pressure Transducer Location for Each Resonator 2 Length Tested	47
2.4	Uncertainty Confidence Intervals	54
2.5	Measurement Uncertainty	55
3.1	Test Campaign Summary	56
3.2	Repeatability Campaign Test Conditions	58
3.3	Percent Variance of Test Conditions from the Target Value in the Repeatability Study	59
3.4	Parametric Study on Resonator Length and Diameter Test Conditions	62
3.5	Percent Variance of Test Conditions from the Target Value in the Resonator Length and Diameter Study	63
4.1	Timmer et al. Case Study Results	82
4.2	Fixed turbine parameters	85

LIST OF FIGURES

1.1	A Sondhauss tube consists of a tube closed at one end and filled with gas. The closed end is expose to a heat source. The temperature gradient constructed between the heat source and ambient gas temperature excites thermoacoustic oscillations in the tube which can be heard [4].	17
1.2	Similar to a Sondhauss tube, the Rijke tube excites thermoacoustic oscillations in a tube open at both ends by heating a metal or gauze mesh fixed in the bottom half of the tube. The heated mesh establishes a temperature gradient with the ambient air conditions and excites thermoacoustic oscillations [6].	18
1.3	A standing wave TAE consists of a tube closed on both ends containing a fluid. A heat exchanger and stack assembly impose a temperature gradient on the working fluid which excites thermoacoustic oscillations. A power extraction device may be attached to the engine to generate electricity.	19
1.4	A travelling wave TAE consists of the same basic parts as a standing wave engine, hot and cold heat exchangers which enclose, in this case, a regenerator, a modified and more efficient version of a stack. A power extraction device may be attached to the resonator to generate electricity.	21
1.5	Configuration of the coupled TAE and ICE system used in the Bou Nader et al. research. The TAE passes hot exhaust gas from the ICE to the hot heat exchanger. The cold heat exchanger takes in ambient air. The thermoacoustic response produced by the helium in the engine is used to generate electricity to charge the battery in the hybrid car, allowing the car to operate for longer durations on electricity, improving fuel efficiency [18].	24
1.6	Experimental configuration used by Alexander et al. [20].	25
1.7	The three stacks tested by Alexander et al. [20].	26
1.8	An OWC system diagram. (Left) Inflow diagram showing ocean waves flowing into the column and pushing air through the turbine out of the top of the column, driving the turbine. (Right) Outflow diagram showing ocean waves flowing out from the column, allowing air to enter through the top of the column, driving the turbine [23].	29
1.9	(Left) A wells turbine [24]. (Right) A bidirectional impulse turbine [25].	29
1.10	3D printed bidirectional impulse turbine used in the de Blok et al. experiments. A loudspeaker was used to excite acoustic pressure oscillations in air to drive the turbine [27].	31
1.11	Experimental results of de Blok's study show that bidirectional turbines perform well under high frequency conditions, achieving a maximum rotor efficiency of just over 30% at 20Hz [27].	32

1.12	Predicted rotor efficiency as a function of working fluid density [27].	33
1.13	Bidirectional impulse turbine used in the experiments of Timmer and van der Meer [28].	34
2.1	Plumbing and Instrumentation Diagram of the experimental setup. Purple represents R-218 flowpaths, green represents nitrogen, red represents Duratherm G heat transfer fluid, and blue represents water. The Coriolis flow meter (CFM-TA-01) is optional hardware not employed in this work [21].	38
2.2	R-218 storage tanks.	39
2.3	R-218 loading/reclamation pump and vacuum pump.	39
2.4	Nitrogen bladder accumulator.	40
2.5	Heat exchanger support hardware.	41
2.6	Schematic of the thermoacoustic engine [21].	41
2.7	A computer aided design (CAD) image of the thermoacoustic engine before changes were made. The test section consists of two major components: the heat exchanger, and resonator section [21].	42
2.8	A CAD image of the heat exchanger designed in conjunction with Mezzo Technologies. The cross-section on the left shows the microtube stack with sealing and mounting hardware. The right image shows fluid and instrumentation connections on the heat exchanger exterior [21].	44
2.9	Rig with new height modification. The total height of the unistrut support is 75in. The red lines indicate the lengths at which the rig was tested.	46
2.10	CAD image from Parker Hannifin of 6-4 F5OLO-SS fitting used to adapt to the new tube diameter. Each image shows the fitting from a different angle.	49
2.11	6-4 F5OLO-SS fitting installed on the rig.	49
2.12	A CAD image from Parker Hannifin of the 6-4 LOHL6-S ZJ fitting used to adapt to the new tube diameter. Each image shows the fitting from a different angle.	50
2.13	6-4 LOHL6-S ZJ Installed in a DPT assembly.	51
2.14	LabVIEW VI used to record and observe data during testing [21]	52
3.1	Location of each pressure transducer measured from the top of the hot side cavity [21].	61

3.2	Comparison between (left) waveform from current testing at various pressures and a temperature difference of 79K compared to (right) waveform from Martinez's testing at various pressures and a temperature difference of 79K [21]. The x axis shows each pressure transducer's location along the rig normalized by the rig length $L = 239\text{cm}$. The y axis shows average steady-state pressure amplitude as measured by each instrument. A bulk pressure trend is not included on the left plot because there is not enough data to establish a trend in bulk pressure. . . .	61
3.3	Waveform from tests with coils in resonator 2. The case shown is from a test at a temperature difference of 79K, and a bulk pressure over critical pressure of 1.13. The top-left insert shows the power spectral density plot of the test, red lines indicate the range of the bandpass filter. The bottom-left insert shows a zoomed in picture of the waveform [32].	63
3.4	Typical waveform from tests without coils in resonator 2. This test was performed at bulk pressure over critical pressure of 1.11, a temperature difference of 100K, resonator 2 length of 1.78m, and resonator 2 diameter of 0.704cm. These plots illustrate the typical bandpass filtered waveform and power spectral density plots obtained from the Kulite pressure sensor on the hot-side cavity.	64
3.5	Frequency and average steady-state pressure amplitude for (a) a temperature difference of 80K, and bulk over critical pressure of 1.1, (b) a temperature difference of 100K, and bulk over critical pressure of 1.1, and (c) a temperature difference of 120K, and bulk over critical pressure of 1.1. Both quantities are plotted against resonator diameter and line markers indicate total rig length. Average steady-state pressure amplitude increasing as total rig length increases and decreasing as resonator 2 diameter increases. Operational frequency decreases as total rig length increases and increases as resonator 2 diameter increases [32].	65
3.6	(a) Pressure amplitude and (b) frequency measured in resonator 2 with and without coils. All tests were conducted at bulk over critical pressure of 1.1 and a temperature difference of approximately 118K. The rig without coils produces a higher pressure amplitude across all resonator lengths while exhibiting only a minor decrease in operational frequency [32]	67
3.7	Comparison of pressure traces between (a) test 66, conducted at a bulk over critical pressure of 1.09 and a temperature difference of 116K with coils in resonator 2, and (b) test 49, conducted at a bulk over critical pressure of 1.1 and a temperature difference of 120K. Solid lines depict raw data translated to be centered around zero. Dashed lines represent bandpass filtered data [32].	68
3.8	Pressure trace of long duration test. Up to 1500 seconds, the rig is being heated to excite thermoacoustic instabilities. The standing wave valves are closed at 1250 seconds, isolating the rig from pressure supply, and the rig is allowed to operate for approximately an additional 30 minutes. Just past 3000 seconds, the valves are opened back up an the rig pressure comes back up to the supply pressure.	69

3.9	Density of R-218 at supercritical pressures and temperatures computed using the Peng-Robinson equation of state [32], [34].	70
3.10	Nitrogen pressure during the leak rate test. The nitrogen was pressurized to approximately 3000kPa and allowed to leak out for 30 hours.	72
4.1	Velocity triangles for an impulse turbine. For the bi-directional impulse turbine, the upstream and downstream stator are identical and mirrored about the vertical axis.	74
4.2	Rotor inlet angle as a function of stator exit angle. The relationship is weakly exponential with rotor inlet angle ranging between 10 and 20 degrees less than the stator exit angle.	77
4.3	Rotational speed as a function of stator exit angle. This trend is more strongly exponential than the rotor inlet angle trend.	78
4.4	Ratio of pressure drop over the turbine to the available thermoacoustic pressure amplitude. This trend is the most strongly exponential of the three presented. The separation between 50% and 75% pressure drop over available amplitude is only 2 degrees in stator exit angle.	80
4.5	Diagram of the velocity triangles used in the design of Timmer et al. The case presented here is for the maximum fluid velocity seen by the turbine, but the case study was performed for both the maximum velocity and the RMS velocity [28].	81
4.6	Turbine blade geometry definitions.	86
4.7	Turbine radial geometry definitions.	87
4.8	Moderate performance turbine design with $\alpha_1 = 65$ degrees.	88
4.9	High performance turbine design with $\alpha_1 = 75$ degrees.	89
4.10	Power generated by the turbine for a 2 1/2" schedule 40 pipe and an input velocity of 4.77m/s. The high performance turbine design generates 3 times more power than the moderate performance design, but has a 3 times higher pressure drop.	90
4.11	Proposed experimental design to test each turbine concept. The turbine will be installed in a tube filled with water, a piston will be used to simulate thermoacoustic pressure fluctuations, and a dynamometer will be used to measure the torque and speed of the shaft.	91

LIST OF SYMBOLS

ΔT	Temperature difference (K)
D_1	Diameter of the hot side cavity, heat exchangers, and stack (cm)
l_{cav}	Length of the hot side cavity (cm)
l_{HHX}	Length of the hot heat exchanger (cm)
l_{stk}	Length of the stack (cm)
l_{CHX}	Length of the cold heat exchanger (cm)
D_2	Diameter of resonator section 2 (cm)
l_{res2}	Length of resonator section 2 (cm)
l_{res3}	Length of resonator section 3 (cm)
D_3	Diameter of resonator section 3 (cm)
U_r	Uncertainty interval
B_r	Bias interval
P_r	Precision interval
$\sigma_{\bar{x}_i}$	Standard deviation of a set
n	Number of samples
f	Frequency (Hz)
P	Pressure (kPa, psi)
$\frac{P}{P_{cr}}$	Bulk pressure over critical pressure
C	Relative percent difference
x_e	Experimental value
x_t	Target value
P_{max}	Maximum pressure amplitude (kPa, psi)
L	Rig length (cm)
a	Speed of sound (m/s)
$\frac{A_{res2}}{A_{res3}}$	Area ratio between resonator 2 and resonator 3
ρ	Density (kg/m^3)
V	Volume (m^3)
c_i	Absolute flow velocity at station i (m/s)

$c_{\theta i}$	Tangential component of absolute flow velocity at station i (m/s)
w_i	Relative flow velocity at station i (m/s)
U	Rotor tip speed (m/s)
α_i	Absolute flow angle at station i (deg)
β_i	Relative flow angle at station i (deg)
ϕ	Flow coefficient
N	Rotor speed (RPM)
r_{tip}	Turbine tip diameter (m)
$\frac{\Delta P}{P}$	Turbine pressure drop over pressure amplitude
\mathbb{P}	Power (W)
\dot{m}	Mass flow rate (kg/s)
r_{hub}	Turbine hub diameter (m)
b	Rotor blade height (m)
D_R	Mean turbine diameter (m)
S_r	Turbine blade pitch (m)
z	Number of rotor blades
l_r	Chord length of rotor blades (m)
r_g	Stator curvature radius (m)
l_g	Stator length (m)
A_{tube}	Tube area (m^2)
$A_{annulus}$	Area of the annulus between turbine hub and tube wall (m^2)
ΔP_{hub}	Pressure drop due to fluid acceleration over turbine hub (kPa, psi)

ABBREVIATIONS

TAE	Thermoacoustic Engine
R-218	Octafluoropropane
UTC	Rolls-Royce University Technology Center
TTE	Transcritical Thermoacoustic Engine
ICE	Internal Combustion Engine
OWC	Oscillating Water Column
RPM	Revolutions per Minute
NIST	National Institute of Standards and Technology
P&ID	Plumbing and Instrumentation Diagram
CAD	Computer Aided Design
DPT	Differential Pressure Transducer
PTFE	Polytetrafluoroethylene
OD	Outer Diameter
ID	Inner Diameter
PVC	Polyvinyl Chloride
DAQ	Data Acquisition System
FSO	Full Spectrum Operation
EPA	Environmental Protection Agency
RMS	Root-Mean-Square

ABSTRACT

Kuras, Benjamin M.S., Purdue University, April 2021. Experimental Study of a Transcritical Thermoacoustic Engine with Power Extraction Applications. Major Professor: Dr. Stephen D. Heister.

An experimental study was performed on a low frequency transcritical thermoacoustic engine developed at Maurice J. Zucrow Laboratories. The goal of the experiment was to characterize the effects of engine geometry on the thermoacoustic production of the working fluid and to use insights gained to design a power extraction device for the transcritical thermoacoustic engine. The effects of geometry were investigated by parametrically varying the length of the resonator and the diameter of the resonator and measuring the pressure amplitude and frequency of thermoacoustic instabilities developed at varying ΔT and one bulk pressure of $\frac{P}{P_{cr}} = 1.1$. It was found that increasing resonator length increases pressure amplitude, decreases frequency, and increases acoustic power developed. Increasing resonator diameter decreases pressure amplitude, increases frequency, and increases acoustic power developed. It was also experimentally proven that coiled tube sections in the resonator attenuate the thermoacoustic pressure wave. After testing, the knowledge gained was applied to the design of a bidirectional impulse turbine for eventual integration into a scaled-up version of the current thermoacoustic engine to be used to extract power from the thermoacoustic instabilities developed in the rig.

1. INTRODUCTION

The phenomena of thermoacoustic oscillations has been an area of research interest for over 200 years. From the first publication of the phenomena by Byron Higgins in 1802 [1], to the research being performed today, the field has developed significantly.

The field of thermoacoustics involves the study of the interaction between pressure, temperature, and density variations in acoustic waves. Thermoacoustic instabilities occur spontaneously when a fluid is exposed to a sufficient temperature gradient and is under enough pressure. Over the life of the field of study, a significant body of work has been developed on how to harness thermoacoustic instabilities where they are wanted and how to mitigate them where they are unwanted.

Harnessing the power developed by thermoacoustic oscillations using a thermoacoustic engine (TAE) has significant appeal over other methods of power generation because TAEs do not require significant numbers of moving parts, so their maintenance requirements are low.

This research intends to optimize a previous TAE geometry to obtain maximum performance from the chosen working fluid, octafluoropropane (R-218) under transcritical pressure and temperature conditions, and to use insights gained from this study and others to develop an energy extraction device for eventual integration into the TAE. Until the research group at Purdue University took up this project, no publicly available research had been published on TAEs using transcritical fluids as the working fluid. Transcritical fluids provide significant advantages over commonly used thermoacoustic working fluids such as helium because of their density is quite sensitive to temperature changes.

Section 1.1 presents the motivation for the research being performed, and section 1.2 reviews currently available literature on the history of and recent work in thermoacoustics, and discusses literature on energy extraction from TAEs via turbines. Finally, section 1.3 presents an overview of the topics that will be covered in this document.

1.1 Motivation

In 2017, the Rolls-Royce University Technology Center (UTC) for Advanced Thermal Management sponsored a project aimed at exploring new methods for thermal management in aircraft engines. Several graduate students at Purdue contributed to research aimed at developing a method for utilizing waste heat to excite thermoacoustic instabilities in transcritical fluids and extract work from the phenomenon. After some study, it became clear that the current iteration of the transcritical thermoacoustic engine (TTE) was not ideal for integration into aircraft systems and subsequently, Rolls-Royce decided to move on from the project. The team at Purdue has pivoted to developing the TTE for use in other waste heat extraction applications, namely in power plants.

1.2 Literature Review

This literature review will give a brief description of the history and give background on research in thermoacoustics including recent research in the field. Next, a description of the work performed at Purdue in thermoacoustics is presented. Finally, a discussion on energy extraction from thermoacoustic devices with a focus on bi-directional turbines is provided.

1.2.1 History of Thermoacoustics

The phenomenon of thermoacoustic oscillations was first scientifically documented in 1802 by Byron Higgins. Higgins burned hydrogen in a tube to produce an audible acoustic phenomena referred to as a “singing flame” [1], [2]. A similar phenomena to the singing flame is said to have been reported frequently by glass blowers when introducing a significant source of heat to a glass tube closed at one end. Sondhauss described the phenomenon reported by glass blowers in the German publication “Annals of Physics and Chemistry” in 1850 [3]. Subsequently, the phenomena of acoustic oscillations occurring in a tube heated and closed at one end is referred to as a “Sondhauss tube”. Figure 1.1 gives a basic diagram of a Sondhauss tube.

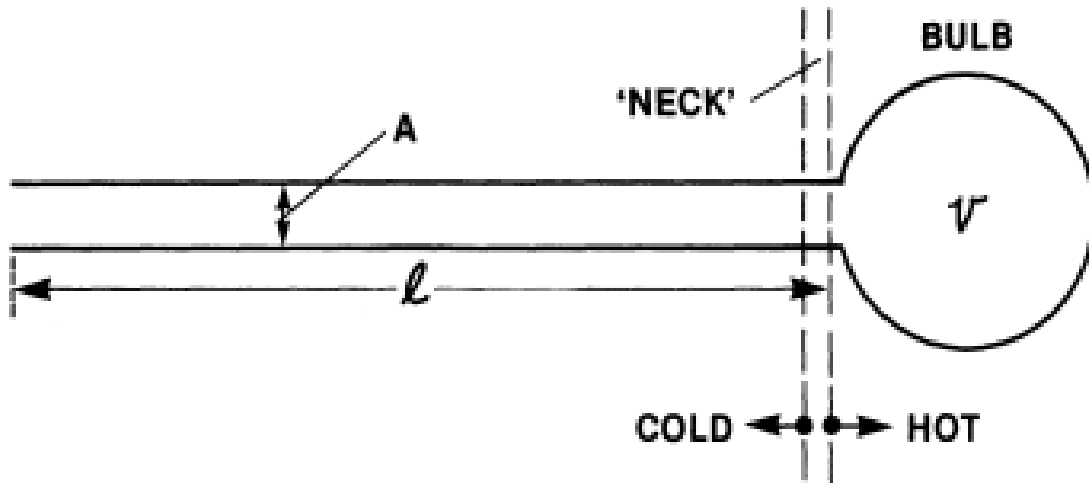


Figure 1.1. A Sondhauss tube consists of a tube closed at one end and filled with gas. The closed end is expose to a heat source. The temperature gradient constructed between the heat source and ambient gas temperature excites thermoacoustic oscillations in the tube which can be heard [4].

A similar phenomenon was experimentally recreated by Rijke in 1859 when he discovered thermoacoustic oscillations could be excited by heating a wire mesh fixed inside the bottom half a tube which is open at both ends, this experimental configuration is known as a “Rijke tube” [5]. Figure 1.2 shows a diagram of a Rijke tube.

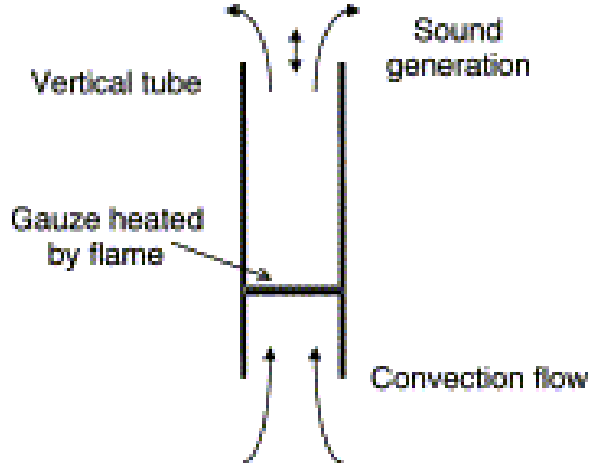


Figure 1.2. Similar to a Sondhauss tube, the Rijke tube excites thermoacoustic oscillations in a tube open at both ends by heating a metal or gauze mesh fixed in the bottom half of the tube. The heated mesh establishes a temperature gradient with the ambient air conditions and excites thermoacoustic oscillations [6].

Although Sondhauss and Rijke were able to experimentally recreate the thermoacoustic phenomenon in two separate ways, a proper explanation for the physical mechanisms which caused the thermoacoustic phenomenon was still missing.

In 1877, in his textbook on sound, Lord Rayleigh posed the first qualitative explanation of the phenomenon which occurs in a Sondhauss tube [7]. It would still be nearly 100 years from Rayleigh's first publication of *The Theory of Sound* before the first theoretical models of thermoacoustic oscillations would be developed.

In the meantime, more discoveries were being made in the field. Cryogenics researcher K. W. Taconis and his colleagues discovered that oscillations could be excited by introducing a hollow tube with one end at room temperature to a supply of liquid helium, this phenomenon would later be termed Taconis oscillations [8]. Research on thermoacoustic oscillations in cryogenic applications continued through into the 1950s where Clement and Gaffney discovered that the thermoacoustic oscillations caused by inserting a hollow tube into a cryogenic fluid could be used to measure the fluid level using the frequency and pressure amplitude of the oscillations [9], [10].

In another area of study, the inventor Warren Marrison patented a heat exchanger device which could be used to excite thermoacoustic oscillations [11]. Marrison proposed that a standing wave heat engine could be used to convert heat into electricity. A standing wave engine uses the basic principle that an acoustic wave trapped in a closed tube will have pressure oscillations which vary in time but not in space. Figure 1.3 shows a basic standing wave heat engine configuration. Although Marrison did not propose the use of a stack, many modern heat exchangers in thermoacoustic applications use a stack to improve heat exchanger performance. A stack, in this context, is a porous material which fluid flows through which allows the fluid to oscillate in contact with a solid wall, improving heat transfer into the fluid.

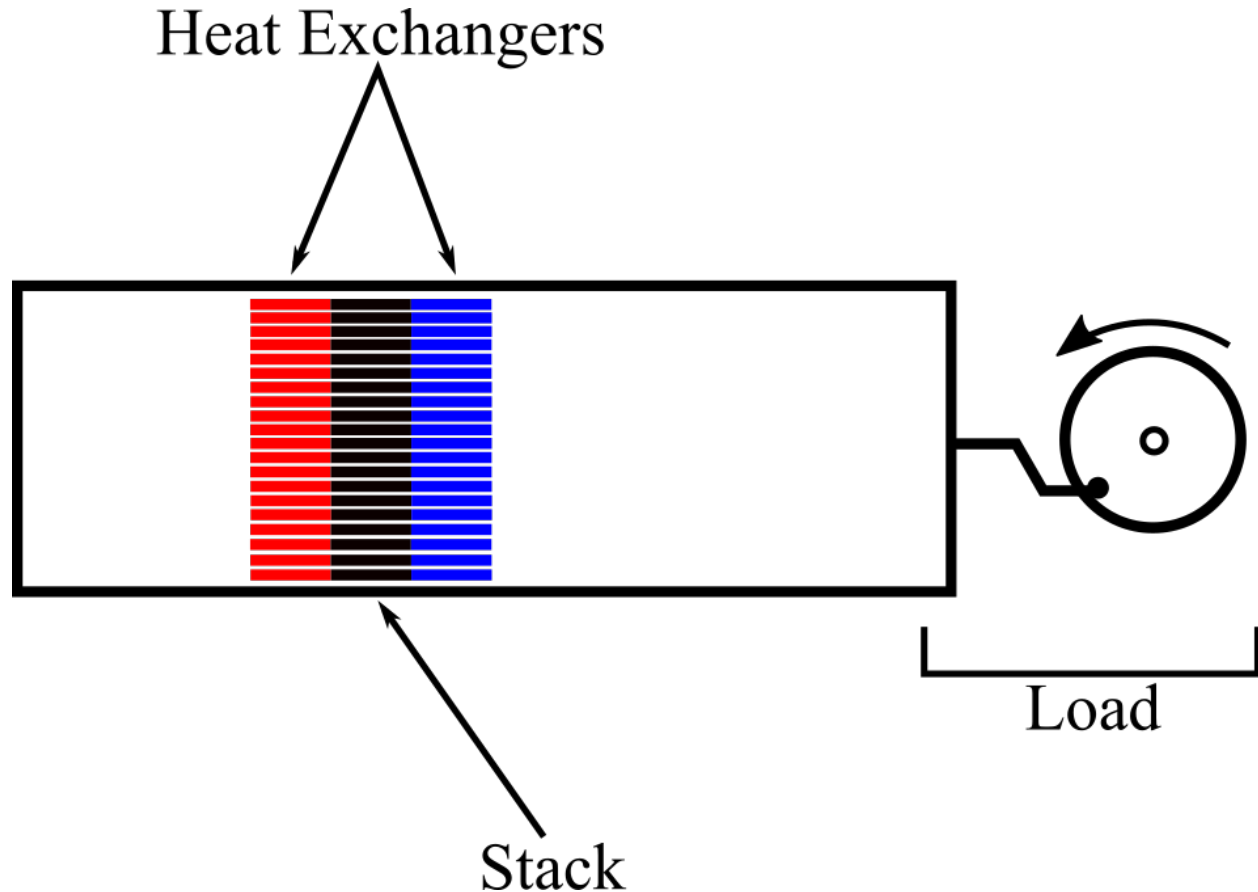


Figure 1.3. A standing wave TAE consists of a tube closed on both ends containing a fluid. A heat exchanger and stack assembly impose a temperature gradient on the working fluid which excites thermoacoustic oscillations. A power extraction device may be attached to the engine to generate electricity.

During the time after the publication of Lord Rayleigh's *The Theory of Sound*, there was significant work being done to theoretically model thermoacoustic oscillations. In 1980, Nikolaus Rott published his linear thermoacoustic theory in the 1980 edition of *Advances in Applied Mechanics* [12]. Rott's theory has become widely accepted as the basis for modeling thermoacoustic behavior.

In 1979, Ceperley began developing a new type of thermoacoustic heat engine using a travelling wave concept [13]. The travelling wave thermoacoustic engine uses a looped-tube configuration which allows pressure oscillations to vary in both time and space. The main appeal of a travelling wave engine is its significant advantage in energy efficiency over a standing wave engine. Figure 1.4 illustrates a basic travelling wave TAE.

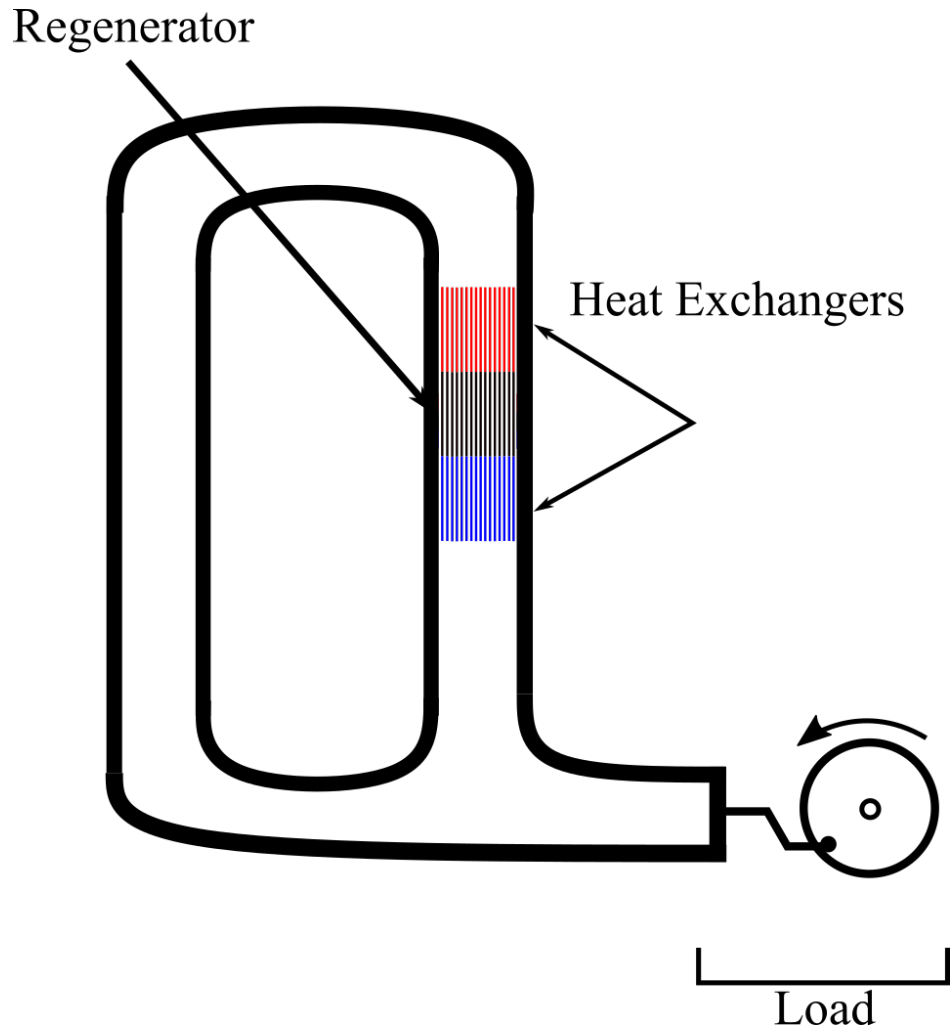


Figure 1.4. A travelling wave TAE consists of the same basic parts as a standing wave engine, hot and cold heat exchangers which enclose, in this case, a regenerator, a modified and more efficient version of a stack. A power extraction device may be attached to the resonator to generate electricity.

In 1999, Blackhaus and Swift had a breakthrough in travelling wave technology, demonstrating an efficiency of 30% in a travelling wave Stirling heat engine [14].

All of this research has set the stage for modern researchers to bring the field of thermoacoustics into the practical realm. A significant amount of effort is now being directed to optimizing both standing wave and travelling wave engine configurations and to developing methods to extract work from TAEs.

1.2.2 Recent Work in Thermoacoustics

Recent work in thermoacoustics is mainly focused on two areas, the optimization of TAE technology, and on the development of energy extraction methods for TAEs. The following section will present a sample of studies which were performed in the past few years focusing on the development of TAE technology and energy extraction technology.

In the area of engine optimization, significant effort is being put into refining TAE geometry. In 2018, Yang et al. investigated the effects of regenerator geometry on travelling wave engine performance. They used a looped travelling wave configuration similar to the one shown in Fig. 1.4. They developed a numerical model of a travelling wave regenerator to aid in design, designed five different regenerators, and tested them over a range of conditions. They determined optimal ranges for various regenerator design parameters to aid in designing a regenerator for low-grade heat recovery [15].

Significant work has also been done investigating the effect of different working fluids. In 2019, Dong et al. performed a study investigating the effects of helium, nitrogen, and argon on the performance of a thermoacoustic Stirling engine. They used a looped tube travelling wave configuration. They found that both nitrogen and argon are more useful for low pressure, low temperature conditions because they have relatively high onset temperatures, or the minimum temperature differential required to excite thermoacoustic instabilities in the fluid, and they found for nitrogen and argon, the onset temperature increases with pressure. They found that helium operates at almost three times the frequency as nitrogen and argon and that the pressure required to obtain minimum onset temperature is relatively moderate at around 1 MPa [16].

In 2020, Tan et al. conducted a similar study in a travelling wave engine investigating the effects of working fluid and some engine geometry. They designed a looped TAE with an air-cooled heat exchanger and tested the engine with carbon dioxide, nitrogen, argon, and helium. They concluded, in agreement with Dong et al., that for all fluids, there exists an optimum mean pressure where onset temperature is minimized and that helium achieves the highest performance [17].

Another major area of effort in thermoacoustics is energy extraction. A significant body of work has been developed on designing and optimizing thermoacoustic heat engines in both standing and travelling wave configurations, but the technologies for extracting work from the engines is still developing. At the moment, much of the work being done in thermoacoustic electricity generation is mathematical modeling, but a few experimental studies have been published in recent years.

Wissam Bou Nader et al. in 2020 proposed that integrating a TAE with an internal combustion engine (ICE) could improve the overall system efficiency of extended range hybrid electric vehicles. They designed and integrated a multistage TAE with an internal combustion engine and performed experiments to determine the efficiency of the combined TAE and ICE system. Figure 1.5 shows a diagram of the TAE integrated with the ICE. The TAE uses exhaust gas from the ICE to excite a thermoacoustic response in helium held inside the TAE. The thermoacoustic instabilities are transferred into electricity via an “acousto-electric device” and the electricity is used to power the car’s battery, allowing it to operate on electricity for longer periods of time.

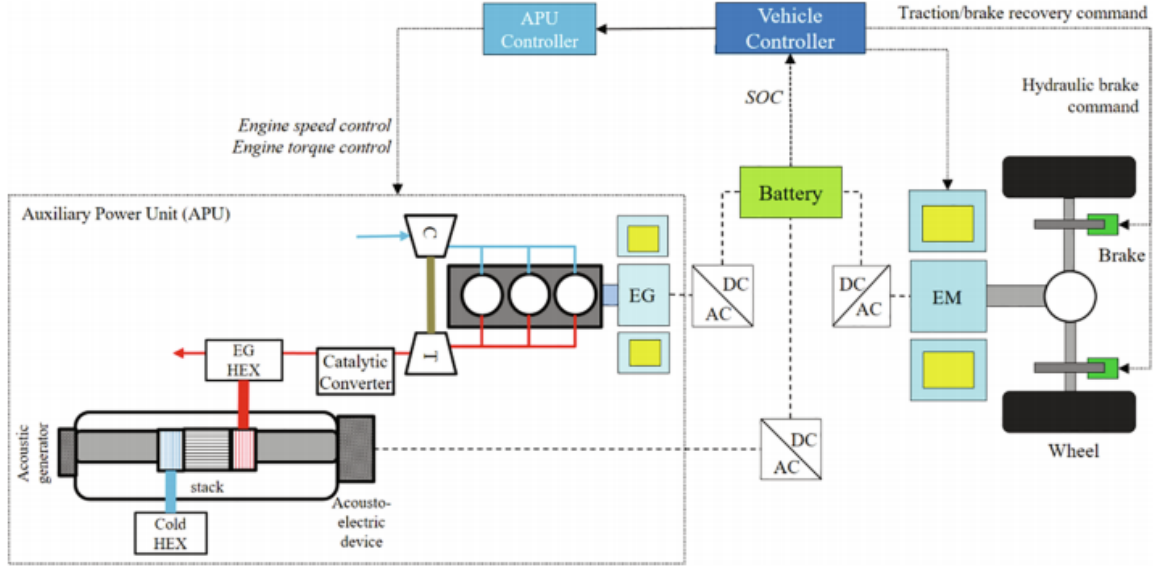


Figure 1.5. Configuration of the coupled TAE and ICE system used in the Bou Nader et al. research. The TAE passes hot exhaust gas from the ICE to the hot heat exchanger. The cold heat exchanger takes in ambient air. The thermoacoustic response produced by the helium in the engine is used to generate electricity to charge the battery in the hybrid car, allowing the car to operate for longer durations on electricity, improving fuel efficiency [18].

Bou Nader et al. tested three different TAEs, a single stage, a two stage, and a three stage TAE. Each stage in the TAE added a new set of heat exchangers and stack each designed to operate at a lower temperature than the previous stage. They found that integrating the TAE with the ICE could reduce fuel consumption by up to 7.6% in the three stage configuration [18].

A flywheel-piston assembly was used by Biwa et al. in 2020 to generate electricity from a travelling wave TAE. They used air at ambient conditions as the working gas. Over a series of tests varying the ΔT across the regenerator, they obtained a maximum power output from the piston-flywheel assembly of 11 mW [19].

In 2019, Timmer et al. demonstrated a bidirectional turbine design for electricity generation which will be discussed in more detail in section 1.2.4.

1.2.3 Previous Work in Thermoacoustics with R-218

Most of the work done in thermoacoustics up to the present has been performed with gaseous working fluid outside of the critical condition of the fluid. In 2018, Alexander et al. [20] were the first to use transcritical fluids for thermoacoustic applications. Transcritical fluids offer a variety of advantages over gaseous working fluids in TAEs. The main advantage of transcritical fluids is the sensitivity of their density to temperature. Imposing a small temperature gradient on a fluid in its critical temperature and pressure region will incite large changes in fluid density, and therefore pressure. A range of working fluids was considered for Alexander's study, eventually, octafluoropropane, R-218 was identified by Steve Hunt as a good candidate for transcritical thermoacoustic applications given its relatively moderate critical temperature and pressure making it feasible for laboratory experimentation.

Alexander et al. designed a standing wave device which used a stack heated on one end by a heating cartridge and cooled by natural air convection on the other to bring the R-218 to its transcritical temperature region. The experiment was pressurized with nitrogen via a bladder accumulator to bring the R-218 to its critical pressure region. Figure 1.6

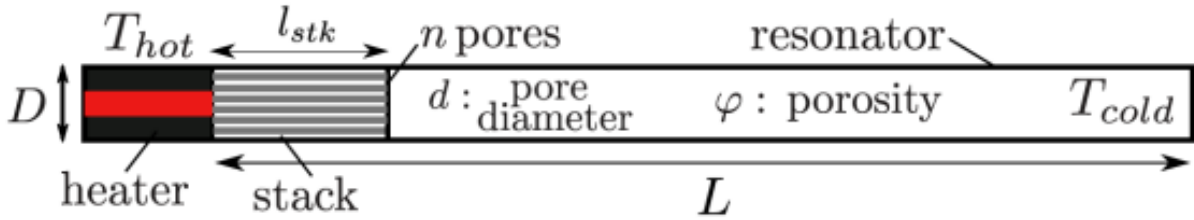
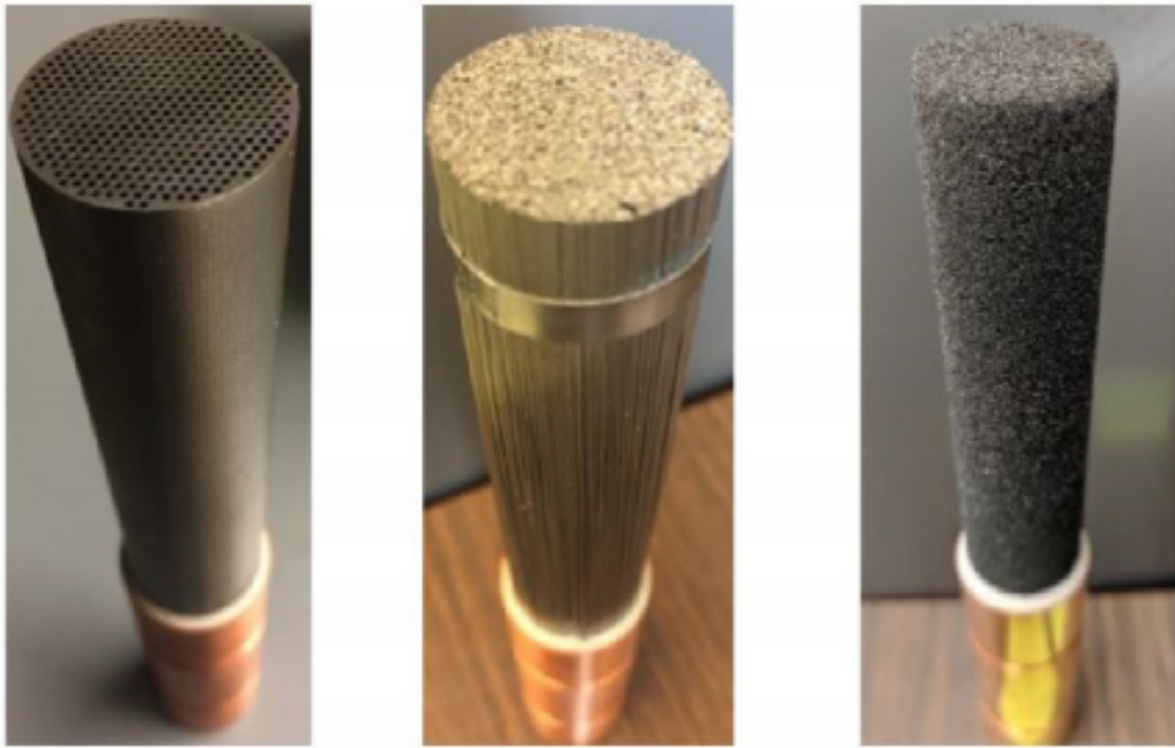


Figure 1.6. Experimental configuration used by Alexander et al. [20].

Alexander et al. tested three different stack configurations, a 3D printed Inconel tube with hollow channels, a bundle of stainless steel microtubes, and a section of porous graphite foam, to determine which stack design was best for producing thermoacoustic instabilities in R-218. Figure 1.7 shows the three designs tested.



(a) 3D printed stack.

(b) Microtube stack.

(c) 100 PPI foam stack.

Figure 1.7. The three stacks tested by Alexander et al. [20].

Of the three stacks tested, only the bundle of stainless steel microtubes were able to produce a thermoacoustic response under the critical conditions of R-218.

After the work of Alexander et al. was complete, the team at Purdue decided to continue investigating R-218 by constructing a new experiment to characterize its thermoacoustic capabilities. Martinez [21] built a new experiment informed by the findings of Alexander et al. The new experiment was also a standing wave device, but was modular, with the capability to vary resonator length. Martinez's experiment also employed a new heat exchanger. The new heat exchanger, designed in conjunction with Mezzo Technologies, consisted of a hot and cold heat exchanger, driven by heated oil and water flows respectively, which impose a temperature gradient on a bundle of stainless steel microtubes surrounded by a vacuum cavity which could be evacuated before testing to provide the working fluid insulation from

ambient conditions. Martinez’s experimental design is discussed in more detail in section 2.2.

Martinez thoroughly characterized the thermoacoustic capabilities of R-218. The thermoacoustic response of the fluid was tested at seven different pressures ranging from 0.9 to 1.3 times the critical pressure of R-218 and five different temperature configurations ranging from a ΔT of 79K to 150K from the hot to cold heat exchangers. Martinez observed that pressure amplitudes increased with ΔT and recorded maximum a peak-to-peak pressure amplitude of 690kPa. She noted that operational frequency was less dependent on fluid conditions, varying 28% from an average of approximately 5Hz. Martinez also investigated the effects of resonator length on the thermoacoustic response of R-218, varying resonator length from 100 to 200cm at three different bulk pressures. Maximum pressure amplitude was achieved at a resonator length of 179cm, Martinez found that increasing resonator length lowers operational frequency, allowing more time for thermal diffusion into the working fluid, but, that at some point, viscous losses incurred by increasing the length of the resonator outweigh the benefits of increasing the length. Finally, Martinez investigated the power production and capability for energy extraction from R-218 in her experiment. A tube was installed to allow the fluid to recirculate through the resonator and check valves were installed to assure the fluid circulated in one direction. Martinez installed a valve which was opened in increments to allow a percentage of fluid to recirculate and the power required to push the tap-off fluid through the recirculation line was measured. The power required to push the fluid through the recirculation line can be taken as a surrogate for extracting power from a standing wave device of similar configuration. Martinez found that up to 73% of acoustic power can be extracted before destruction of the acoustic wave. The findings of Martinez’s study have laid the groundwork for the work which will be described in the following chapters.

1.2.4 Energy Extraction via Turbines

There are many methods to extract work from thermoacoustic instabilities. There are three categories of devices which can extract power from a thermoacoustic device, thermoelectrics, power extraction via thermodynamic cycle such as the Rankine cycle, or turbines.

Each method has its advantages and disadvantages. Thermo-electric devices have the benefit of not using moving parts, they are simply installed into the termoacoustic device and can generate electricity using the changes in heat in the system. Thermo-electric devices, however, are not very efficient and frequently require some kind of bonding agent to be installed which can wear out when exposed to constant heat gradients over time. Using a cycle, such as the Rankine cycle, to extract power has the benefit of being significantly more efficient than thermo-electric devices. Rankine cycles, however, require much more hardware and moving parts than thermo-electrics, and therefore require more maintenance. A turbine installed directly into the TAE provides a balance between these two extremes. A turbine is more robust than a thermo-electric device as it is installed mechanically using a shaft and mounting assembly, rather than an adhesive, and it only requires a single moving part. This work will focus on the use of bidirectional turbines to extract work from thermoacoustic instabilities as they have the most promise for use with high density fluids.

A bidirectional, or self-rectifying, turbine is a turbine in which the rotational direction is independent of the direction of fluid flow. Self rectifying turbines saw their advent in oscillating water column (OWC) systems. In an oscillating water column system, a column of air is contained in a structure which is open on one end to atmosphere, and open on the other end to ocean water. At the top of the structure, a self rectifying turbine is mounted. OWC turbines typically operate in the range of 750 - 1500RPM [22]. The motion of ocean waves coming into or out of the structure pushes the air column up or down respectively, driving the turbine. Figure 1.8 shows an oscillating water column assembly.

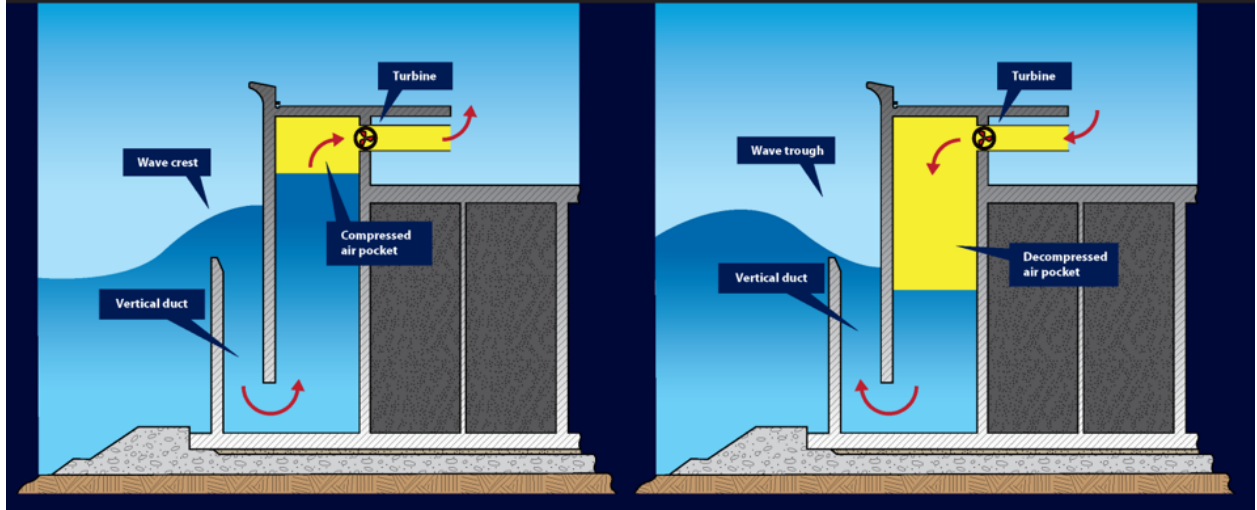


Figure 1.8. An OWC system diagram. (Left) Inflow diagram showing ocean waves flowing into the column and pushing air through the turbine out of the top of the column, driving the turbine. (Right) Outflow diagram showing ocean waves flowing out from the column, allowing air to enter through the top of the column, driving the turbine [23].

There are two basic types of self-rectifying turbines, a Wells turbine and a bidirectional impulse turbine. Figure 1.9 shows both types of turbine.

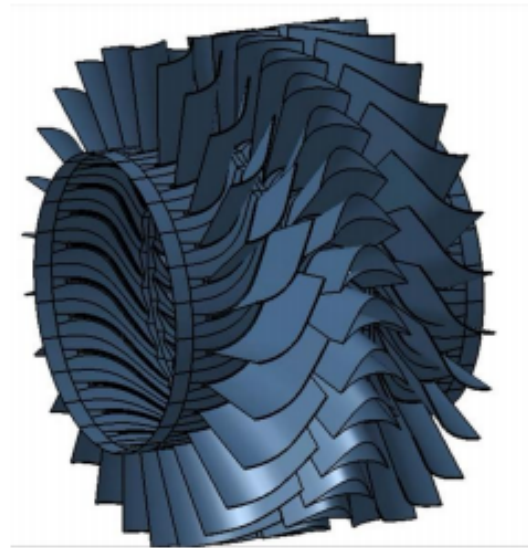
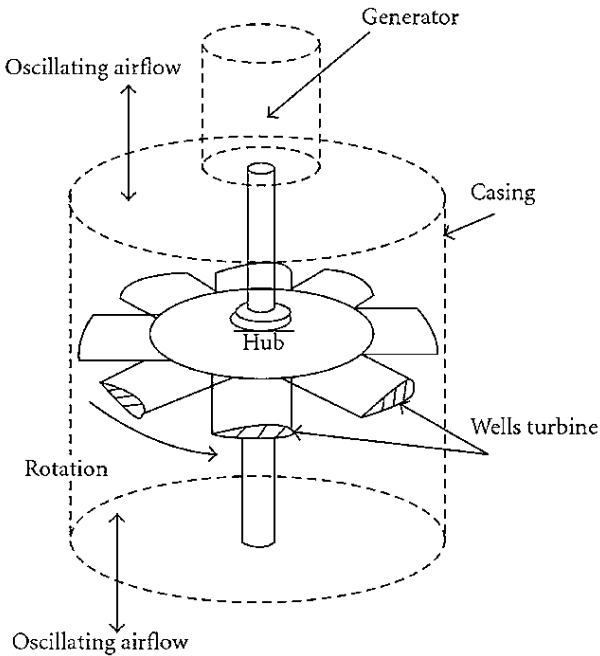


Figure 1.9. (Left) A wells turbine [24]. (Right) A bidirectional impulse turbine [25].

A Wells turbine uses symmetrical airfoils perpendicular to fluid flow to direct bidirectional flow into unidirectional rotation. Regardless of the flow direction, a Wells turbine airfoil will always direct the fluid flow to the trailing edge of the airfoil, so it will only rotate in one direction. Wells turbines suffer from having to operate primarily with high angle of attack with respect to the airflow. It follows, then, that as flow velocity increases, a Wells turbine may stall. While Wells turbines are cost effective and relatively easy to manufacture, they provide poor efficiency and starting characteristics in comparison to a bidirectional impulse turbine [26]. Given this restriction, Wells turbines are better suited to low pressure, and low speed applications.

A bidirectional impulse turbine directs flow into the rotor blades via use of guide vanes. The guide vane, or stator is a stationary airfoil which speeds up and directs flow into the rotor blade. Bidirectional impulse turbines have a mirrored symmetrical set of guide vanes on either side of the rotor blade assembly to direct bidirectional flow into unidirectional rotation. A bidirectional impulse turbine must have a degree of reaction equal to zero, implying all of the pressure drop observed in the turbine occurs over the stator. This is required to maintain symmetry about the rotor blade, if a bidirectional turbine had a nonzero degree of reaction, the rotor blade would not be symmetric, and would not work in bidirectional flow [26].

Although both Wells turbines and bidirectional impulse turbines have historically been used in OWC systems, the thermoacoustics research community has taken interest in translating work on bidirectional impulse turbines in OWC systems for use in thermoacoustic applications. Kees de Blok et al. from Aster Thermoacoustics were the first to implement a bidirectional impulse turbine into a thermoacoustic heat engine [27]. Figure 1.10 shows the experimental setup de Blok used.

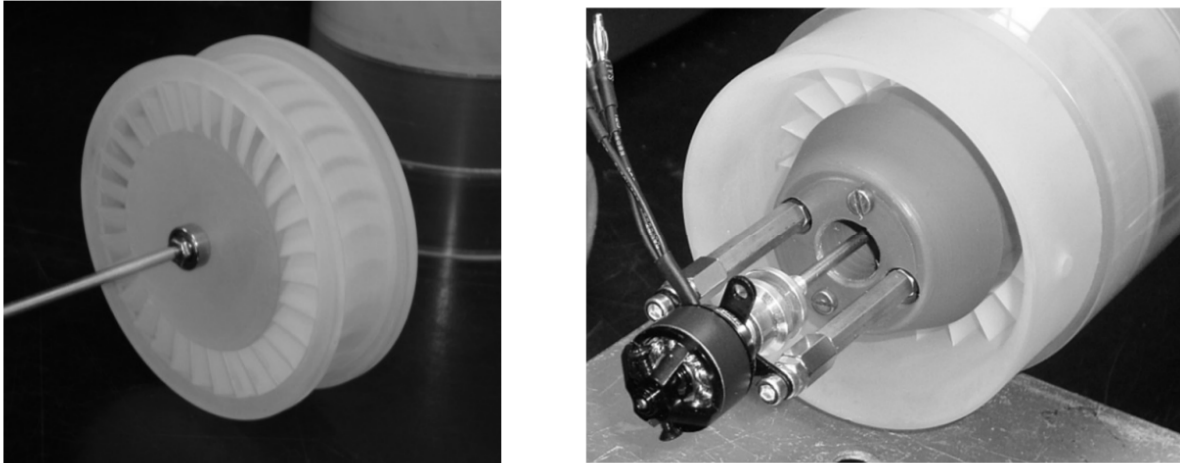


Figure 1.10. 3D printed bidirectional impulse turbine used in the de Blok et al. experiments. A loudspeaker was used to excite acoustic pressure oscillations in air to drive the turbine [27].

de Blok performed a series of measurements on the turbine using a loudspeaker to drive acoustic oscillations in air to determine rotor efficiency for various operational frequencies and power outputs. Figure 1.11 shows the results of the study.

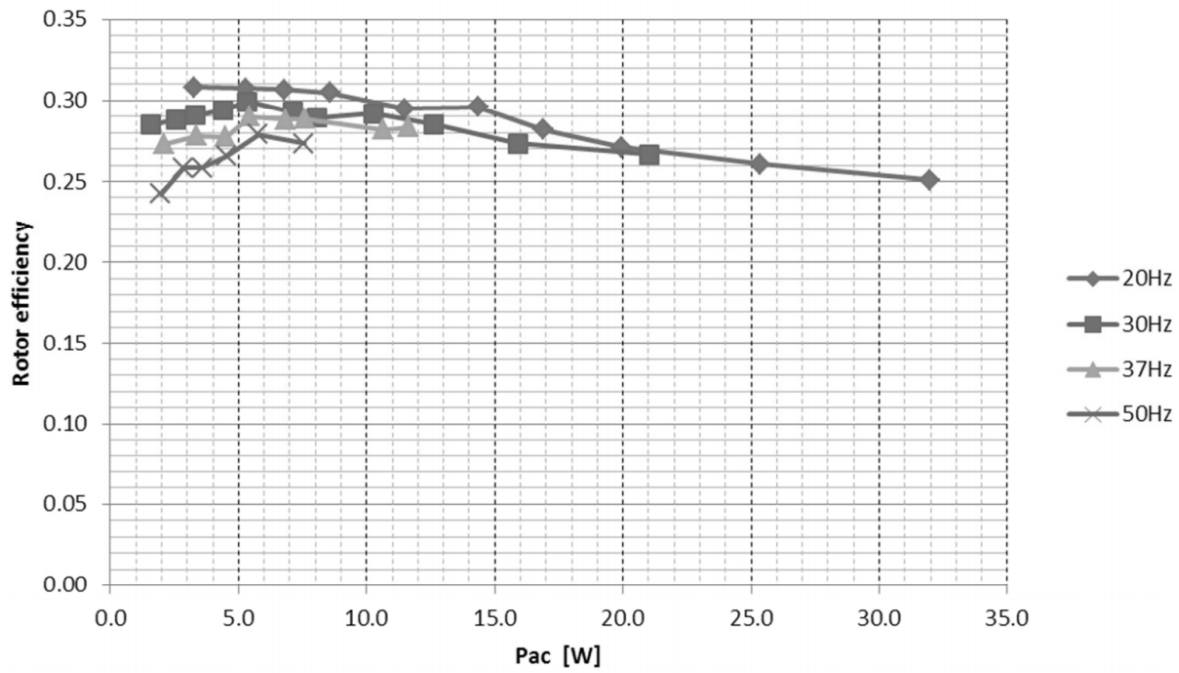


Figure 1.11. Experimental results of de Blok's study show that bidirectional turbines perform well under high frequency conditions, achieving a maximum rotor efficiency of just over 30% at 20Hz [27].

de Blok also predicted that rotor efficiency could increase further with increasing working fluid density. Figure 1.12 shows the predicted rotor efficiency curve as a function of density.

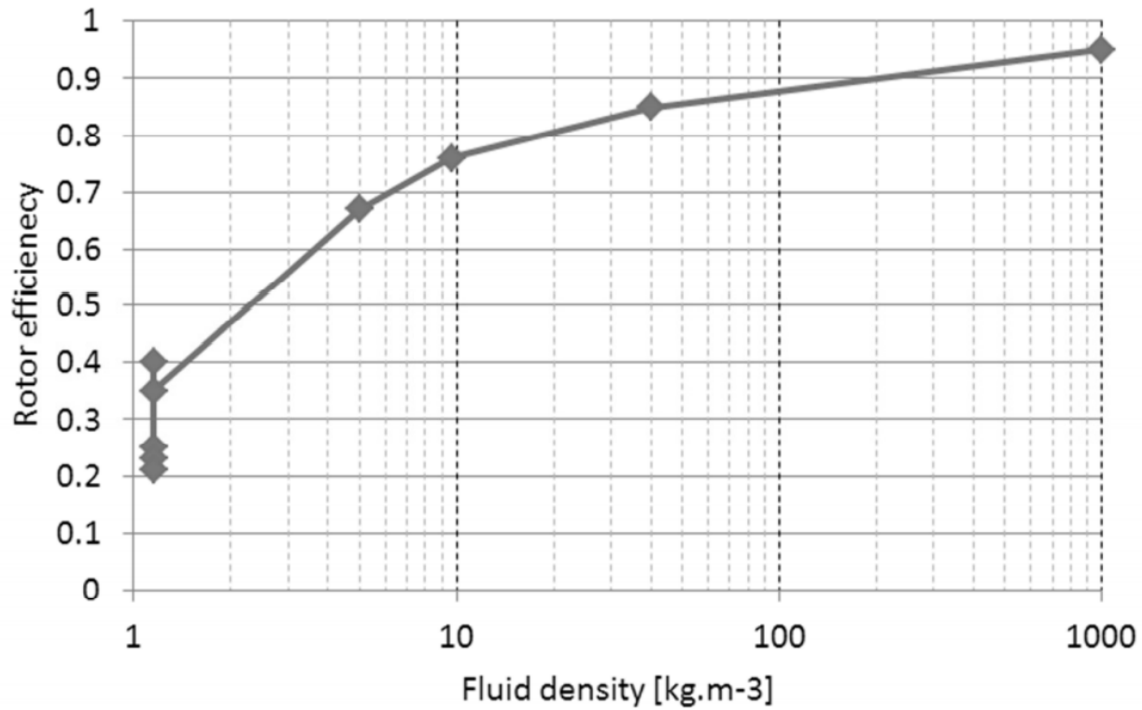


Figure 1.12. Predicted rotor efficiency as a function of working fluid density [27].

In 2019, Michael Timmer and Theo van der Meer from the University of Twente in The Netherlands published a new study investigating a bidirectional impulse turbine in thermoacoustic applications. Similar to de Blok, Timmer and van der Meer used a loudspeaker to excite pressure oscillations in air to drive their turbine [28]. Figure 1.13 shows the turbine used in Timmer and van der Meer's experiments which is based on an OWC turbine from Suzuki et al. [29].

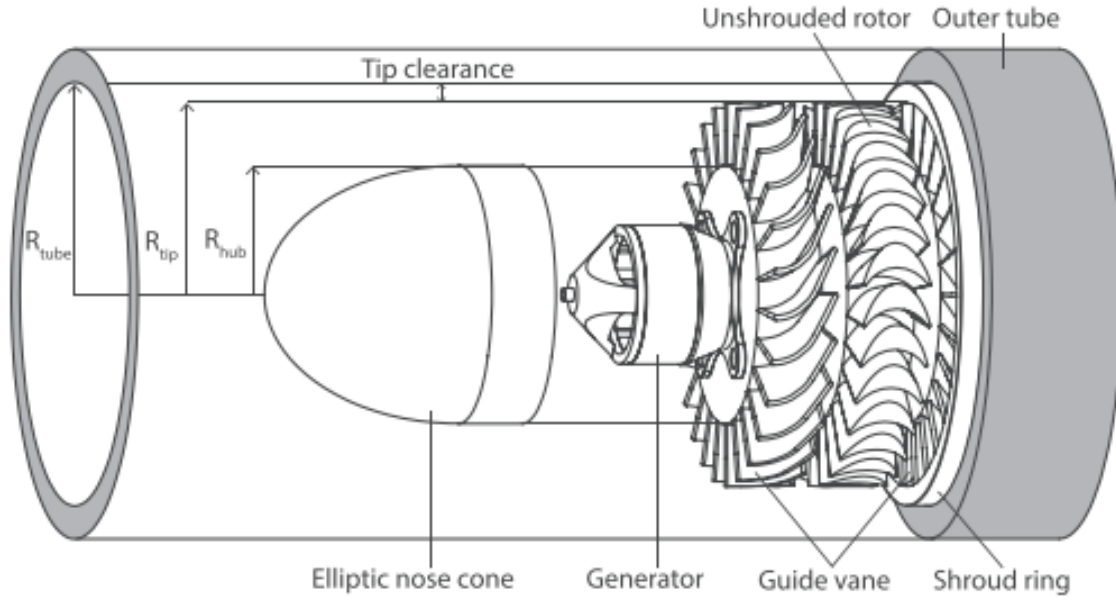


Figure 1.13. Bidirectional impulse turbine used in the experiments of Timmer and van der Meer [28].

Although Timmer and van der Meer only achieved a maximum turbine efficiency of 25%, they performed and validated a dimensional analysis which determined that turbine efficiency is dependent only on nondimensional acoustic power drop over the turbine and of flow coefficient, or the ratio between axial input flow velocity and rotor tip circumferential velocity.

Bidirectional impulse turbines in thermoacoustic applications are still a relatively new area of research. They provide promising advantages over other methods of extracting power from thermoacoustic devices. They have potential to be more efficient than other methods of power extraction and are predicted to perform well with high density fluids.

1.3 Document Overview

The following chapters in this document detail new work done over the past year on TTE research at Purdue University. Chapter 2 discusses the experimental design used in this research. Chapter 3 discusses the results of tests carried out using the TTE in the fall of 2020. Chapter 4 discusses the design of a bi-directional impulse turbine which is intended for energy extraction from the TTE. Finally, chapter 5 concludes the document with a summary

of experimental results, design work done, a discussion of lessons learned, and suggestions for future work.

2. EXPERIMENTAL FACILITY

An experiment was designed by Martinez [21] to characterize the thermoacoustic properties of transcritical fluids. A range of working fluids for the experiment were investigated by Hunt in 2016 [30]. R-218 was chosen as the working fluid for the experiment because the critical temperature and pressure of R-218 are feasible for laboratory testing. Tab. 2.1 lists the critical conditions of R-218.

Table 2.1. Critical Conditions of R-218 from the National Institute of Standards and Technology (NIST)

Parameter	Value
Critical Pressure (P_{cr})	2.68MPa
Critical Temperature (T_{cr})	345.05K

Martinez’s experiment built upon the experiments of Alexander [20] which defined the best method for transferring heat to R-218 to obtain a thermoacoustic response. In 2020, changes were made to the existing facility to begin a new study which expanded the operating envelope of Martinez’s experiment. This section lists experimental objectives of the new study, summarizes Martinez’s experimental and test article design, discusses changes made to Martinez’s experiment, describes instrumentation used in testing, and reports an uncertainty analysis on the instrumentation.

2.1 Experimental Objectives

At the beginning of the test campaign, several objectives were laid out with the goal of developing an understanding of the power generation capabilities of transcritical R-218 to aid in the design of a power extraction device. The objectives are as follows:

1. Verify repeatability with prior experiments.
2. Assess the influence of resonator length on the thermoacoustic response of R-218.
3. Assess the influence of resonator diameter on the thermoacoustic response of R-218.

4. Assess the influence of coiled resonator tube sections on the thermoacoustic response of R-218.

Three studies were performed to achieve these objectives. First, a sample of Martinez’s test conditions were replicated and compared to her results. Second, a study was performed which varied resonator length and assessed the changes in both pressure amplitude and operational frequency. Finally, a study was performed which varied resonator diameter and, again, measured changes in pressure amplitude and operational frequency. The results of all studies were compared with modelling results and prior experiments to characterize the effects of resonator geometry on the thermoacoustic response of R-218.

2.2 Experimental Design

Martinez’s experiments focused on defining both the thermoacoustic characteristics of transcritical R-218, and its feasibility for use as a working fluid for power extraction. The experimental setup used in this work is referred to as the “rig”. In this study, changes were made to the existing experiment to support several new studies focused on understanding the effect of rig geometry on the thermoacoustic response of transcritical R-218, and therefore available acoustic power developed by thermoacoustic instabilities. The individual parts of the rig are summarized in this section. A more detailed discussion on design can be found in Martinez’s thesis [21].

2.2.1 System Overview

Figure 2.1 shows the plumbing and instrumentation diagram (P&ID) for the rig. The rig can be divided into three separate sections: the fluid loading and pressurization system, the test section which includes a heat exchanger and resonator section, and heat exchanger support hardware.

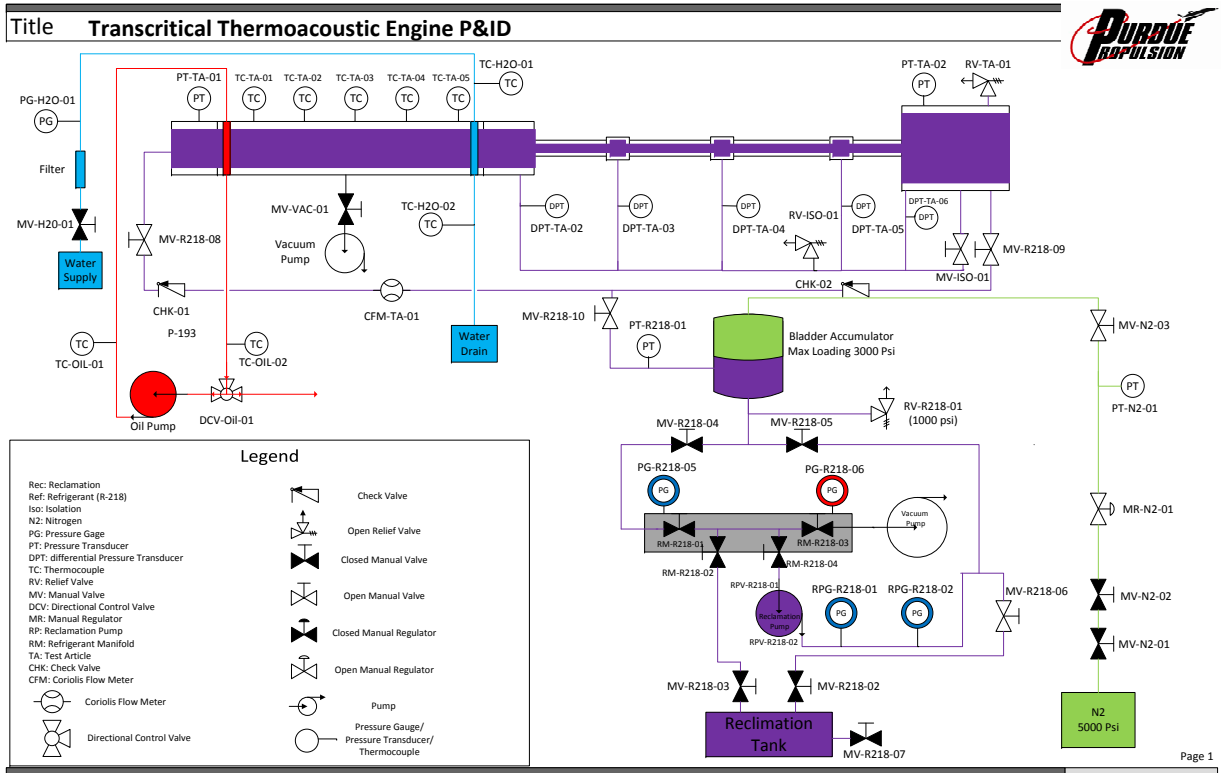


Figure 2.1. Plumbing and Instrumentation Diagram of the experimental setup. Purple represents R-218 flowpaths, green represents nitrogen, red represents Duratherm G heat transfer fluid, and blue represents water. The Coriolis flow meter (CFM-TA-01) is optional hardware not employed in this work [21].

Figures 2.2 - 2.4 show the loading and pressurization system components. This system includes a storage tank for R-218, a manifold for routing fluid from storage to the rig, a pump for loading and unloading fluid, a vacuum pump to evacuate the test section before fluid loading, and a bladder accumulator used for pressurization. To achieve a sustained and significant thermoacoustic response from R-218, it must be near its critical pressure. In this region, the density of R-218 is sensitive to changes in temperature and is prone to develop thermoacoustic instabilities when exposed to a significant temperature gradient. The system is pressurized via a 3000psi bladder accumulator.

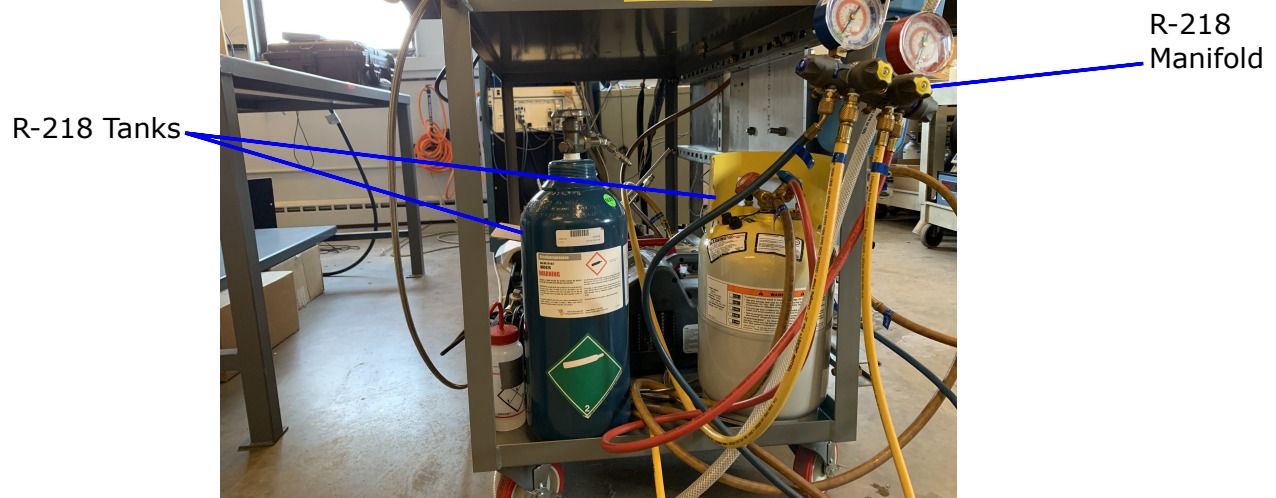


Figure 2.2. R-218 storage tanks.

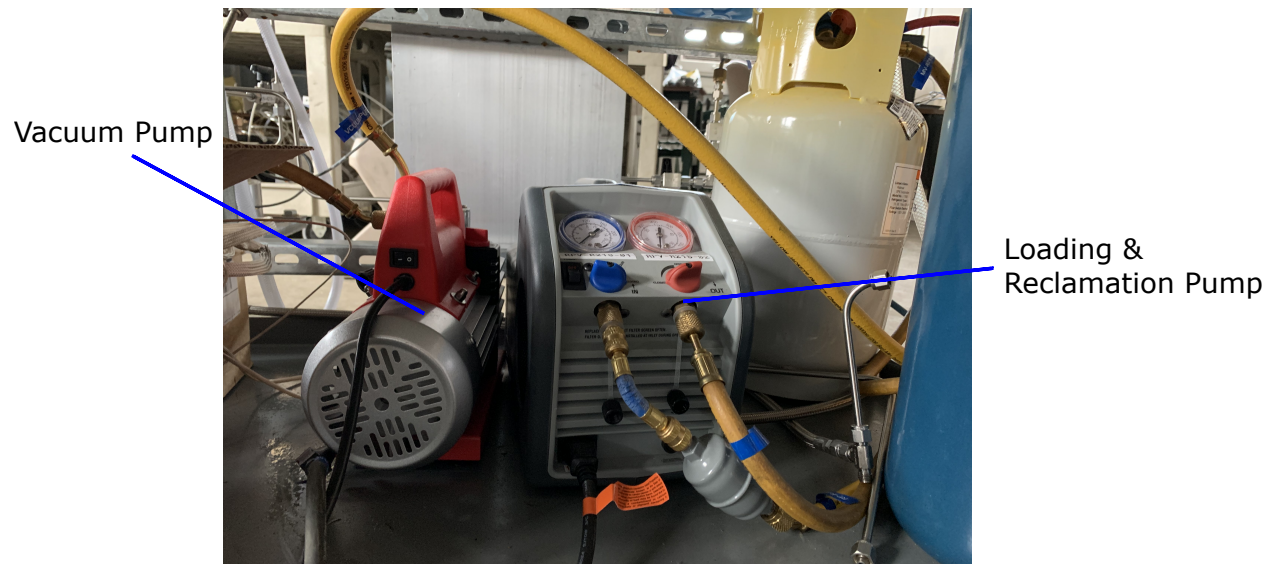


Figure 2.3. R-218 loading/reclamation pump and vacuum pump.



Figure 2.4. Nitrogen bladder accumulator.

Figure 2.5 shows the components of the heat exchanger support system. this system includes a pressure fed tap water supply, a heat transfer oil pump, and a vacuum pump. The water supply is taken from facility supply and run through a filter before being introduced into the heat exchanger. The vacuum pump, shown in figure 2.3, is used to evacuate the space around the microtube stack to insulate the stack from ambient conditions. The oil and water supplies deliver hot and cold fluid respectively to the heat exchanger to induce a temperature gradient along the microtube stack which, when the temperature gradient is large enough and the R-218 is pressurized to near its critical pressure, excites thermoacoustic instabilities in the test section which can be recorded with pressure transducers.

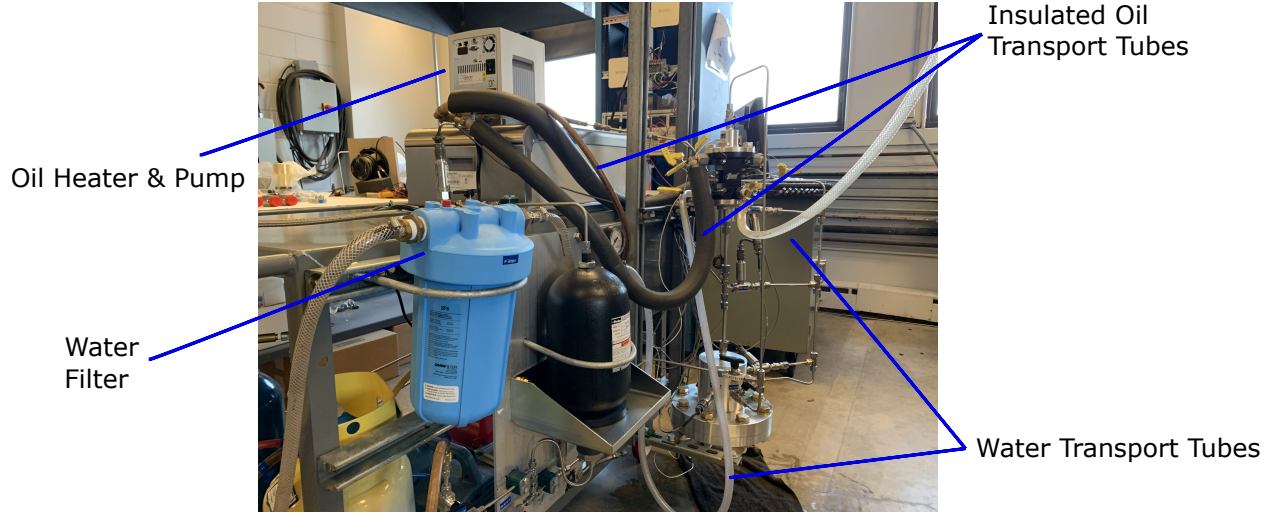


Figure 2.5. Heat exchanger support hardware.

Figure 2.6 gives a basic outline of the components of the test section of the rig. The test section consists of a heat exchanger, a cavity on the hot side of the heat exchanger, three resonator sections, and a recirculation line.

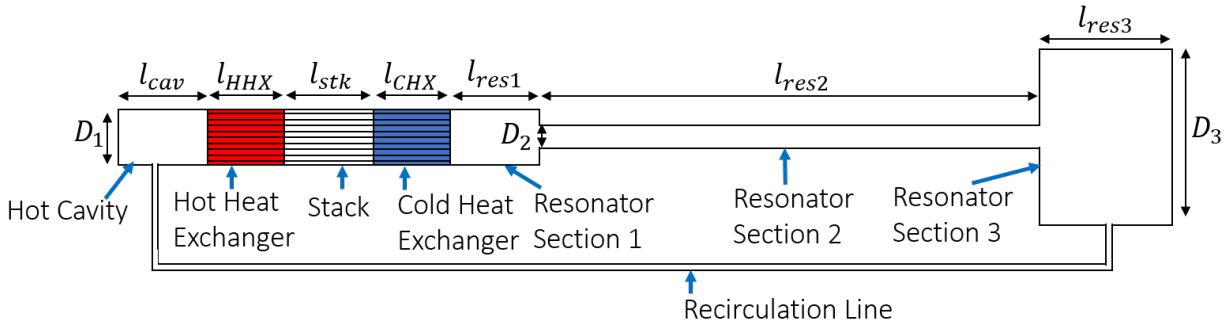


Figure 2.6. Schematic of the thermoacoustic engine [21].

Table 2.2 gives all major rig dimensions listed in fig. 2.6.

The test section is primarily a standing wave device, but is outfitted with a recirculation line used to operate the rig as a travelling wave device. There are two manual ball valves on the top and bottom of the rig which can be closed to isolate the recirculation line and operate the device as a standing wave engine. The ability to operate the test section as a

travelling wave device was implemented by Martinez when the self-pumping characteristics of R-218 were being investigated [21]. Fig. 2.7 shows a CAD image of the rig test section.

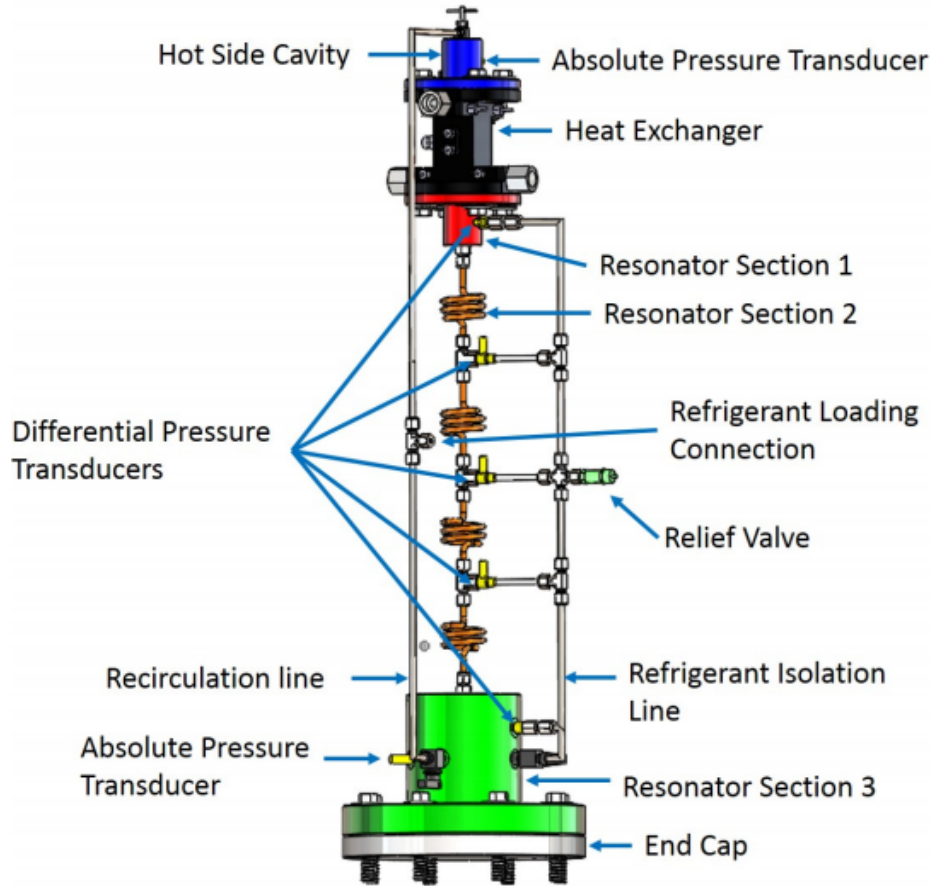


Figure 2.7. A computer aided design (CAD) image of the thermoacoustic engine before changes were made. The test section consists of two major components: the heat exchanger, and resonator section [21].

The first component of the resonator section is the hot side cavity. This cavity is attached to the top of the heat exchanger and provides a path for fluid loading. It also has a port to attach one of the two standing/travelling wave valves. This cavity provides a volume for R-218 to boil-off into without over-pressurizing the system. The next section is resonator section 1, it has the same geometry as the hot side cavity but is outfitted with different instrumentation and fluid connection ports. The bulk of the test section is taken up by resonator section 2. In the rig's original configuration, resonator section 2 consists of a

series of coiled 1/4" - 0.053" tubes separated by differential pressure transducers (DPT). Resonator 2 has a section of tubing connected to the opposing side of the DPTs which can be isolated from the test section after pressurization, allowing for accurate differential pressure measurements. The length of resonator section 2 is modular and can be outfitted with tubes of varying length. Resonator 2 is where the bulk of pressure measurements take place and where the most accurate reading of pressure amplitude and frequency can be obtained. Resonator section 3 has the second of the standing/travelling wave valves. Additionally it has ports for instrumentation and a fluid loading valve. Resonator 3 is designed with a flange on the end to adapt to a power extraction device.

The heat exchanger is the most complicated and important component in the test article. It was designed in conjunction with a team of Mezzo Technologies engineers. The heat exchanger is the device which delivers heat to the pressurized R-218 and therefore excites thermoacoustic instabilities in the fluid. Within the heat exchanger, R-218 flows through a stack of microtubes which distribute heat to the R-218 by imposing a temperature gradient between the top and bottom of the stack. The temperature gradient is created using heated Duratherm G Heat Transfer Fluid and water flowing through the ports on the top and bottom of the heat exchanger respectively.

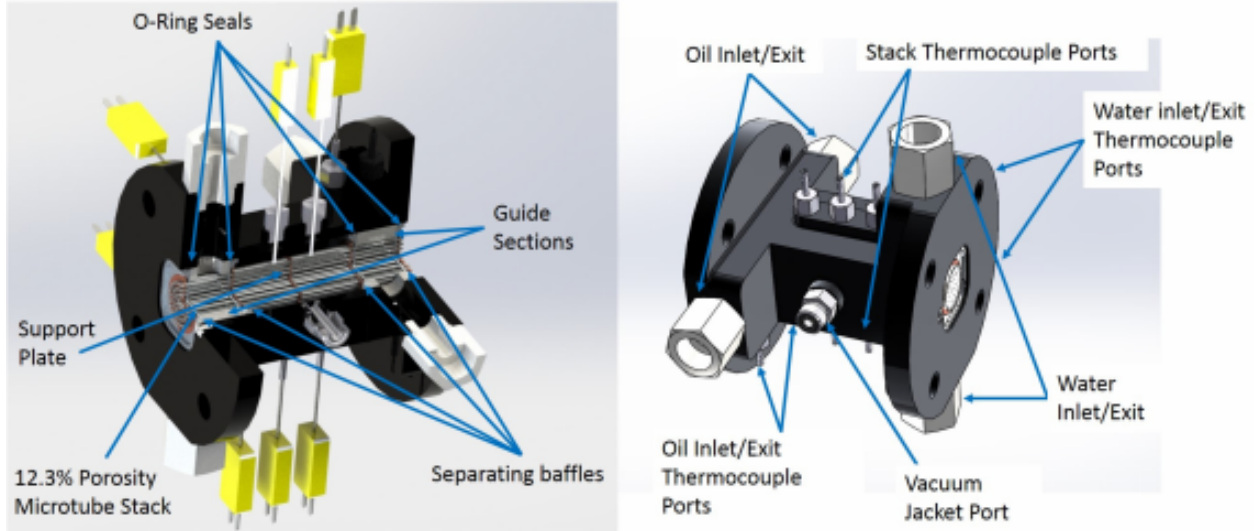


Figure 2.8. A CAD image of the heat exchanger designed in conjunction with Mezzo Technologies. The cross-section on the left shows the microtube stack with sealing and mounting hardware. The right image shows fluid and instrumentation connections on the heat exchanger exterior [21].

Fig. 2.8 shows a CAD image of the heat exchanger. The heat exchanger sits between the hot side cavity and resonator section 1, depicted in Fig. 2.7. It attaches via a flange on either side through which the temperature control fluids flow. The heat exchanger supports temperature readings on both the inlet and outlet oil and water ports, as well as axial readings along the microtube stack. The heat exchanger has a vacuum jacket port to allow a vacuum pump to evacuate the space around the microtube stack to insulate it from ambient conditions during operation. A detailed discussion of the design of the heat exchanger is included in Martinez's thesis.

2.3 Changes Made to the Experimental Setup

Table 2.2 lists all major rig dimensions. Any dimension that was varied for this work is listed as a range of values.

Table 2.2. Rig Dimensions

Parameter	Value (cm)
D_1	2.352
D_2	0.457, 0.622, 0.704
D_3	10.670
l_{cav}	5.080
l_{HHX}	2.030
l_{stk}	6.100
l_{CHX}	2.030
l_{res1}	5.080
l_{res2}	55.880, 101.600, 177.800
l_{res3}	15.240

Several changes were made to the rig to support variation in both resonator 2 length and diameter. Modifications were made primarily to resonator section 2. Additionally, some support hardware was swapped out to adapt to the changes made in resonator 2.

2.3.1 Removing Coils from the Resonator

The first change made to the experiment was to remove the coils in resonator section 2. It was hypothesized that viscous losses incurred while the R-218 was flowing through the coils was reducing the pressure amplitudes of the thermoacoustic instabilities developed by the rig. The ratio of bend radius to tube diameter of the 1/4" coiled tubes was 2.25. Minimizing viscous losses would increase acoustic power developed by increasing pressure amplitudes of the thermoacoustic instabilities produced by transcritical R-218. To achieve these objectives, the height of the rig was increased significantly to achieve similar resonator lengths to Martinez's experiment without using coiled tubes in resonator section 2.

Martinez's rig was disassembled to allow access to the unistrut rail used to mount the heat exchanger and resonator section 3. The existing unistrut was swapped out for longer unistrut, approximately 8 feet in length, and resonator 2 was reconstructed using straight

tube sections. The height modification allowed the rig to be tested without coils up to a resonator 2 length of approximately 70in.

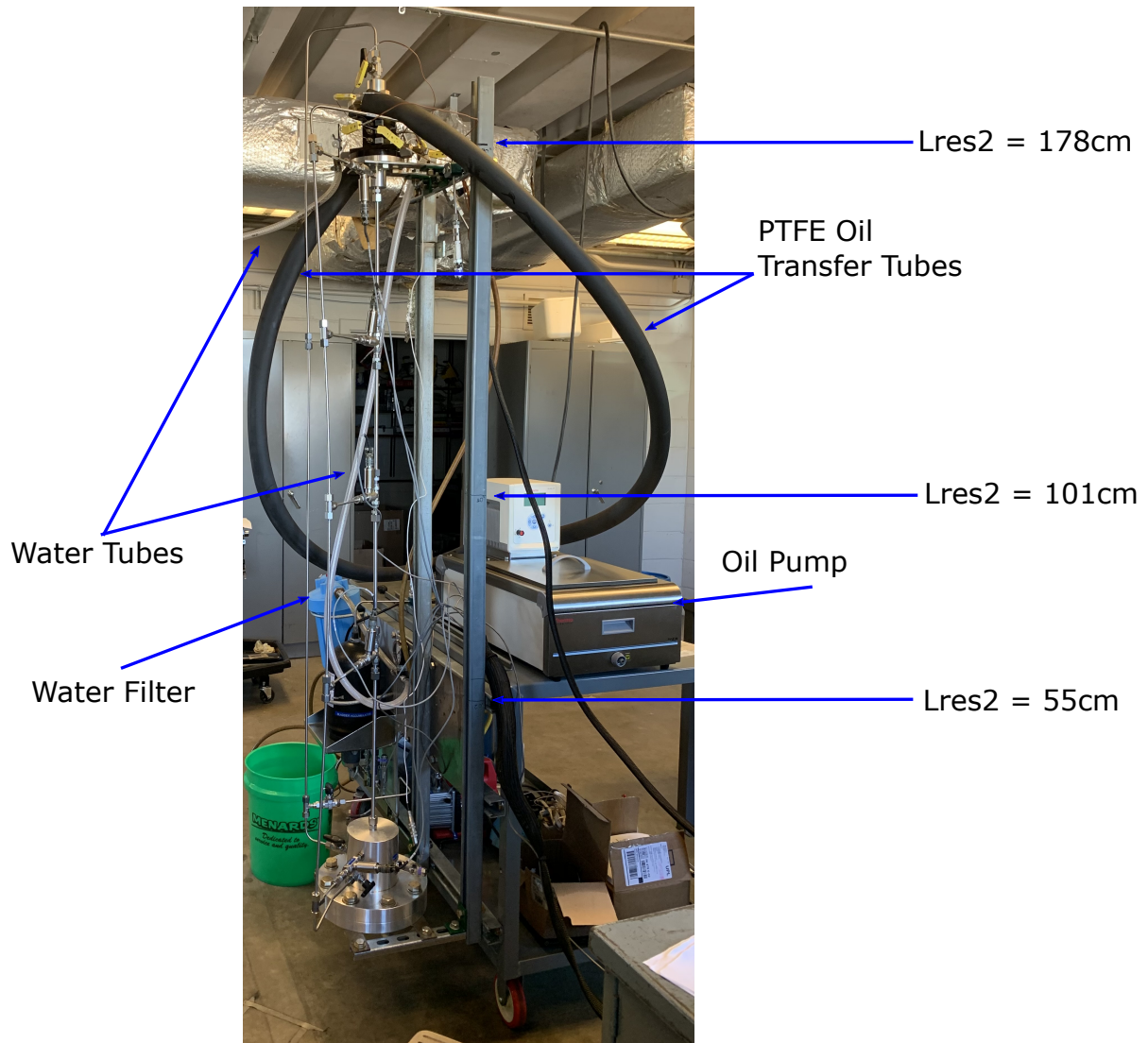


Figure 2.9. Rig with new height modification. The total height of the unistrut support is 75in. The red lines indicate the lengths at which the rig was tested.

Fig. 2.9 shows the rig with the new length modification. The length leaders on the figure notate resonator 2 length at the marked station. The black tubes running along the left and right of the rig are the new oil transport tubes. The oil transport tubes are 3/4" outer diameter (OD), 1/2" inner diameter (ID) flexible Polytetrafluoroethylene (PTFE) tubing

insulated with seamless flexible rubber foam pipe insulation. The new tubes are attached to the heat exchanger using tube collars and barbed fittings. The water connection also needed to be lengthened which required a longer section of 3/4" OD, 1/2" ID soft polyvinyl chloride (PVC) plastic tubing to be cut and installed onto the water filter. Table 2.3 lists the location of pressure transducers used in the rig. All lengths are measured from the top of the hot side cavity.

Table 2.3. Pressure Transducer Location for Each Resonator 2 Length Tested

Instrument	Location (cm)		
	$l_{res2} = 55.880$	$l_{res2} = 101.600$	$l_{res2} = 177.800$
Hot Side Cavity Kulite Absolute PT	1.65	1.65	1.65
Resonator 1 DPT	17.00	17.00	17.00
Resonator 2 First DPT	32.63	50.87	76.27
Resonator 2 Second DPT	54.25	84.74	135.54
Resonator 2 Third DPT	72.88	118.61	194.81
Resonator 3 DPT	80.88	126.60	142.80
Resonator 3 Absolute PT	84.88	130.60	146.80

The operation of the oil pump with the new PTFE tubes created an issue with oil distribution. When the rig was in its longest configuration and while the oil pump was heating up, there was not sufficient pump head to supply the heat exchanger with oil until the pump setting was increased. Once the pump setting was increased, a large slug of pre-heated oil was introduced to the heat exchanger. The sudden arrival of pre-heated oil to the heat exchanger may have contributed to a sealing issue which will be discussed in chapter 3.4.

The height modification also presented some issues. First, when the rig was being tested at a resonator 2 length of 22in, not all of the differential pressure transducers would fit in the space. Similarly, when the rig was being tested in its longest configuration, 70in, the differential pressure transducers were spaced out significantly farther than in the 40in condition with coils tested in previous work. This resulted in a lower resolution measurement

of the waveform within the rig. In its longest configuration, the vertical height of the rig also prevented the standing wave manual isolation valves to both be closed at the same time which may have caused distortions in the growth of the thermoacoustic instability during those tests.

Ultimately, the issues which developed as a result of the modification were managed and recorded. None of the issues discussed impacted ability to record useful data.

2.3.2 Adding Functionality to Support Varying Resonator Diameter

The second change made to the experiment was to increase the diameter of resonator section 2. To further investigate how available acoustic power might be maximized, it was desired to characterize the effects of resonator 2 diameter on the thermoacoustic response of R-218. This modification was performed after the coils were removed from this section. All of the tests performed with a larger resonator 2 diameter were performed without coils.

To develop an understanding of how diameter affects the thermoacoustic response of R-218 in the rig, 2 new tube sizes were selected: 3/8" - 0.049", and 3/8" - 0.065". Both tubes were selected because they were larger than the 1/4" - 0.035" tested previously, and both have an outer diameter of 3/8". A new flaring pin was required to flare the 3/8" - 0.65" tubing. Despite needing to buy a new flaring pin, it was still less expensive than modifying the rig to accept both 3/8" OD tubing and a larger size. To accommodate the 3/8" tube diameter, a new set of fittings to affix the resonator 2 tubes to both resonators 1 and 3, and each DPT were acquired. To adapt the new tubing to the other resonator sections a set of stainless steel 3/8" Seal-Lok ORFS to 1/4" SAE straight thread fittings (6-4 F5OLO-SS) were used. Since both have the same outer diameter, only one set of fittings was required for both tube diameters. Fig. 2.10 shows one of the 6-4 F5OLO-SS fittings.

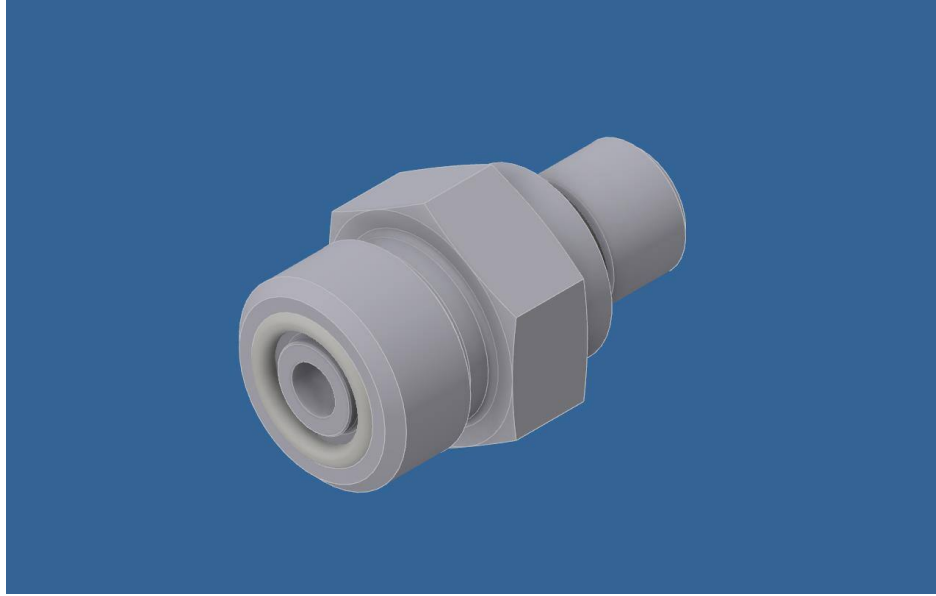


Figure 2.10. CAD image from Parker Hannifin of 6-4 F5OLO-SS fitting used to adapt to the new tube diameter. Each image shows the fitting from a different angle.

The 6-4 F5OLO-SS fittings were installed into both resonator section 1 and resonator section 3. Fig. 2.11 shows the 6-4 F5OLO-SS installed in the rig.

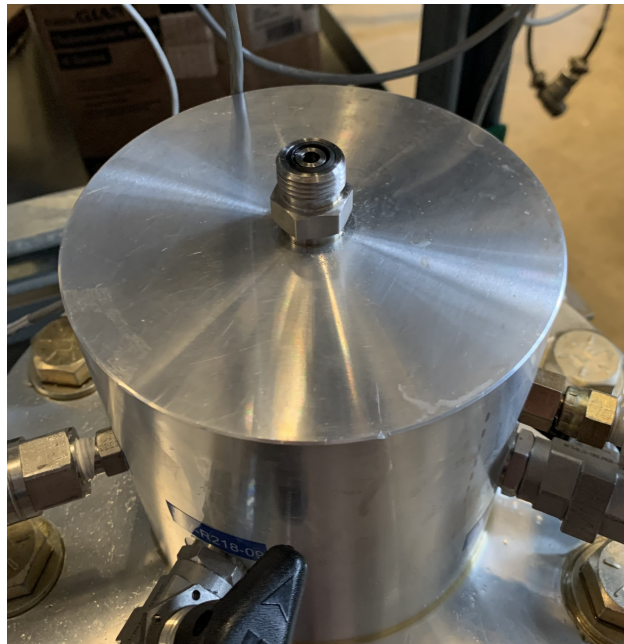


Figure 2.11. 6-4 F5OLO-SS fitting installed on the rig.

To adapt to each of the DPT connections, a set of 1/4" to 3/8" Seal-Lok expander fittings (6-4 LOHL6-S ZJ) were used. Fig. 2.12 shows the 6-4 LOHL6-S ZJ fitting.

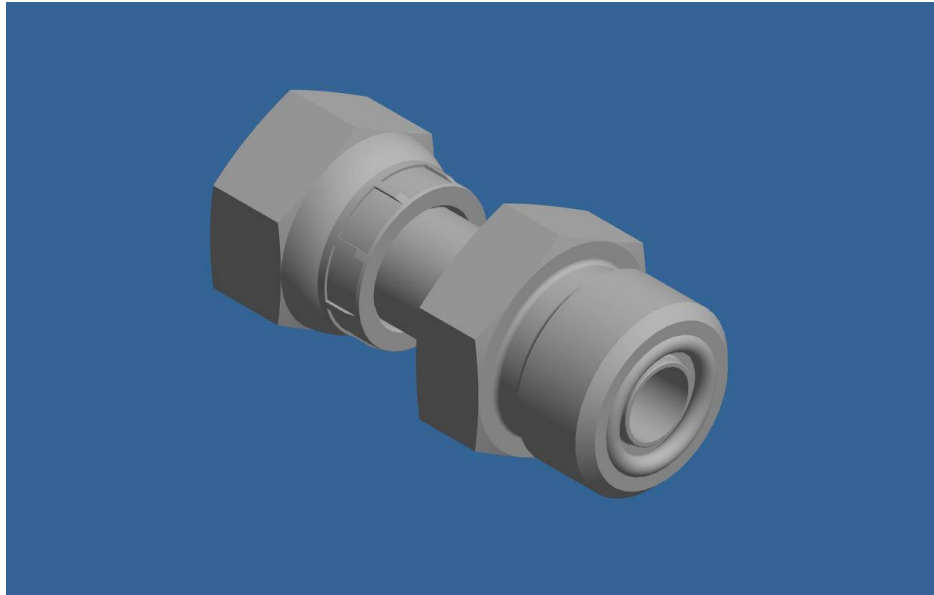


Figure 2.12. A CAD image from Parker Hannifin of the 6-4 LOHL6-S ZJ fitting used to adapt to the new tube diameter. Each image shows the fitting from a different angle.

The 6-4 LOHL6-S ZJ fittings were installed onto each DPT assembly to adapt the 1/4" architecture to accept 3/8" tubing. Fig. 2.13 shows the 6-4 LOHL6-S ZJ fitting installed in a DPT assembly.



Figure 2.13. 6-4 LOHL6-S ZJ Installed in a DPT assembly.

The brief change in diameter through the 1/4" tee used to connect the DPTs was not long enough to have a meaningful impact on the thermoacoustic waveform, and since the rig was operated in standing wave configuration, there was no concern with phasing issues given the cross sectional area change.

2.4 Instrumentation

To accurately measure the thermoacoustic response of R-218 inside the rig, both pressure and temperature readings were required. Temperature readings on the rig were only taken on the heat exchanger, while pressure readings were taken along the length of the rig. All measurements were acquired and recorded using an National Instruments Max Data Acquisition System. A LabVIEW Virtual Instrument developed for Martinez's experiment was used to control data acquisition in these experiments. A screenshot of the LabVIEW VI used to control the DAQ is shown in Fig. 2.14.

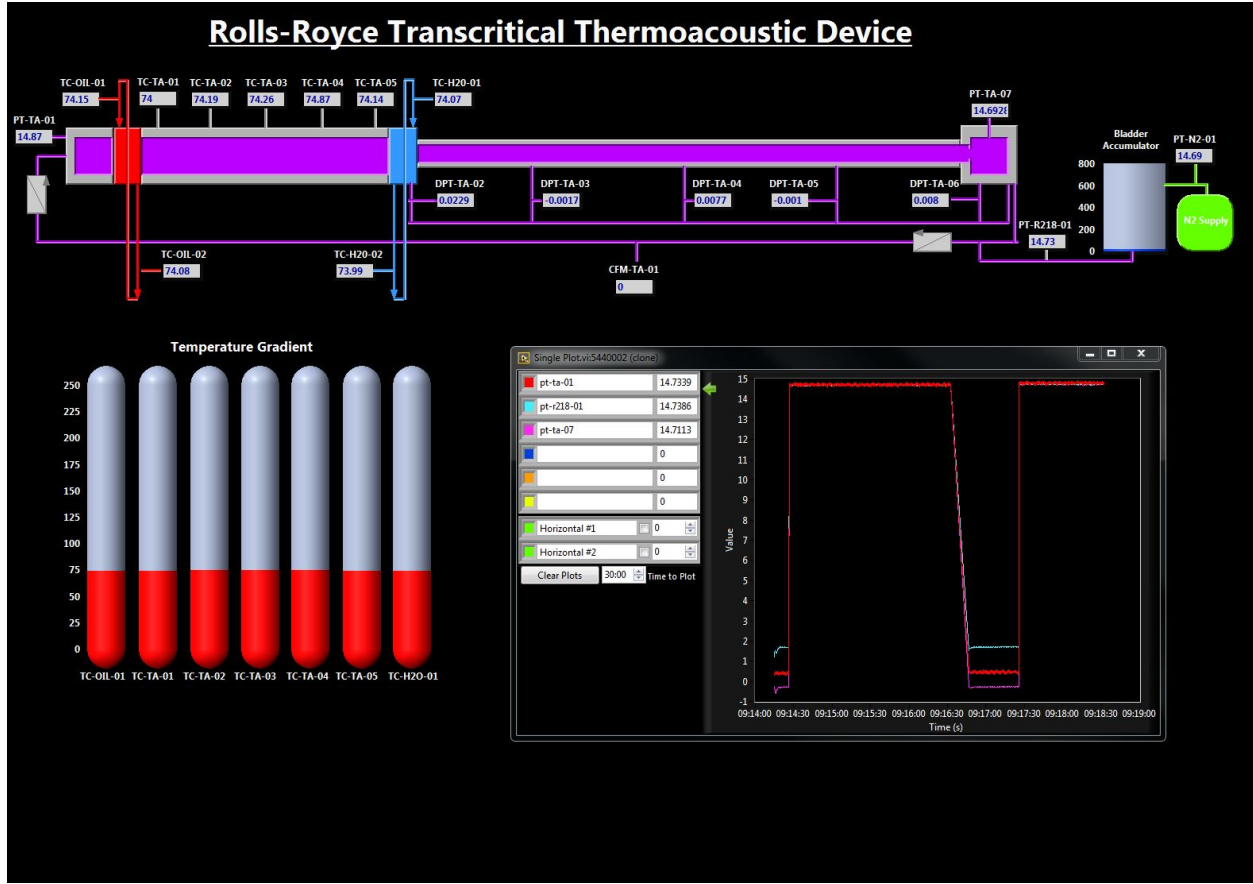


Figure 2.14. LabVIEW VI used to record and observe data during testing [21]

The heat exchanger has ports for inlet and outlet thermocouples on for each fluid connection intended to measure total ΔT as well as 5 thermocouples placed axially along of the heat exchanger intended to measure the temperature gradient from the hot side to the cold side of the device. All thermocouples used were OMEGA type-K thermocouples (GKMQSS-062G-6).

The entire rig is equipped with pressure readings along the length. There are two absolute pressure transducers on the rig, 1 Kulite pressure sensor (ETL-GTS-B-190-2000A), and one Unik 5000 (PMP50E6-TB-A3-CA-H0-PE-1000PSIA). The Kulite pressure transducer, which can withstand higher temperatures than a Unik 5000, is placed in the hot side cavity. The Unik 5000 absolute pressure transducer is placed in resonator section 3. The two absolute measurements on either end of the rig provide a measurement of both total pressure drop over the rig and bulk pressure in the rig. The resonator section is equipped with 5 Unik

5000 300psid differential pressure transducers (PMP50E6-TD-A3-CA-H0-PG, 0 to 300 psid, w/w), 1 in resonator section 1, 3 in resonator section 2, and 1 in resonator section 3. The rig has an isolation valve attached to resonator section 3 which closes off one side of the differential pressure transducers from the resonator section. The differential sensors provide a more accurate reading than the absolute transducers of pressure oscillations during a thermoacoustic response.

2.4.1 Uncertainty Analysis

Uncertainty in measurement is a gauge of the agreement between an experimentally measured value and its true value. To understand the reliability of all measurements taken during testing, an uncertainty analysis was performed to obtain a range of values in which the true value may lie. Uncertainty is broken into two components referred to as bias error and precision error. Bias error encompasses systematic or non-random error. Precision error describes random error. All uncertainty results in this study are reported at a 95% confidence interval. The 95% confidence interval for uncertainty is given by equation 2.1. Here the subscript r refers to the sample of data used to construct the confidence interval. For example, U_{DPT} may refer to the uncertainty in a sample of DPT data.

$$U_r^2 = B_r^2 + P_r^2 \quad (2.1)$$

To construct a confidence interval for total uncertainty, confidence intervals for both bias and random error need to be constructed. Equation 2.2 gives the equation for constructing a confidence interval for precision error for large sample size ($n \geq 10$) [31].

$$P_{\bar{X}_i} = \frac{2\sigma_{\bar{X}_i}}{\sqrt{n}} \quad (2.2)$$

To construct precision confidence intervals, Eq. 2.2 is applied to a steady-state sample of measured data from each pressure transducer and thermocouple for 3 separate tests. A precision interval for each instrument is computed for each test, and the precision interval per instrument is then averaged over the 3 tests. The 3 test average precision interval for

each DPT is then averaged between all of the DPTs to obtain an average precision interval for all DPTs. The same process is applied to the thermocouples. The absolute pressure transducer intervals are taken from the 3 test average, as they are both separate models.

To obtain a precision interval for frequency, the period between local pressure peaks reported by the Kulite pressure transducer over the same steady state intervals used to compute precision for pressure and temperature measurements is computed. The frequency is obtained by taking the reciprocal of the period. Then, Eq. 2.2 is applied to the frequency measurements to obtain a precision interval.

Bias error confidence intervals are collected from instrument manufacturers. From the OMEGA thermocouple probe datasheet, the type-K thermocouples used have an accuracy of $\pm 2.2C$. From GE Druck, both the absolute and differential pressure transducers have an accuracy of $\pm 0.04\%$ FSO. From Kulite, the Kulite pressure transducer has an accuracy of $\pm 0.1\%$ full spectrum operation (FSO). No bias error is reported for frequency measurement as it depends only on time.

Applying equations 2.1 and 2.2 to a sample of steady-state test data and manufacturer bias interval data gives an uncertainty interval for each measurement. Table 2.4 shows the bias, precision, and uncertainty confidence intervals for each measurement taken during testing.

Table 2.4. Uncertainty Confidence Intervals

Measurement	B_r	P_r	U_r
Temperature (K)	± 2.2	± 0.0114	± 2.2
Frequency (Hz)	± 0	$\pm 2.72E-5$	$\pm 2.72E-5$
Unik Absolute Pressure (kPa)	± 2.76	± 0.112	± 2.76
Unik Differential Pressure (kPa)	± 0.827	± 0.0772	± 0.831
Kulite Absolute Pressure (kPa)	± 20.7	± 0.144	± 20.7

This analysis shows that precision error in measurement is largely negligible, likely due to the fact that sample rate was significantly higher than frequency of change in both temperature and pressure. The temperature during testing was intended to remain constant, and

pressure fluctuations reached a maximum of $13Hz$ over all tests while the pressure sample rate was $2000Hz$.

Uncertainty in these measurements can be translated into uncertainty in important test quantities. Table 2.5 lists the average computed uncertainty in each important quantity.

Table 2.5. Measurement Uncertainty

Parameter	Uncertainty
ΔT (K)	± 4.4
f (Hz)	$\pm 2.72E-5$
P (kPa)	± 8.1

3. EXPERIMENTAL RESULTS

Over the summer and fall of 2020, a total of 114 tests were conducted looking into both the repeatability of previous experiments and effects of resonator geometry on the thermoacoustic response of transcritical R-218. Table 3.1 summarizes all conditions tested in each study.

Table 3.1. Test Campaign Summary

Test Numbers	Test Goal	Variables	Range
1-22	Assess repeatability of previous test results.	$\frac{P}{P_{cr}}$ ΔT	0.9 - 1.1 79K - 120K
23- 114	Assess effects of resonator length, diameter, and removal of coils on the thermoacoustic response of R-218.	l_{res2} D_2 ΔT	55.88 - 177.80cm 0.457 - 0.704cm 80K - 120K

Section 3.1 discusses testing and analysis methods, section 3.2 discusses the study investigating repeatability of previous results, section 3.3 discusses the study into the effects of thermoacoustic engine geometry on performance, and section 3.4 discusses the method used to analyze a leak which occurred in the heat exchanger during testing.

3.1 Testing and Analysis Methods

To ensure safe testing operation and accurate testing results, a specific procedure was followed for handling R-218 and for preparing the rig for testing. A full list of procedures is located in Appendix A. Since the rig was operated at high pressure and because R-218 is a greenhouse gas regulated by the Environmental Protection Agency (EPA), extra safety precautions were observed when preparing the rig for test.

Each time the rig needed to be filled with R-218, the rig was first checked for leaks by pressurizing with nitrogen to approximately 125% of the desired bulk pressure for the test. Leaks were discovered in one of three ways: observation, usually sound, manual investigation using SNOOP Liquid Leak Detector, or by observing pressure measurements in the rig over time. Once no leaks were detected in the system, the nitrogen was evacuated using a vacuum

pump and R-218 was loaded via an electric pump. Once the pressure in the rig reached a steady state, the pump was switched off and the rig was pressurized with nitrogen via the bladder accumulator, at this point, the test conductor put on safety glasses. If the rig did not reach the desired pressure, the nitrogen pressurant was vented and the R-218 in the rig was given some time to condense. After a few minutes, the pump was switched back on to load more R-218 into the rig. This process was repeated until the rig could reach the desired pressure.

Once the rig was at the required bulk pressure for the test, the R-218 supply was closed and isolated from the rig, the DPT isolation valves were closed, and the current bulk pressure was recorded. The nitrogen supply was then closed to avoid any thermoacoustic instabilities damaging the nitrogen system which was not designed to operate under thermoacoustic conditions. Once the rig reached a steady-state pressure, the water and oil supplies were turned on.

The water flow rate was calculated using the catch-and-weigh method. Three trials were performed timing how long the water took to fill 1L of a flask. The water flow rate was adjusted and measured via this method until it was within 10% of the desired flow rate, approximately 3.785LPM. The oil pump was run on its highest setting, delivering approximately 80g/s of Duratherm G to the heat exchanger in every test.

The oil and water temperatures were allowed to come up to a steady state, the ΔT across the heat exchanger was estimated by averaging the inlet and outlet thermocouples for both oil and water and computing the difference. The bulk pressure was estimated by averaging the pressure over approximately one minute using PT-TA-01, the Kulite pressure sensor. Once all test conditions were met, data logging was initiated, temperature readings were taken at 80Hz and pressure readings were taken at 2000Hz. Finally, the standing wave valves were closed. Once the valves were closed, the thermoacoustic response of the R-218 was allowed to reach steady-state and operate there for approximately one minute, the valves were then closed and data logging was stopped. Each condition was tested a minimum of 3 times to ensure repeatability of results.

Once testing was completed for a given set of conditions, the water and oil supplies were shut off and the rig was allowed to cool for a few minutes. When ΔT was low enough that

the R-218 was no longer responding thermoacoustically, the rig was depressurized partially by venting the nitrogen from the bladder accumulator. The remaining pressure in the rig was used to drive R-218 back into the storage system with the assistance of the electric pump. The rig was deemed empty once the absolute pressure measurements in the rig were reading a partial vacuum, between 34-48kPa. After the R-218 was unloaded and stored in the reclamation tank, the seal on the test section of the rig could be broken to make changes.

Oscillation frequencies experienced in the rig were computed using an FFT and plotting the results. The fundamental frequency was determined by picking the lowest frequency peak on the FFT plot. In all cases, the lowest frequency peak was also the most powerful, which supports the method for defining the fundamental frequency of the thermoacoustic oscillations. Pressure amplitudes in the rig were determined by passing a steady-state interval of pressure data to a minimum-order filter with a stopband attenuation of 60 dB with a passband frequency of 0.5 to 1.5 times the fundamental frequency of the oscillation. The RMS of the filtered pressure was then computed to eliminate negative peaks and the pressure amplitude was taken as twice the average of all local peaks of the filtered root-mean-square (RMS) data.

3.2 Study on Repeatability of Previous Results

The first study performed was an investigation of the repeatability of Martinez’s results [21]. All tests in this section were performed using a resonator length of 80in, a resonator diameter of 0.18in, and with coils in resonator 2. Table 3.2 lists all conditions originally intended to be tested.

Table 3.2. Repeatability Campaign Test Conditions

Parameter	Value		
$\frac{P}{P_{cr}}$	0.9	1.0	1.1
$\Delta T[K]$	79	105	120

Although the rig has been tested at both higher ΔT and $\frac{P}{P_{cr}}$, they were both limited for this study to avoid over-exerting the hardware which had already been through a previous test campaign.

Not every condition in Tab. 3.2 was tested. After testing all pressures at $\Delta T = 79\text{K}$, and all ΔT at $\frac{P}{P_{cr}} = 1.1$, it was determined that further evidence of repeatability was unnecessary. Each condition was tested from 3 to 5 times to ensure that the results had an acceptable level of precision.

3.2.1 Repeatability of Results

To characterize the agreement of fluid conditions between Martinez’s study and the repeatability study, the bulk pressure, ΔT , pressure amplitude, and frequency recorded for each test were taken and the percent deviation from the value reported in Martinez’s study was calculated using Eq. 3.1.

$$C = \frac{x_e - x_t}{x_t} * 100 \quad (3.1)$$

Where x_e is the experimental value, x_t is the target value, and C is the relative percent difference between the two values. Table 3.3 lists the average deviation from the target value for all fluid characteristics during the repeatability testing.

Table 3.3. Percent Variance of Test Conditions from the Target Value in the Repeatability Study

Parameter	Variance from Target Value (%)
$\frac{P}{P_{cr}}$	1.4
ΔT	0.68
P_{max}	16.6
f	8.6

While the fluid conditions set before testing, $\frac{P}{P_{cr}}$ and ΔT were matched quite closely to Martinez’s study, the pressure amplitude and frequency obtained in testing varied more

significantly from the target values. This is due to the fact that the change in pressure amplitude observed when varying $\frac{P}{P_{cr}}$ is within the uncertainty range of the Kulite pressure transducer used to measure maximum pressure amplitude. When varying ΔT and holding $\frac{P}{P_{cr}}$ constant, however, the change in maximum pressure amplitude is larger than the uncertainty in the Kulite. In the current rig configuration, a Kulite pressure transducer is installed on the hot side cavity because of its ability to withstand higher temperatures. The Kulite, however, has a higher degree of uncertainty than the Unik pressure transducers.

It should be noted that while the percentage variation from the target values in both P_{max} and f are significant, since the target value for both parameters was quite small, the actual difference was relatively small. In frequency, on the order of ± 0.4 - 0.5 Hz and in pressure amplitude, on the order of ± 40 - 80 kPa.

3.2.2 Waveform Comparison

To form a more complete picture of the comparison between Martinez's results and the results of the repeatability study, the waveform of the thermoacoustic instabilities inside the rig were computed and compared. The waveforms reported in this section were plotted using average steady-state pressure amplitudes for each condition tested. Figure 3.1 gives the locations of each pressure transducer along the rig.

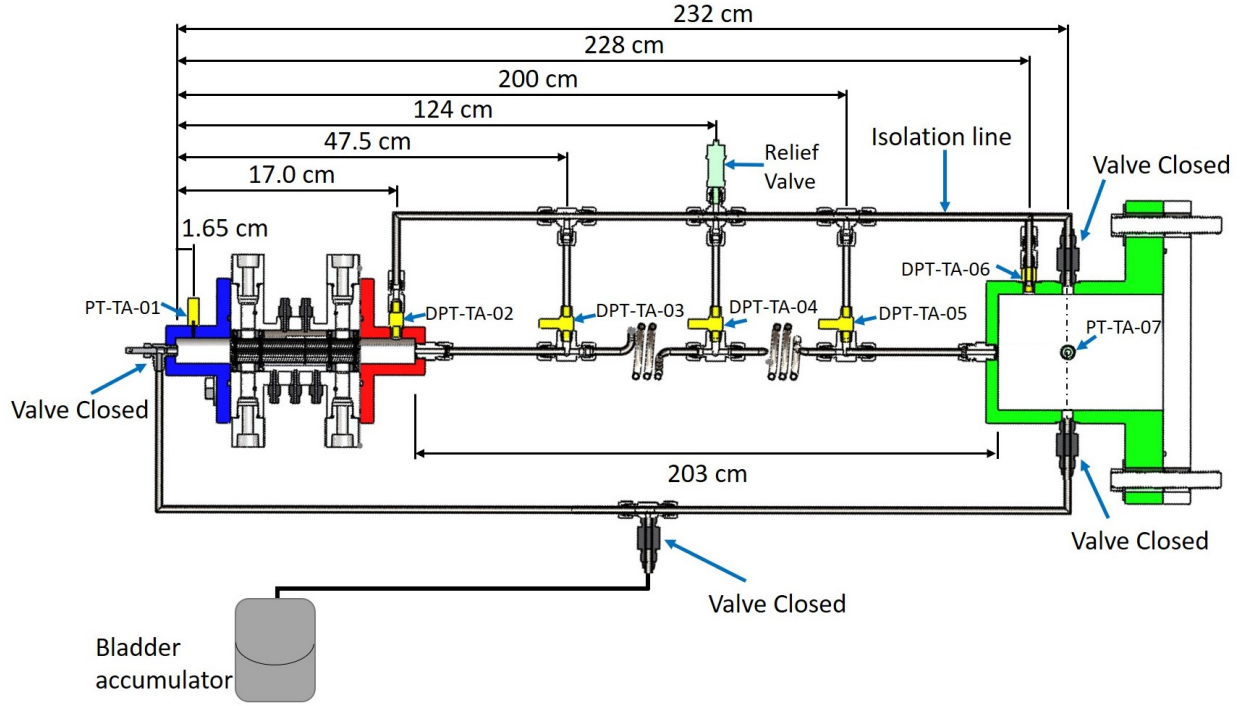


Figure 3.1. Location of each pressure transducer measured from the top of the hot side cavity [21].

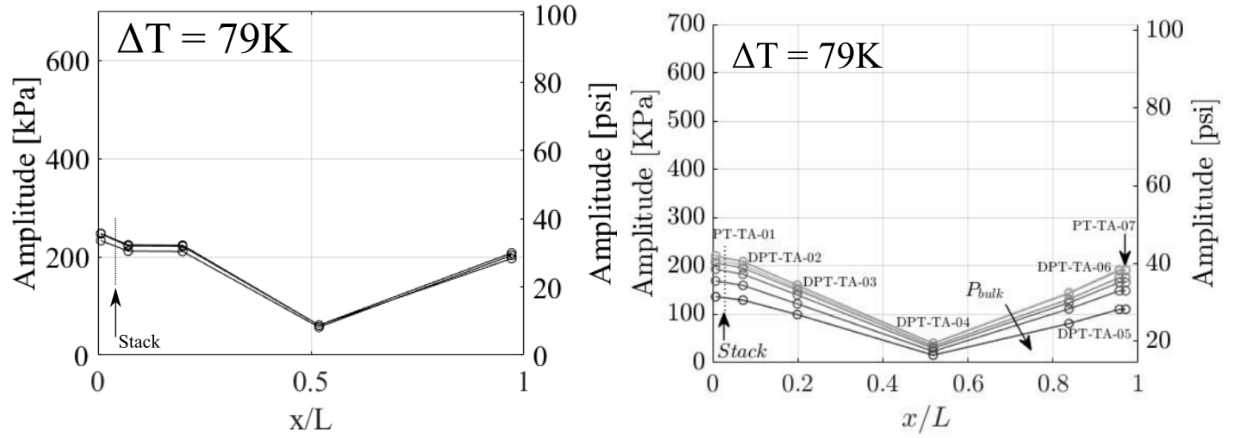


Figure 3.2. Comparison between (left) waveform from current testing at various pressures and a temperature difference of 79K compared to (right) waveform from Martinez's testing at various pressures and a temperature difference of 79K [21]. The x axis shows each pressure transducer's location along the rig normalized by the rig length $L = 239\text{cm}$. The y axis shows average steady-state pressure amplitude as measured by each instrument. A bulk pressure trend is not included on the left plot because there is not enough data to establish a trend in bulk pressure.

Figure 3.2 shows a comparison between the waveform measured in the current repeatability testing and the waveform measured in Martinez’s testing. The trend is similar with pressure amplitude decreasing to the midpoint of the rig and increasing beyond that. There was little decrease in pressure amplitude measured between positions 2 and 3 in the current testing. The heat exchanger was experiencing some leakage issues which may explain this discrepancy. The amplitudes are also similar, with a maximum of just over 200kPa at the hot-side cavity and a minimum of approximately 70kPa at the midpoint of the rig. DPT-TA-05 and DPT-TA-06 are omitted from the left plot. The measurements these instruments were reporting were suspicious and evaluation of both pressure transducers showed that they were not functioning.

3.3 Parametric Study on Resonator 2 Length and Diameter

The second study performed was an investigation into the effects of resonator section geometry on the thermoacoustic response of R-218. All tests in this campaign were performed at $\frac{P}{P_{cr}} = 1.1$. Table 3.4 lists all conditions tested in this study.

Table 3.4. Parametric Study on Resonator Length and Diameter Test Conditions

Parameter	Value		
$\Delta T[K]$	80	100	120
$l_{res2}[m]$	0.559	1.02	1.78
$D_2[cm]$	0.457	0.622	0.704

3.3.1 Condition Repeatability

To understand how consistent test conditions were between all tests in this study, both $\frac{P}{P_{cr}}$, and ΔT were recorded for each test and compared to the target test condition. Table 3.5 lists the average percent deviation from the target test value for the study on resonator length.

Table 3.5. Percent Variance of Test Conditions from the Target Value in the Resonator Length and Diameter Study

Parameter	Variance from Target Value (%)
$\frac{P}{P_{cr}}$	0.42
ΔT	0.43

The variation in fluid condition between tests in this study is minimal.

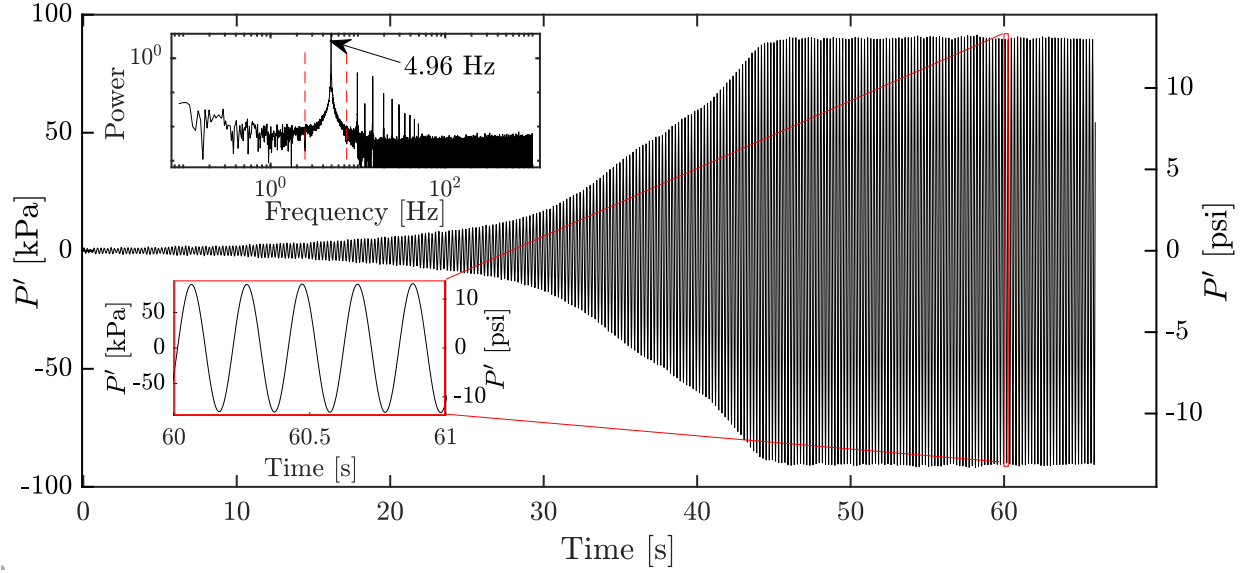


Figure 3.3. Waveform from tests with coils in resonator 2. The case shown is from a test at a temperature difference of 79K, and a bulk pressure over critical pressure of 1.13. The top-left insert shows the power spectral density plot of the test, red lines indicate the range of the bandpass filter. The bottom-left insert shows a zoomed in picture of the waveform [32].

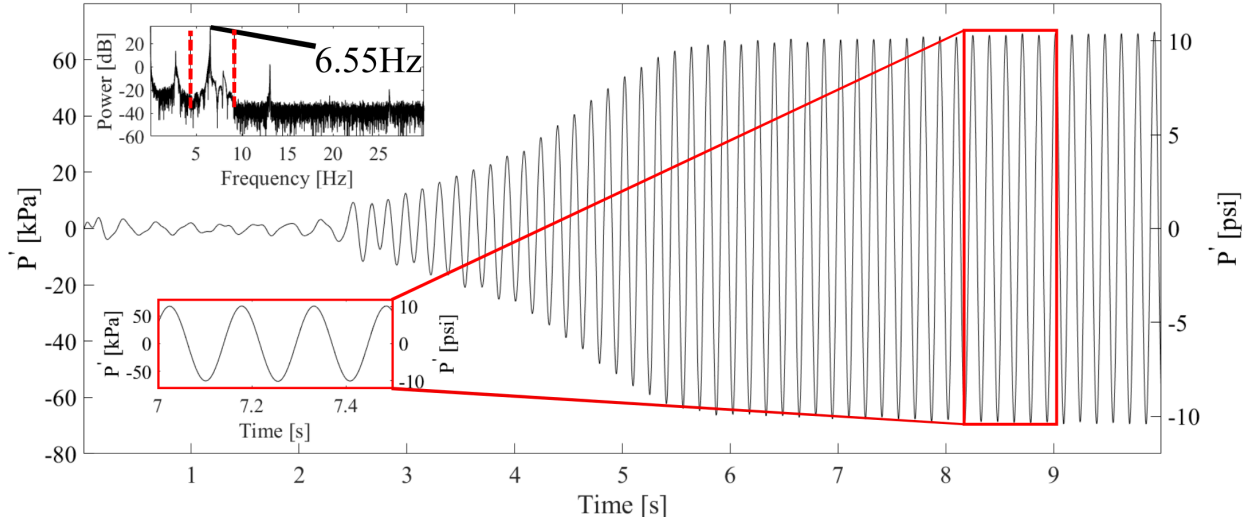


Figure 3.4. Typical waveform from tests without coils in resonator 2. This test was performed at bulk pressure over critical pressure of 1.11, a temperature difference of 100K, resonator 2 length of 1.78m, and resonator 2 diameter of 0.704cm. These plots illustrate the typical bandpass filtered waveform and power spectral density plots obtained from the Kulite pressure sensor on the hot-side cavity.

Figures 3.3 and 3.4 illustrate the typical waveform from tests with and without coils in resonator 2 respectively. Both figures exhibit classical exponential growth with signal saturation at a highly periodic limit cycle. They both have a power spectral density with a strong peak at the fundamental frequency with some higher frequencies at lower power. From these figures, it can be determined that the fundamental anatomy of the pressure signal has not been significantly altered by changing length, diameter, or by removing coils from resonator 2, therefore, comparisons can be drawn between the results of this study and previous studies.

3.3.2 Influence of Resonator Length and Diameter

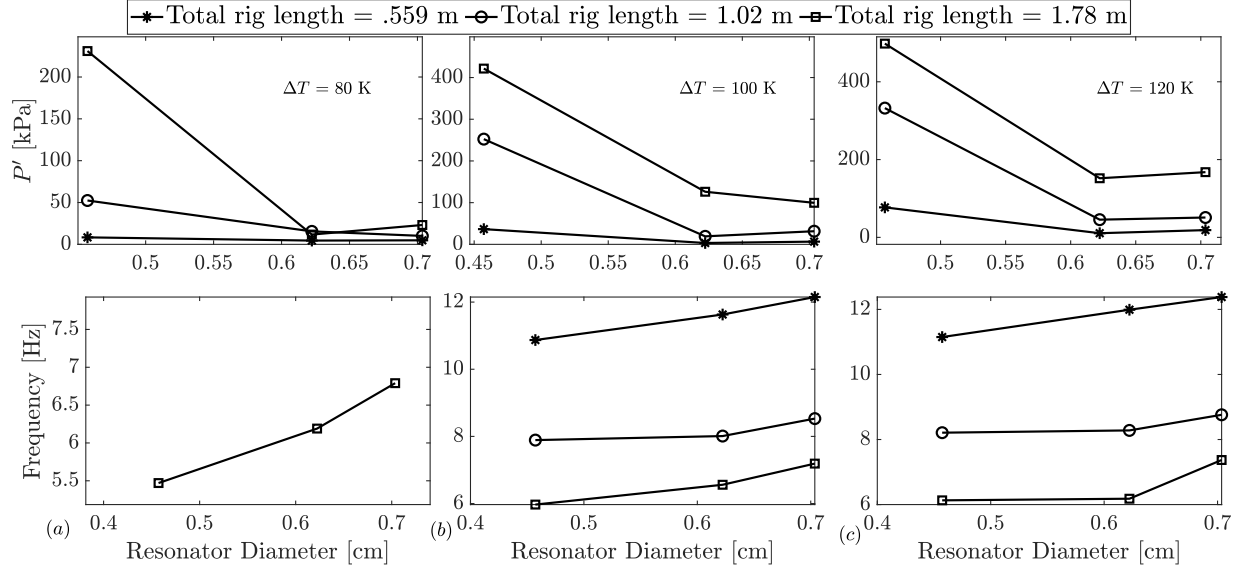


Figure 3.5. Frequency and average steady-state pressure amplitude for (a) a temperature difference of 80K, and bulk over critical pressure of 1.1, (b) a temperature difference of 100K, and bulk over critical pressure of 1.1, and (c) a temperature difference of 120K, and bulk over critical pressure of 1.1. Both quantities are plotted against resonator diameter and line markers indicate total rig length. Average steady-state pressure amplitude increasing as total rig length increases and decreasing as resonator 2 diameter increases. Operational frequency decreases as total rig length increases and increases as resonator 2 diameter increases [32].

Figure 3.5 shows the results of the parametric study on resonator 2 length and diameter. In a standing wave device, the wavelength is set by the length of the resonator being used. As the device gets longer, wavelength increases. The first resonant mode for a standing wave device of length L with speed of sound in the working medium, a , is given by Eq. 3.2.

$$f = \frac{a}{2L} \quad (3.2)$$

This approximation is valid for a device with no dissipation, nonlinear effects, or geometry changes. As resonator length, and therefore wavelength, increases, frequency must decrease and velocity must increase. In an acoustic wave, as the maximum velocity increases, so

does the maximum pressure amplitude. These maxima will not occur at the same location, because in an acoustic wave velocity nodes are pressure anti-nodes, but the maximum velocity and pressure amplitude will increase together.

The behavior described by Fig. 3.5 deviates from the behavior predicted by Eq. 3.2. Theory suggests that the scaling of measurements in Fig. 3.5 both between length changes and diameter changes should be linear. The deviation of measurements from theory suggests that some nonlinearities are occurring in the TTE. These deviations can be explained by a few different mechanisms.

Engine geometry and fluid performance are strongly coupled in thermoacoustic devices. Increasing the length of resonator 2, and therefore increasing the wavelength, decreases the effects of axial geometry on thermoacoustic production. As L goes to infinity, the approximation of frequency made by Eq. 3.2 becomes more accurate. By this logic, changing the length of resonator 2 may put the TTE in different geometry regimes which have varying effects on fluid performance. Geometry changes may also modify the phasing of the engine which can affect the thermoacoustic production of the device.

The trend in resonator diameter can be explained by a few competing effects. First, changing the geometry of the engine, as stated before, can greatly affect thermoacoustic production. Second, increasing the diameter of resonator 2 significantly increases the mass of R-218 in the system. A larger mass of R-218 in the system requires a larger thermal energy input to excite thermoacoustic instabilities in the fluid. Finally, varying the diameter of resonator 2 will have an effect on $\frac{A_{res2}}{A_{res3}}$, the area ratio between resonator 2 and resonator 3, which will affect the pressure drop experienced across that area change.

These three factors are coupled in various ways. Increasing the diameter of resonator 2 will increase the mass of R-218 the rig needs to drive, but it will also increase $\frac{A_{res2}}{A_{res3}}$ which will decrease the pressure drop across the resonator 2 to resonator 3 boundary. Increasing the diameter of resonator 2 also modifies the thermoacoustic production of the rig. The coupling of these factors gives rise to a complicated interaction which merits more investigation.

Lacking measurements of flow velocity and heat required to excite thermoacoustic instabilities, it is impossible to directly report the amount of acoustic power developed in the rig. Fig. 3.5 shows that the rig is still able to obtain a sustained thermoacoustic response

using a larger diameter tube in resonator section 2. The model developed by Migliornio and Scalo [33] estimates, using the results from Fig. 3.5, that increasing resonator length and diameter both increase the acoustic power developed in the rig. Increasing the length of the resonator, from Fig. 3.5, increases pressure amplitude, which in turn increases acoustic power. Although pressure amplitude goes down when diameter increases, the volumetric flowrate inside the rig increases which may increase the acoustic power developed in the rig. Further investigation is required to quantitatively determine the rig configuration which develops the most acoustic power.

3.3.3 Influence of Coils

As part of the parametric study on resonator 2 length and diameter, the coils tube sections used in Martinez's study were replaced in favor of straight sections. It was hypothesized that removing coils from resonator 2 would increase the pressure amplitudes seen in the rig at similar frequencies to the coiled configuration due to a reduction in viscous losses in the resonator section. Figure 3.6 shows a comparison of frequency and pressure amplitudes obtained during tests with and without coils. These measurements confirm that coils in resonator 2 do attenuate the pressure signal.

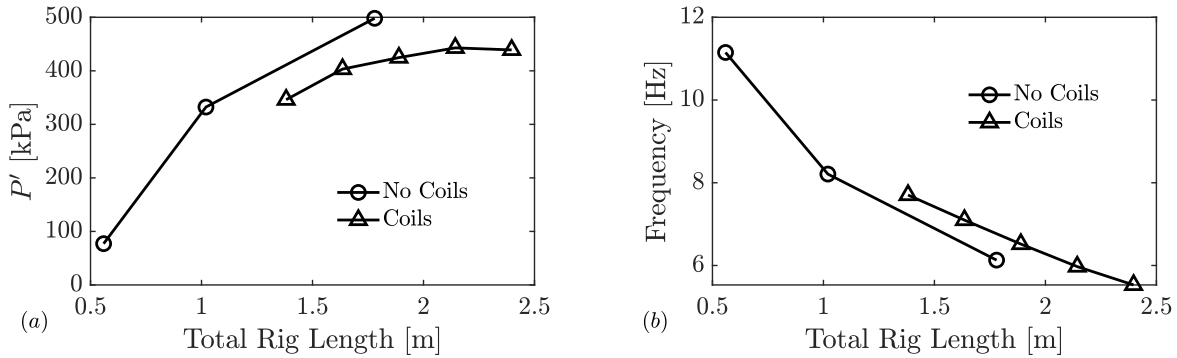


Figure 3.6. (a) Pressure amplitude and (b) frequency measured in resonator 2 with and without coils. All tests were conducted at bulk over critical pressure of 1.1 and a temperature difference of approximately 118K. The rig without coils produces a higher pressure amplitude across all resonator lengths while exhibiting only a minor decrease in operational frequency [32]

The minor decrease in frequency is likely due to boundary layer effects. In a coiled tube, the centrifugal force applied to the while is is turning through the coil creases a local pressure gradient between radially across the tube. This pressure gradient develops a secondary eddy flow which circulates radially and affects the frequency of the acoustic wave. In a straight tube, this boundary layer effect is not present.

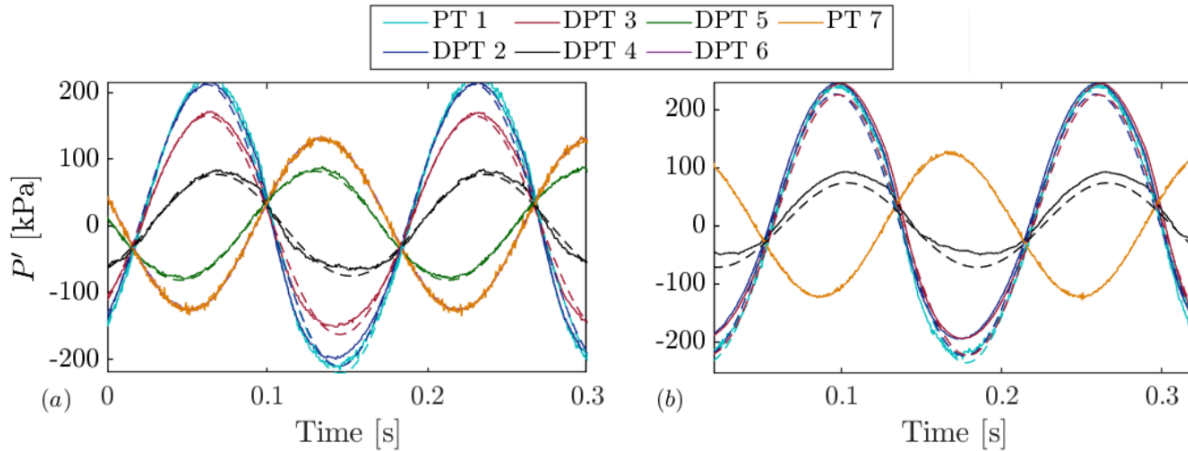


Figure 3.7. Comparison of pressure traces between (a) test 66, conducted at a bulk over critical pressure of 1.09 and a temperature difference of 116K with coils in resonator 2, and (b) test 49, conducted at a bulk over critical pressure of 1.1 and a temperature difference of 120K. Solid lines depict raw data translated to be centered around zero. Dashed lines represent bandpass filtered data [32].

Figure 3.7 gives a comparison between pressure traces on each instrument for tests both with and without coils. Again, DPT 5 and DPT 6 have been omitted from reporting in the current study. Tests without coils exhibit a significant wave steepening effect which suggests that removing coils, thereby reducing viscous losses in resonator 2, does decrease acoustic wave attenuation.

3.4 Leak Rate Analysis

After the parametric study on resonator length and resonator tube diameter was completed. More tests were carried out to investigate outstanding questions on the effects of resonator tube diameter. First, a long duration test was performed to determine if pressure

oscillations in a larger resonator tube diameter required more time to reach a limit cycle. During this test, a small leak developed in the system. Figure 3.8 shows the pressure trace of the test where the leak was noticed.

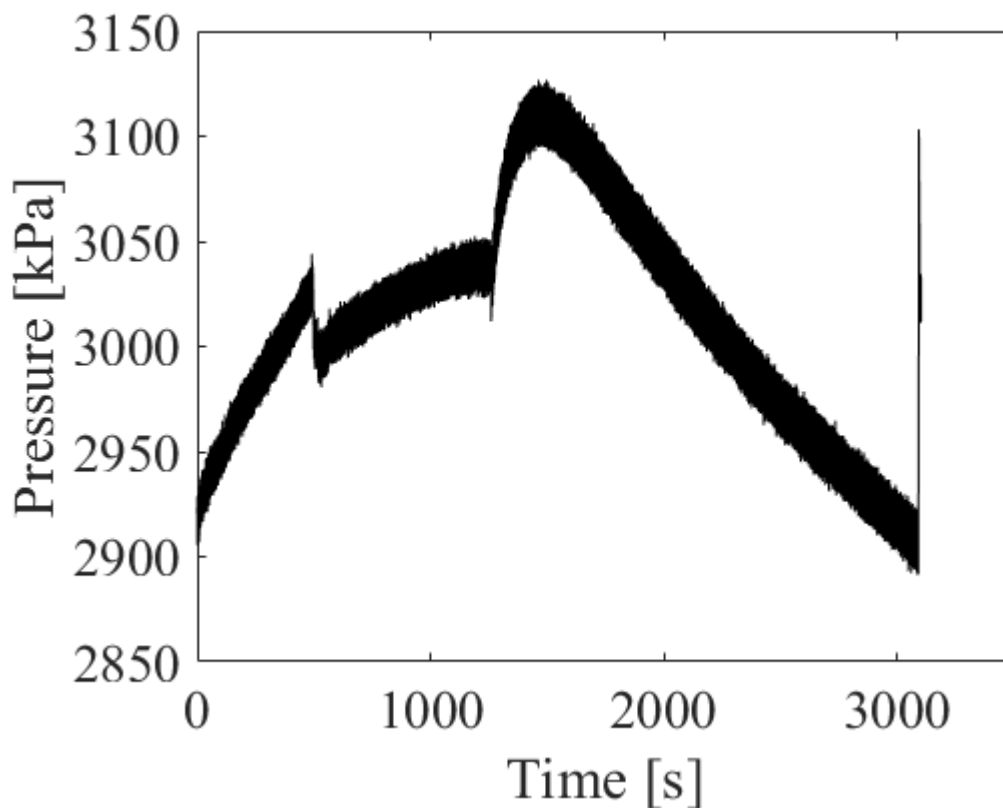


Figure 3.8. Pressure trace of long duration test. Up to 1500 seconds, the rig is being heated to excite thermoacoustic instabilities. The standing wave valves are closed at 1250 seconds, isolating the rig from pressure supply, and the rig is allowed to operate for approximately an additional 30 minutes. Just past 3000 seconds, the valves are opened back up and the rig pressure comes back up to the supply pressure.

After the test, the R-218 was reclaimed from the system and the system was pressurized with nitrogen up to 450psi in increments of 50psi to check for leaks. No leaks were detected in any of the fittings or instrumentation. Using previous experience from Martinez's experiments, it was determined that the heat exchanger was leaking. To determine if it was safe to continue testing, the following analysis was performed to calculate the extent of the leak.

To begin characterizing the leak, first, it was necessary to understand how the density of R-218 changes with both temperature and pressure. Figure 3.9 shows how the density of R-218 changes with pressure and temperature.

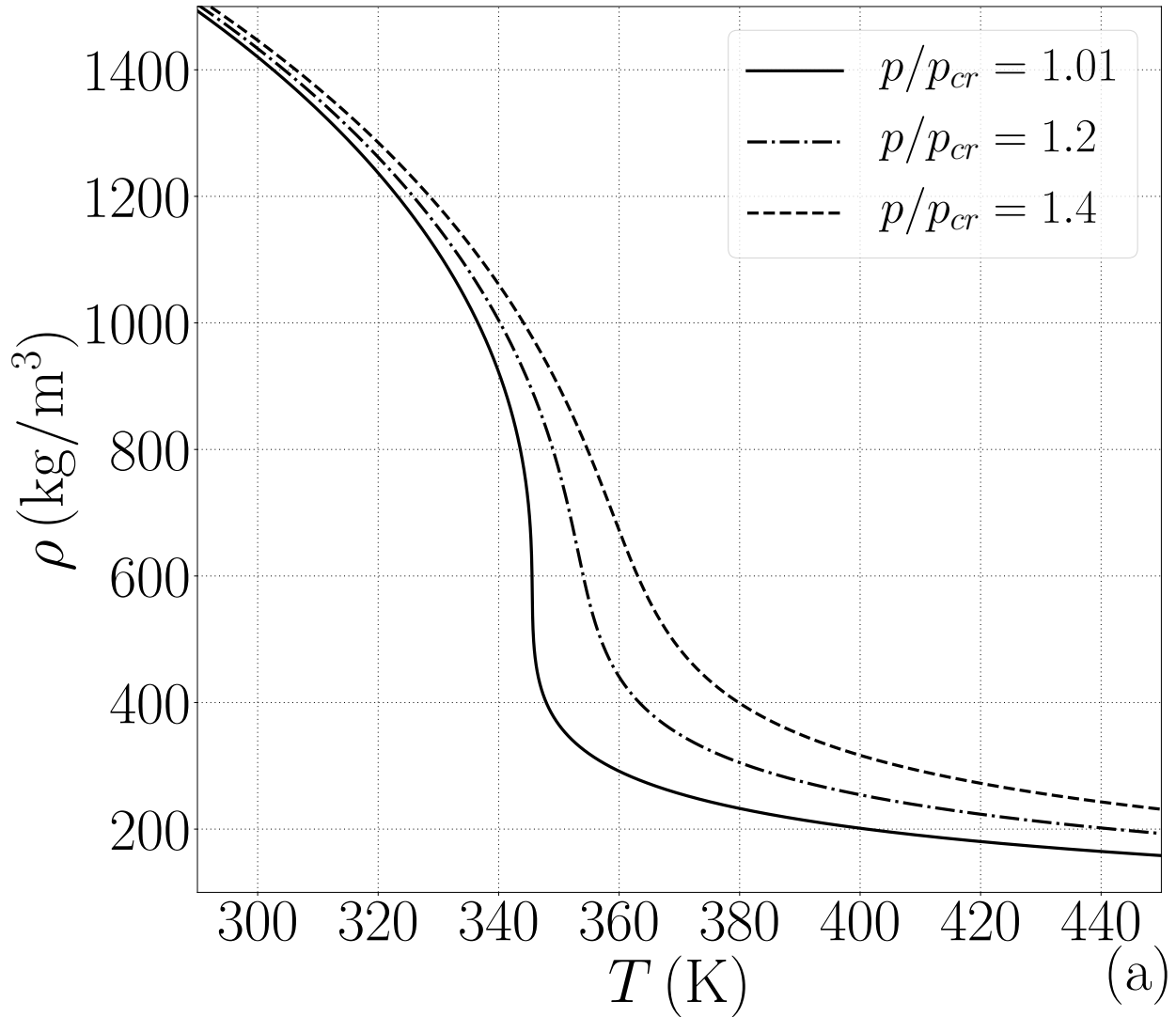


Figure 3.9. Density of R-218 at supercritical pressures and temperatures computed using the Peng-Robinson equation of state [32], [34].

To simplify the analysis, it was assumed that the leak was coming from the hot side of the heat exchanger. This assumption was made because the seal on the hot side of the heat exchanger was under a much larger thermal load and could reasonably be assumed to have failed before any other seal. Using this assumption, the analysis could be performed using

a constant temperature. The hot side cavity of the heat exchanger was selected as a control volume. To quantify the mass flow rate of R-218 out of the leak, change in density over time needs to be quantified. The change in density over time is expressed by,

$$\frac{d\rho}{dt} = \frac{1}{V} \frac{dm}{dt} \quad (3.3)$$

Where $\frac{d\rho}{dt}$ is the change in density over time, V is the volume of the hot side cavity, and $\frac{dm}{dt}$ is the mass flow rate of the leak. Change in density over time can also be expressed by,

$$\frac{d\rho}{dt} = \frac{dP}{dt} \left. \frac{\partial \rho}{\partial P} \right|_T \quad (3.4)$$

Where $\frac{dP}{dt}$ is the change in pressure over time, and $\left. \frac{\partial \rho}{\partial P} \right|_T$ is the change in density of R-218 over pressure evaluated at a constant temperature. Setting equations 3.3 and 3.4 equal yields an expression which can be used to determine leak rate.

$$\frac{dm}{dt} = V \frac{dP}{dt} \left. \frac{\partial \rho}{\partial P} \right|_T \quad (3.5)$$

V was obtained from the geometry of the heat exchanger, $\frac{dP}{dt}$ was measured during the test, and $\left. \frac{\partial \rho}{\partial P} \right|_T$ was determined from test data.

Figure 3.10 shows the pressure trace of nitrogen during the leak rate test.

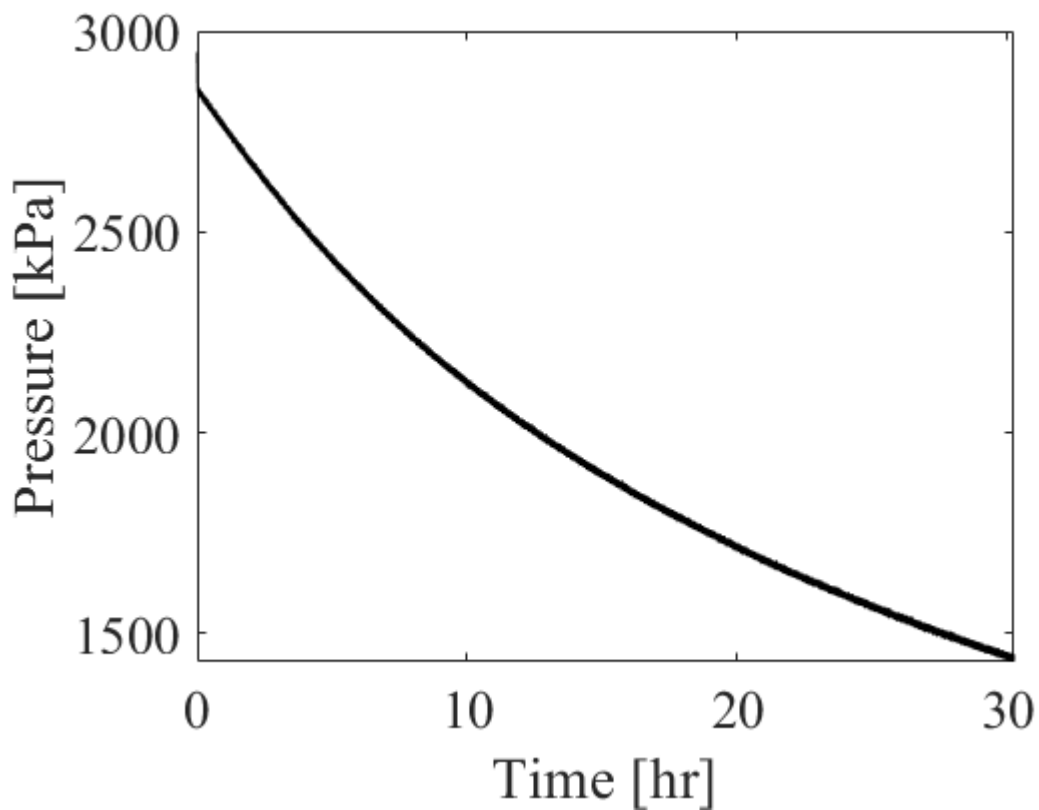


Figure 3.10. Nitrogen pressure during the leak rate test. The nitrogen was pressurized to approximately 3000kPa and allowed to leak out for 30 hours.

Mass flow rate varies directly with pressure since there are no sonic orifices in the rig, so the flow rate is never constant, but for the duration of the test it remains on the order of 10^{-8} kg/s. After this analysis was performed it was determined it was safe to continue testing with R-218 given the leak was so slow and only occurred when the heat exchanger was exposed to high temperatures. As before, to mitigate leakage, the R-218 was reclaimed from the system after each testing day was complete.

4. BIDIRECTIONAL TURBINE DESIGN

After significant progress was made on characterizing the thermoacoustic performance of R-218 and the effects of TTE geometry were investigated, work began on designing a device to extract energy from the TTE. There are a significant number of methods to extract energy from a thermoacoustic engine. Based on the previous work on R-218 from Martinez [21] and the work on bidirectional turbines in thermoacoustic engines by Timmer, et al. [28], and de Blok, et al. [27], it was decided that an axial bi-directional impulse turbine should be designed for use in energy extraction in the TTE. The following chapter contains in section 4.1 the motivation behind designing a bi-directional impulse turbine for this application. In section 4.2 a discussion of preliminary analyses performed to understand the turbine's operational domain is presented. Using the relations derived in section 4.2, a case study was performed on a published turbine in section 4.3. In section 4.4, the mechanical design of the turbine is discussed. Finally, in section 4.5 a proposed experiment to test the turbine is developed.

4.1 Motivation

Little research has been done investigating bi-directional turbines for TAE applications. As discussed in section 1.2.4, de Blok et al. were the first to implement a bi-directional impulse turbine in a TAE in 2014. To date, no bi-directional turbine in TAE applications has been implemented with high density fluids. de Blok predicted, shown in Fig. 1.12, that bi-directional impulse turbines could see significant improvements in rotor efficiency when working with high density fluids.

4.2 Preliminary Analyses

Before beginning the mechanical design of the turbine, several preliminary analyses were performed to understand the operational envelope of the turbine. The first step in developing useful relations for design was to define the velocity triangles for this turbine. Figure 4.1 shows the velocity triangles defined for a bi-directional impulse turbine.

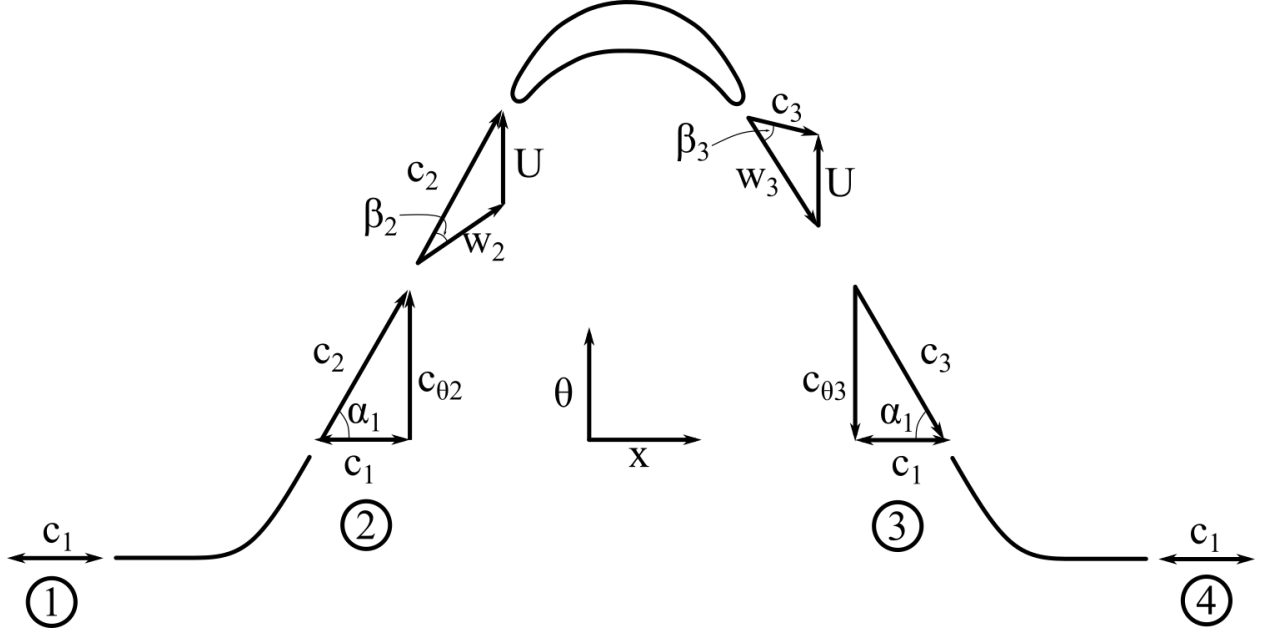


Figure 4.1. Velocity triangles for an impulse turbine. For the bi-directional impulse turbine, the upstream and downstream stator are identical and mirrored about the vertical axis.

The diagram is broken into four stations. Station 1 is the upstream stator inlet, station 2 is the upstream stator exit/rotor blade inlet, station 3 is the rotor blade exit/downstream stator inlet, and station 4 is the downstream stator exit. The velocity triangles are broken up into two reference frames, the absolute, or lab frame, and the relative, or rotor frame. Absolute velocities are denoted by the letter c and relative velocities are denoted by the letter w . Each c and w vector has an axial and tangential component. Axial velocity remains constant throughout the system, so it will always be denoted by the absolute inlet velocity at station 1, c_1 . Tangential velocity changes throughout the system, so, when necessary, tangential velocity components are denoted with the subscript θ . Rotor speed is denoted in this diagram as U . Two angle systems are also defined in this diagram, angles labelled α are absolute angles defined by fixed quantities. Angles labelled β are relative flow angles. For example, α_1 will maintain a fixed value regardless of the magnitude of c_1 , but β_2 will vary with changes in the magnitude of c_1 .

Before deriving relations from Fig. 4.1, three useful turbine relations need to be defined. The turbine flow coefficient, ϕ , given by Eq. 4.1, defined as the ratio of inlet axial velocity to turbine tangential rotor tip velocity, is a useful design relation.

$$\phi = \frac{c_1}{U} \quad (4.1)$$

Flow coefficient defines the stator exit angle. The second useful equation defines the relationship between absolute, relative, and rotor tip velocities. This relationship is given by Eq. 4.2.

$$\vec{c} = \vec{U} + \vec{w} \quad (4.2)$$

For any point in the turbine, absolute flow velocity is defined as the sum of the rotor tip velocity vector and the relative flow velocity vector. Turbine rotational speed given in RPM, N , is necessary for computing the power generated by the turbine. N is defined by Eq. 4.3.

$$N = U \frac{60}{2\pi r_{tip}} \quad (4.3)$$

Where r_{tip} is the radius of the rotor blade tip.

With these three equations, the rest of the velocity triangles can be defined using Fig. 4.1. First, stator exit angle is defined by Eq. 4.4.

$$\alpha_1 = \tan^{-1}\left(\frac{1}{\phi}\right) \quad (4.4)$$

Next, Eq. 4.5 gives the tangential component of absolute velocity at station 2, $c_{\theta 2}$ can be defined.

$$c_{\theta 2} = c_1 \tan(\alpha_1) \quad (4.5)$$

Using Eq. 4.2, the tangential component of relative velocity at station 2, $w_{\theta 2}$, can be defined. $w_{\theta 2}$ is given by Eq. 4.6.

$$w_{\theta 2} = c_{\theta 2} - U \quad (4.6)$$

Next, the rotor relative inlet angle β_2 is given by Eq. 4.7.

$$\beta_2 = \tan^{-1}\left(\frac{w_{\theta 2}}{c_1}\right) \quad (4.7)$$

Since this is a bi-directional impulse turbine, the rotor must be symmetrical about the θ axis, therefore β_2 must equal β_3 . Knowing this, the tangential component of relative velocity at station 3, $w_{\theta 3}$ is given by Eq. 4.8.

$$w_{\theta 3} = c_1 \tan(\beta_3) \quad (4.8)$$

Finally, the tangential component of absolute velocity at station 3, $c_{\theta 3}$ can be defined using Eq. 4.2. $c_{\theta 3}$ is given by Eq. 4.9.

$$c_{\theta 3} = w_{\theta 3} - U \quad (4.9)$$

Using the relationships derived above, several important design curves can be generated for stator exit angles ranging from 60 to 80 degrees [35]. Figure 4.2 shows a plot of rotor inlet angle as a function of stator exit angle generated by solving Eqs 4.4 - 4.7 over the given range of α_1 values.

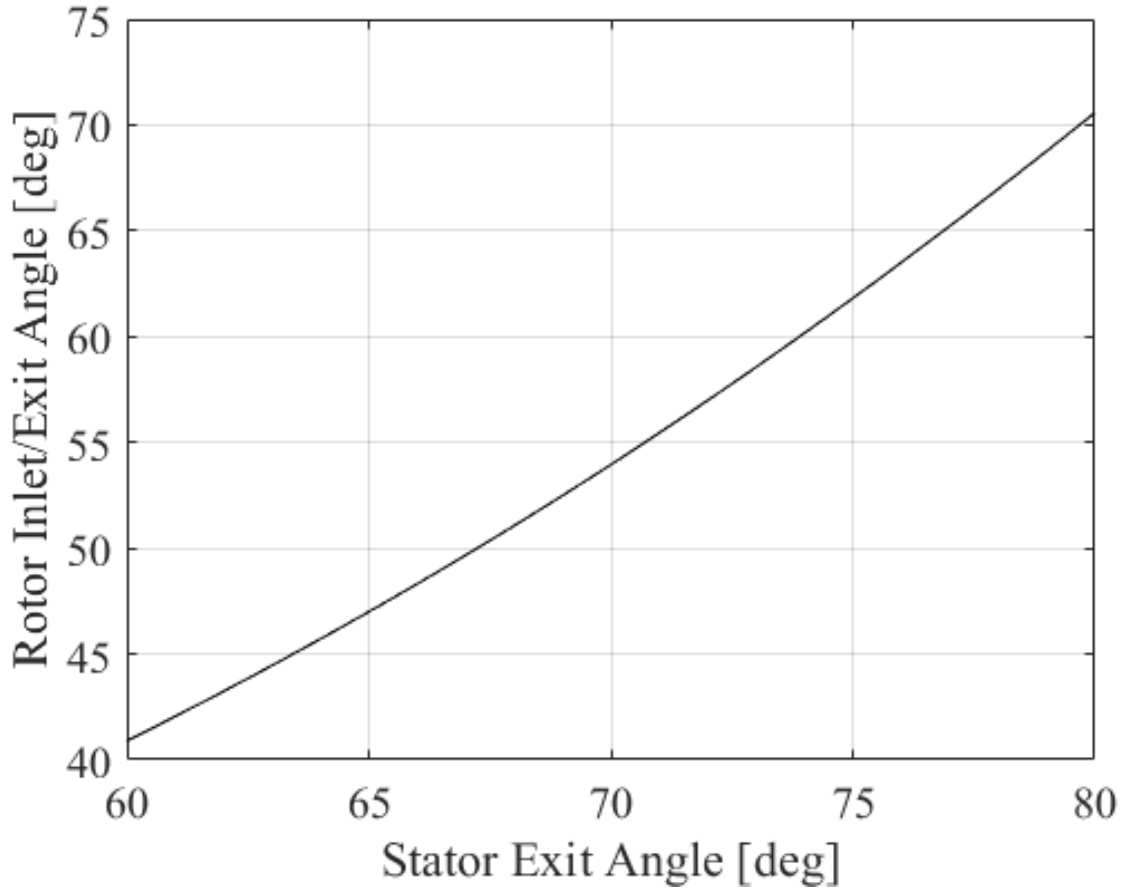


Figure 4.2. Rotor inlet angle as a function of stator exit angle. The relationship is weakly exponential with rotor inlet angle ranging between 10 and 20 degrees less than the stator exit angle.

The relationship presented in Fig. 4.2 allows a rotor inlet angle to be chosen based upon the turbine stator inlet conditions.

The next curve derived from the velocity triangles describes the relationship between stator exit angle and rotor speed. Figure 4.3, generated by solving Eqs. 4.1, 4.4, and 4.3 for a fixed turbine diameter of 60mm.

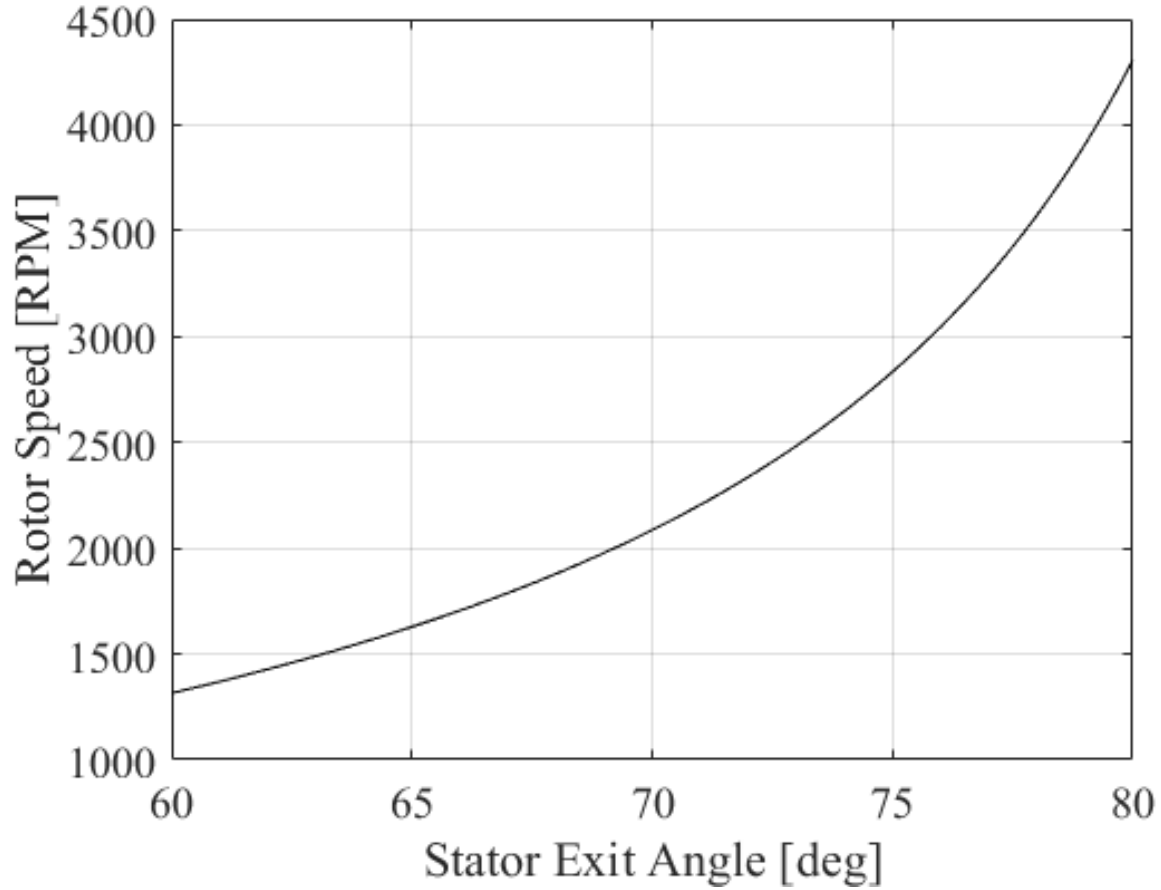


Figure 4.3. Rotational speed as a function of stator exit angle. This trend is more strongly exponential than the rotor inlet angle trend.

The trend illustrated in Fig. 4.3 is clearly exponential. Although this turbine is relatively low speed in comparison to turbines designed for other applications, for example in rocket engine turbomachinery, turbines tend to operate on the order of 5000 - 30,000RPM [36], it does operate at a higher speed than OWC turbines which is expected due to the increased working fluid density of R-218 over air used in OWC systems.

The final curve generated for design illustrates the relationship between α_1 and the ratio of pressure drop over the turbine to the available thermoacoustic pressure amplitude, referred to as $\frac{\Delta P}{P}$. $\frac{\Delta P}{P}$ is used as a measure of what percentage of acoustic power generated by thermoacoustic instabilities is extracted by the turbine. To define, $\frac{\Delta P}{P}$, a few equations

are required. Equations 4.10 and 4.11 give two ways to compute the power developed by a turbine.

$$\mathbb{P} = \dot{m}U\Delta c_\theta \quad (4.10)$$

$$\mathbb{P} = \dot{m}\frac{\Delta P}{\rho} \quad (4.11)$$

Where \mathbb{P} is the power developed by the turbine, \dot{m} is the working fluid mass flow rate, Δc_θ is the difference between $c_{\theta 2}$ and $c_{\theta 3}$, ΔP is the pressure drop over the turbine, and ρ is the working fluid density. Equating the right hand sides of Eqs. 4.10 and 4.11, an equation defining ΔP can be developed. The pressure drop over the turbine is given by Eq. 4.12.

$$\Delta P = \rho U \Delta c_\theta \quad (4.12)$$

Using Eq. 4.12 and dividing the answer by the on-design pressure amplitude of the turbine, the relationship between $\frac{\Delta P}{P}$, given by Fig. 4.4, can be established.

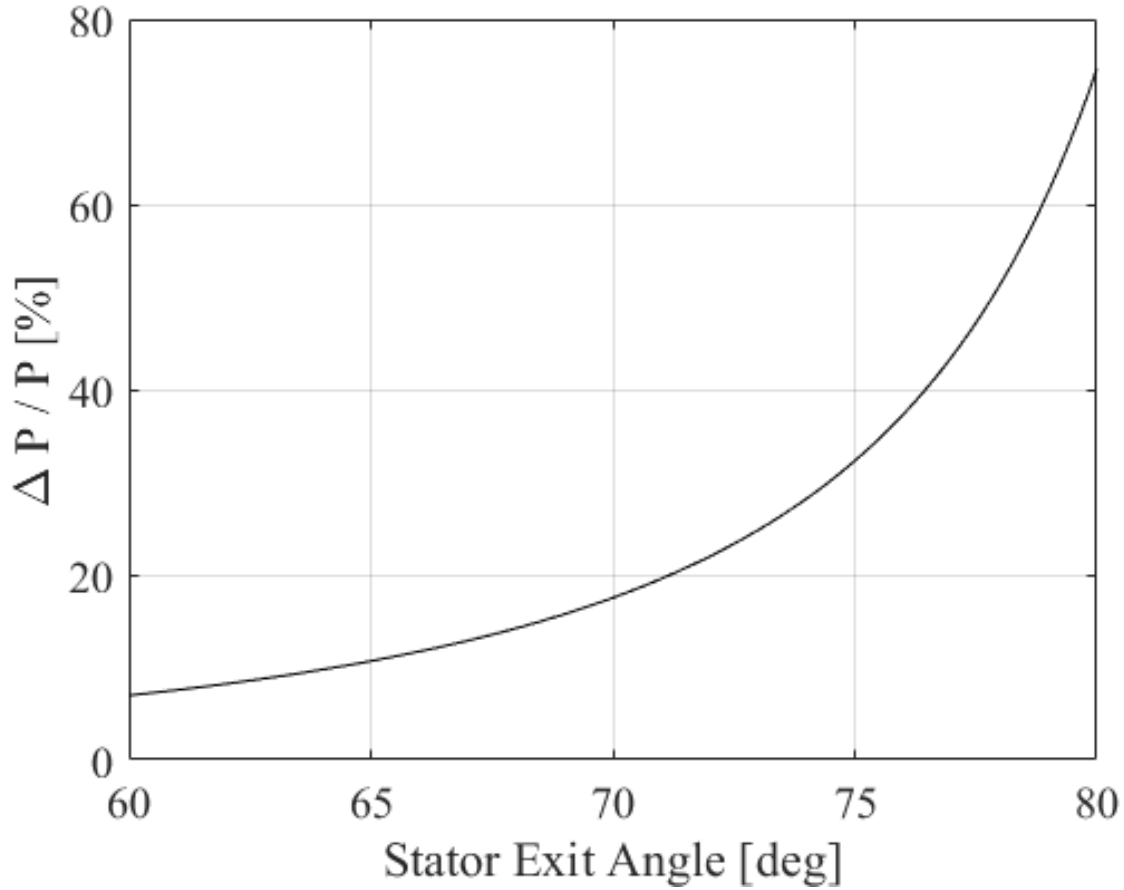


Figure 4.4. Ratio of pressure drop over the turbine to the available thermoacoustic pressure amplitude. This trend is the most strongly exponential of the three presented. The separation between 50% and 75% pressure drop over available amplitude is only 2 degrees in stator exit angle.

A turbine can be designed by selecting a desired percentage pressure drop over the turbine and correlating the selection to a stator exit angle using Fig. 4.4. Using the results of Martinez’s [21] R-218 pumping characteristics study, the desired percentage pressure drop can be correlated to an amount of power extracted from the thermoacoustic wave.

4.3 Turbine Design Case Study

Using the equations and figures developed above, a case study was performed on the design of Timmer et al. to gain understanding of typical values for the velocity vectors defined in Fig. 4.1. Figure 4.5 gives a diagram of the design used in the study.

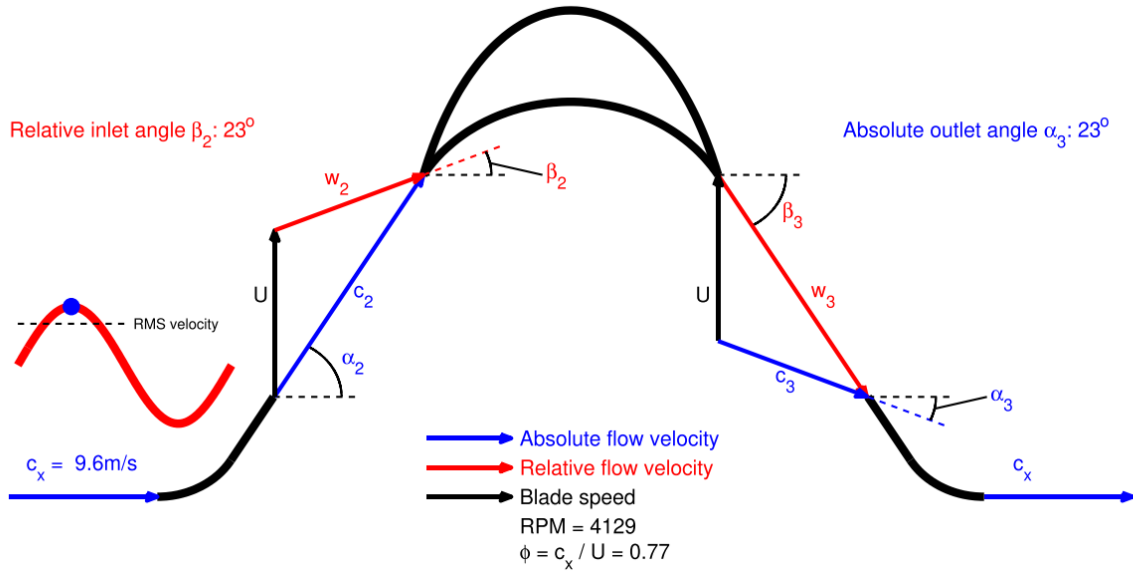


Figure 4.5. Diagram of the velocity triangles used in the design of Timmer et al. The case presented here is for the maximum fluid velocity seen by the turbine, but the case study was performed for both the maximum velocity and the RMS velocity [28].

The maximum inlet velocity, in Fig. 4.5 this is referred to as c_x , is 9.6m/s, the RMS (Root-Mean-Square) velocity is 6.11m/s, the turbine has a fixed stator exit angle of 60° and operates at $\phi = 0.77$ [28].

Table 4.1 lists the absolute value of the velocities computed for both the RMS velocity and maximum velocity reported in Timmer et al. for each station defined in Fig. 4.1 except for station 4 because station 1 and station 4 are equivalent in a bi-directional turbine. Note that $w_{\theta 3}$ is in the opposite direction of U .

Table 4.1. Timmer et al. Case Study Results

Station	Parameter	Max Value [m/s]	RMS Value [m/s]
1	c_1	9.6	6.11
2	c_2	19.20	12.21
	$c_{\theta 2}$	16.62	10.58
	w_2	10.46	6.65
	$w_{\theta 2}$	4.16	2.65
3	c_3	12.70	8.07
	$c_{\theta 3}$	8.31	5.28
	w_3	10.46	6.65
	$w_{\theta 3}$	4.16	2.65

The most important value to notice in this study is $c_{\theta 3}$, the rotor blade outlet tangential velocity, or exit swirl velocity. In the design of Timmer et al, at the RMS velocity, the on-design condition, $c_{\theta 3} \neq 0$, which means not all of the energy from the tangential motion of the fluid imparted by the turning in the stator is translated into rotor blade motion, in simpler terms, there is residual kinetic energy in the working fluid which is left unused. From this case study, it was decided that for this turbine, $c_{\theta 3}$ should be fixed at 0 in the on-design condition to avoid losing energy to flow swirl at the on-design condition.

4.4 Mechanical Design

When beginning the mechanical design of the turbine, it was determined that as many variables as possible should be bounded within the range of previously demonstrated and published turbines to allow meaningful comparisons to be made between this turbine, intended to be used with transcritical fluids, and other turbines which were used in gaseous flow environments. The turbine tip radius was fixed to 30mm, which is similar to the 29mm in Timmer et al. [28]. The number of blades was selected to be 29, the same as Timmer et al. and a prime number, which avoids any symmetries in rotation. A 2 1/2" schedule 40 pipe was selected to house the turbine as it is the closest pipe size to the turbine which

allows some clearance for both turbine shrouding and seating within the tube. The ratio of hub-to-tip radii was set to 0.7, similar to both Timmer et al., and Suzuki et al. [29]. With this set of parameters, the hub radius, rotor blade height, and rotor blade pitch can be determined using Eqs. 4.13 through 4.17.

Eq. 4.13 defines the hub radius.

$$r_{hub} = \frac{r_{hub}}{r_{tip}} r_{tip} \quad (4.13)$$

Using the hub-to-tip ratio and the tip radius of the turbine, blade height can be determined via Eq. 4.14.

$$b = (1 - \frac{r_{hub}}{r_{tip}}) r_{tip} \quad (4.14)$$

Knowing r_{hub} , the mean turbine diameter can also be calculated using Eq. 4.15

$$D_R = (1 + \frac{r_{hub}}{r_{tip}}) r_{tip} \quad (4.15)$$

Using D_R , blade pitch can be determined. Blade pitch is given by Eq. 4.16.

$$S_r = \frac{\pi D_R}{z} \quad (4.16)$$

Finally, chord length is defined by Eq. 4.17 as twice the blade pitch.

$$l_r = 2S_r \quad (4.17)$$

The radius of curvature and length of the stator blades, r_g and l_g , were scaled to the mean turbine diameter of 25.5mm from the work of Suzuki et al..

To define rotor blade geometry using Figs. 4.2 - 4.4, an on design condition needed to be defined. Since the thermoacoustic pressure oscillations occur in a sinusoidal fashion, it was determined that designing the turbine to the RMS fluid velocity of the chosen condition was preferable because, although it would not reach as high a power output as it would if it were designed to the maximum velocity, the turbine would be more efficient on average

over the entire operational range. This turbine is designed with an RMS freestream fluid velocity of 2.23m/s. Note that this value is not what is reported in Tab. 4.2, this is because the acceleration experienced by the fluid when flowing over the hub nosecone needs to be accounted for. Assuming fluid density is approximately constant between the freestream and the turbine, Eq. 4.18 gives the expression for computing the accelerated fluid velocity.

$$c_{1,accelerated} = c_{1,RMS} \frac{A_{tube}}{A_{annulus}} \quad (4.18)$$

Where A_{tube} is the area of the tube carrying the fluid and $A_{annulus}$ is the are of the annulus bounded by the turbine nosecone and the tube wall.

A pressure drop must also be computed to accompany the acceleration in fluid. Equation 4.19 expresses the pressure drop experienced by accelerating the fluid.

$$\Delta P_{hub} = \frac{1}{2} \rho (c_{1,accelerated}^2 - c_{1,RMS}^2) \quad (4.19)$$

Using Eqs. 4.18 and 4.19 to correct the conditions for the nosecone acceleration, the turbine on-design inlet velocity is 4.77m/s and the on-design thermoacoustic pressure amplitude availability is 677kPa (98psi). With the inlet conditions defined, Figs. 4.2 - 4.4 can be referenced to construct a turbine blade design.

Table 4.2 lists all important parameters used to define the design of the bi-directional turbine. Two designs have been developed for testing, one aimed at developing a moderate amount of power, and one aimed at developing a large amount of power, so some quantities have two entries.

Table 4.2. Fixed turbine parameters

Parameter	Value	Unit
r_{tip}	30	mm
$\frac{r_{hub}}{r_{tip}}$	0.7	-
z	29	-
b	9	mm
S_r	5.5	mm
l_r	11	mm
l_g	10.4	mm
r_g	7.45	mm
α_1	65, 75	deg
β_2	45, 62	deg
β_3	45, 62	deg
N	1630, 2834	RPM
\mathbb{P}	1064, 3221	W
c_1	4.77	m/s
P_1	677	kPa

Figures 4.1, 4.6, and 4.7 show how the parameters in Tab. 4.2 are mapped onto the geometry of this turbine.

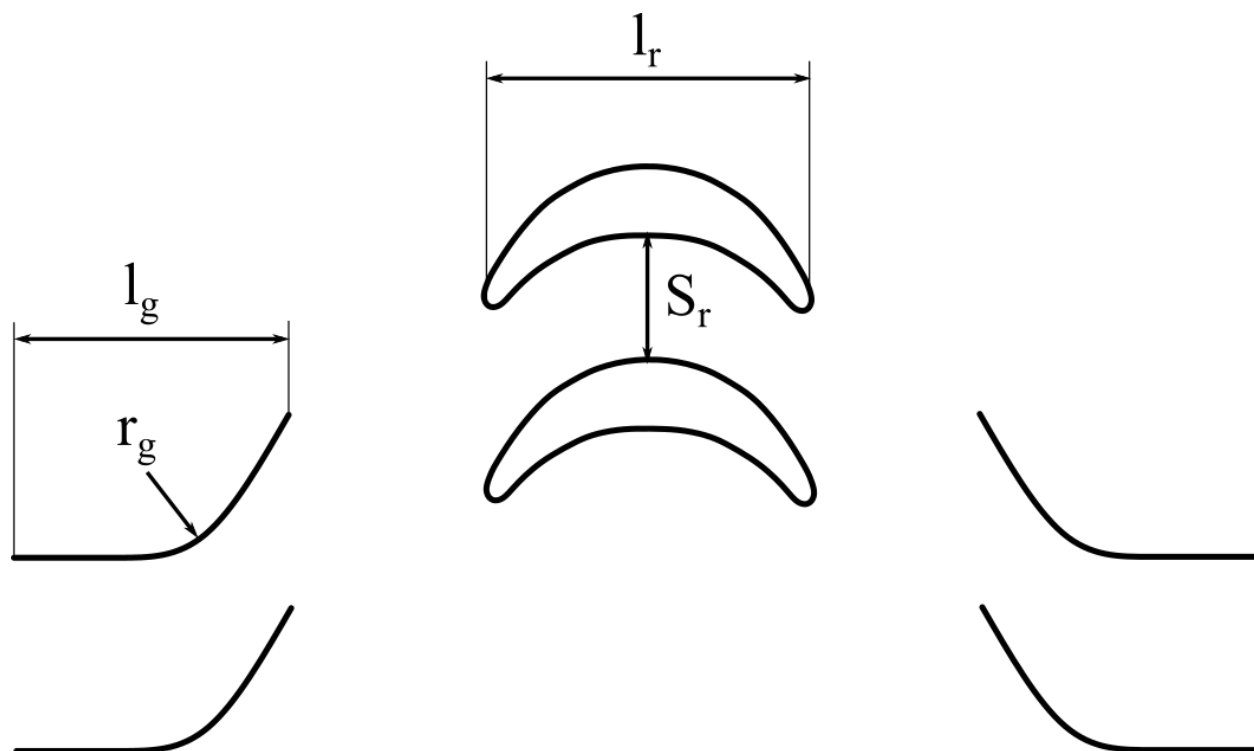


Figure 4.6. Turbine blade geometry definitions.

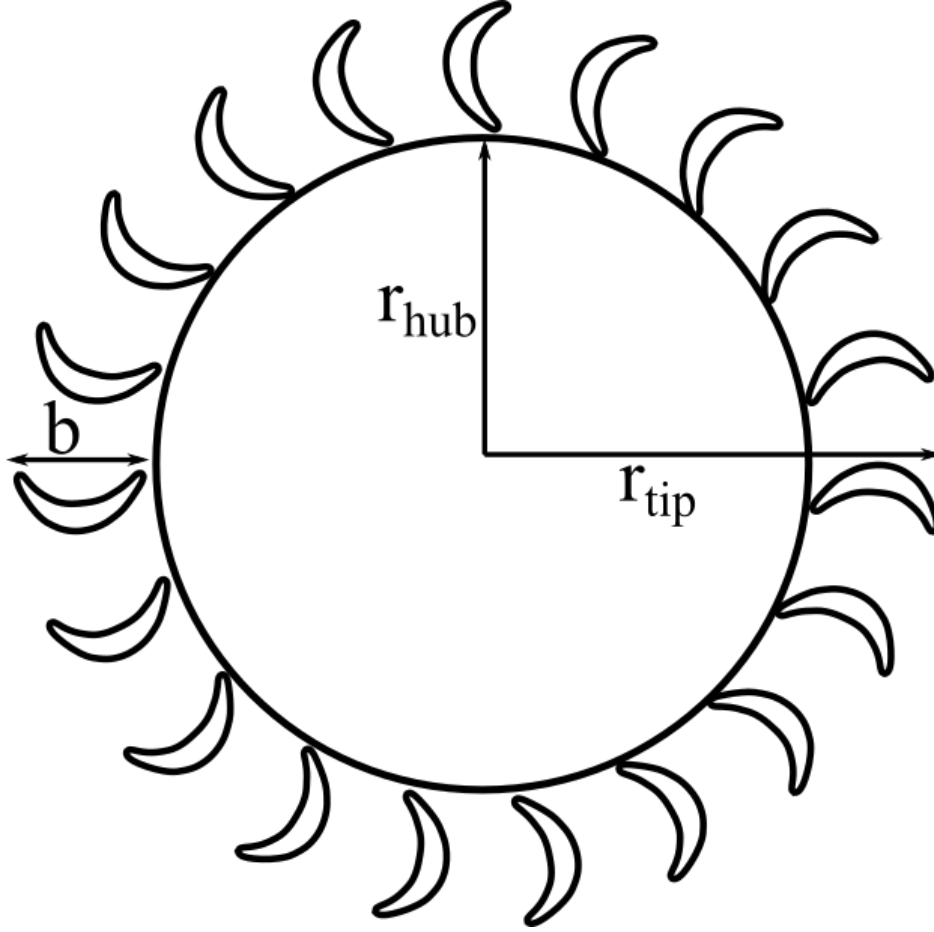


Figure 4.7. Turbine radial geometry definitions.

As stated before, two rotor designs were selected, one high performance design aimed at extracting the maximum amount of power possible without destroying the acoustic wave or creating unreasonable geometry, and one moderate performance design aimed at extracting a moderate amount of power. As listed in Tab. 4.2, the two α_1 values selected were 65 and 75 degrees. Figure 4.8 shows the moderate performance turbine assembly in both isometric and section views, and Fig. 4.9 shows the high performance turbine assembly in both isometric and section views. It should be noted that in both cases, the turbine only has one nosecone, this is a consideration made for ease of testing when characterizing the performance of these turbines. In the fully integrated design in a TTE, there will be a nosecone on each side of the turbine.

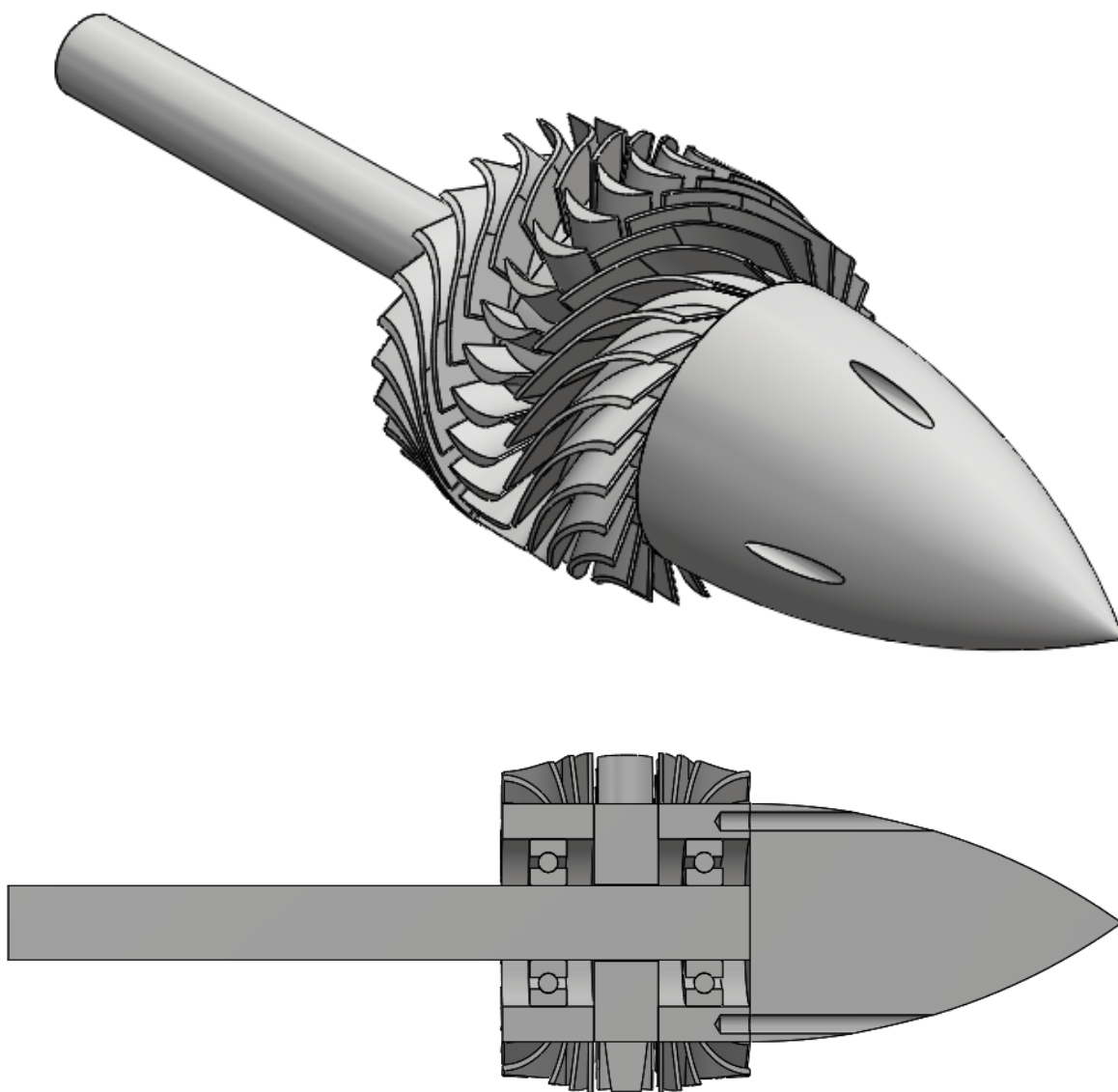


Figure 4.8. Moderate performance turbine design with $\alpha_1 = 65$ degrees.

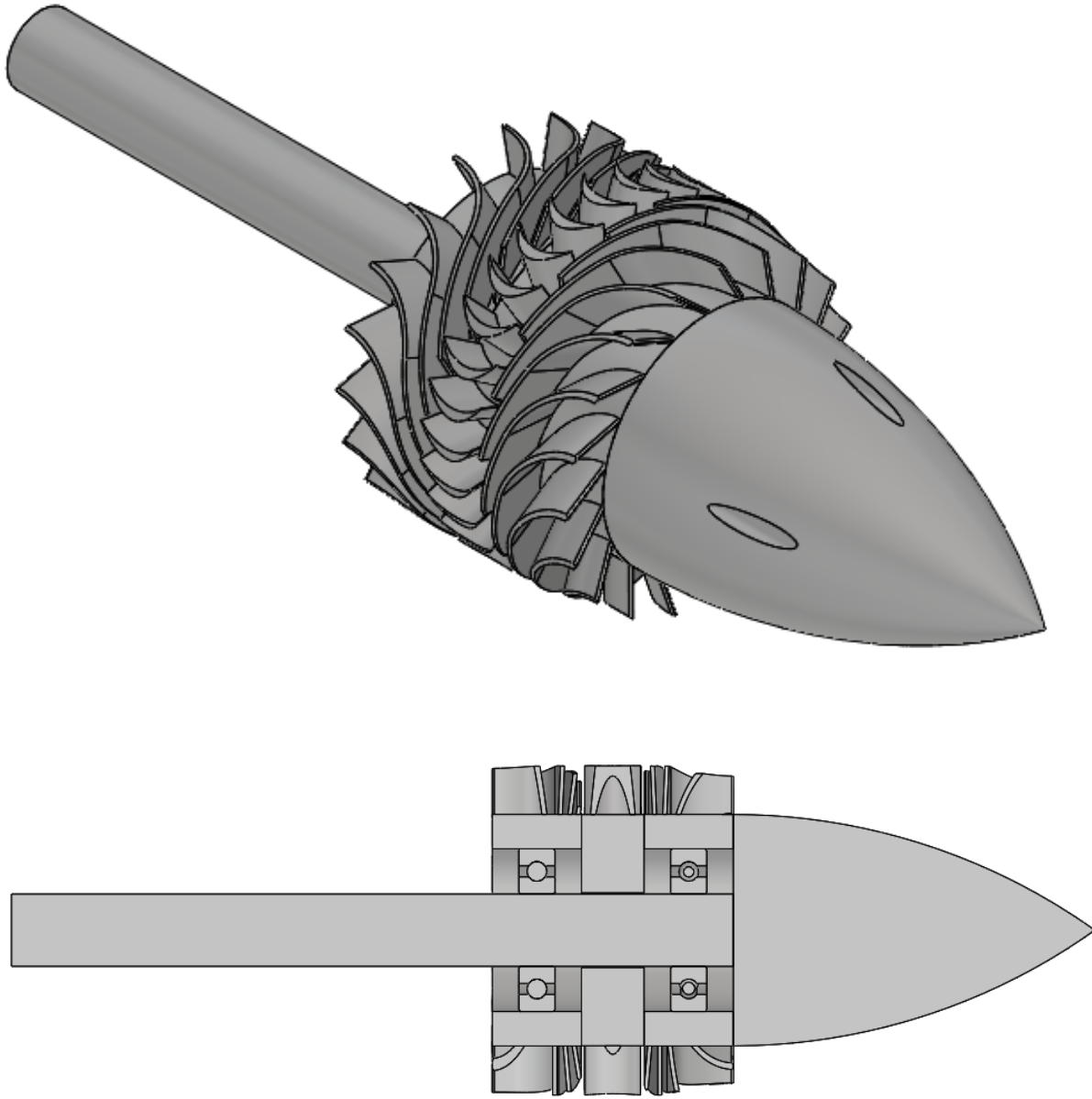


Figure 4.9. High performance turbine design with $\alpha_1 = 75$ degrees.

The power generated by each turbine can be plotted with the geometry defined. Figure [4.10](#) shows the power generated by the turbine as a function of stator exit angle with each design condition called out.

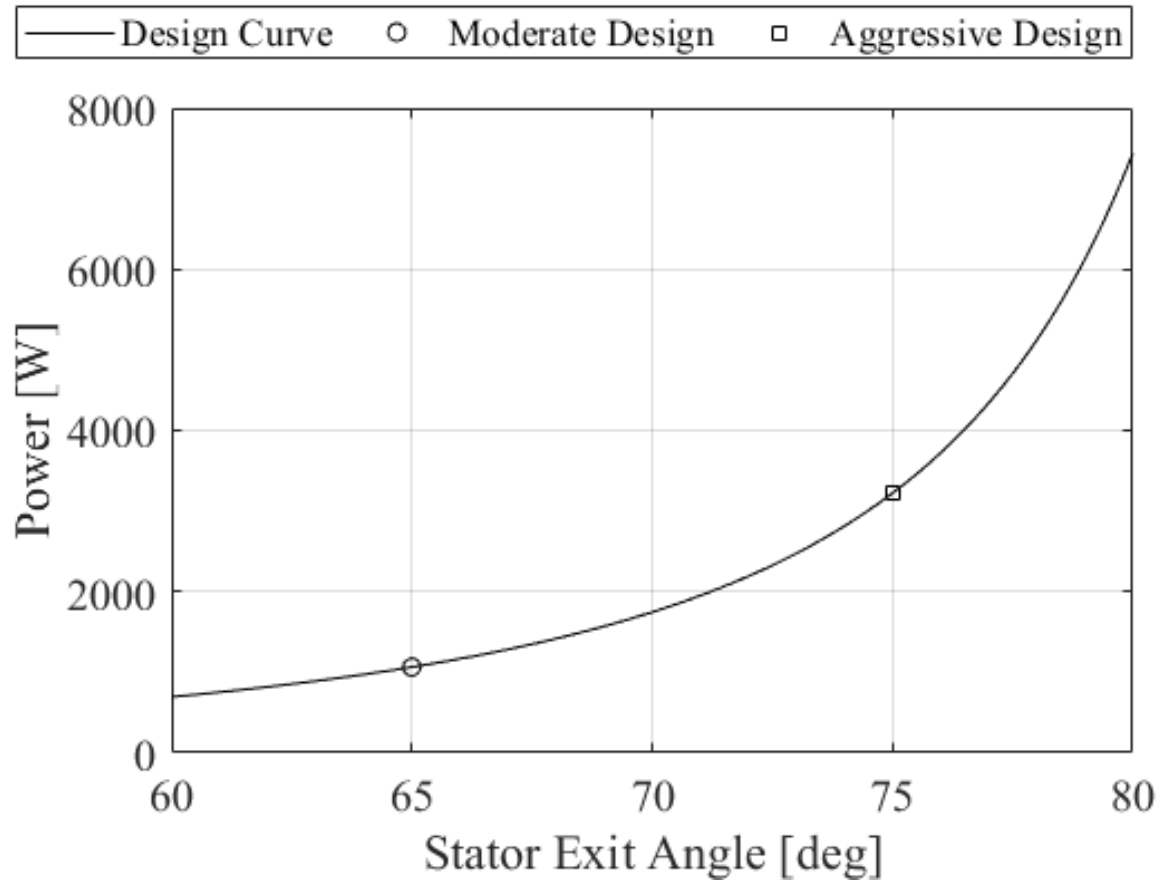


Figure 4.10. Power generated by the turbine for a 2 1/2" schedule 40 pipe and an input velocity of 4.77m/s. The high performance turbine design generates 3 times more power than the moderate performance design, but has a 3 times higher pressure drop.

Both turbine designs use trade number R8 bearings with a 1/2 inch shaft. The nosecone is a tangent ogive shape which is 1.5 times the length of the stator-rotor assembly. The nosecone is attached via 4 set screws which sit inside the holes on the face of the nosecone. The moderate performance turbine has 26 guide vanes in each stator stage, and the high performance turbine has 19. The high performance turbine has fewer guide vanes because to achieve the more aggressive stator exit angle, the stators need to take up more space.

4.5 Proposed Experiment

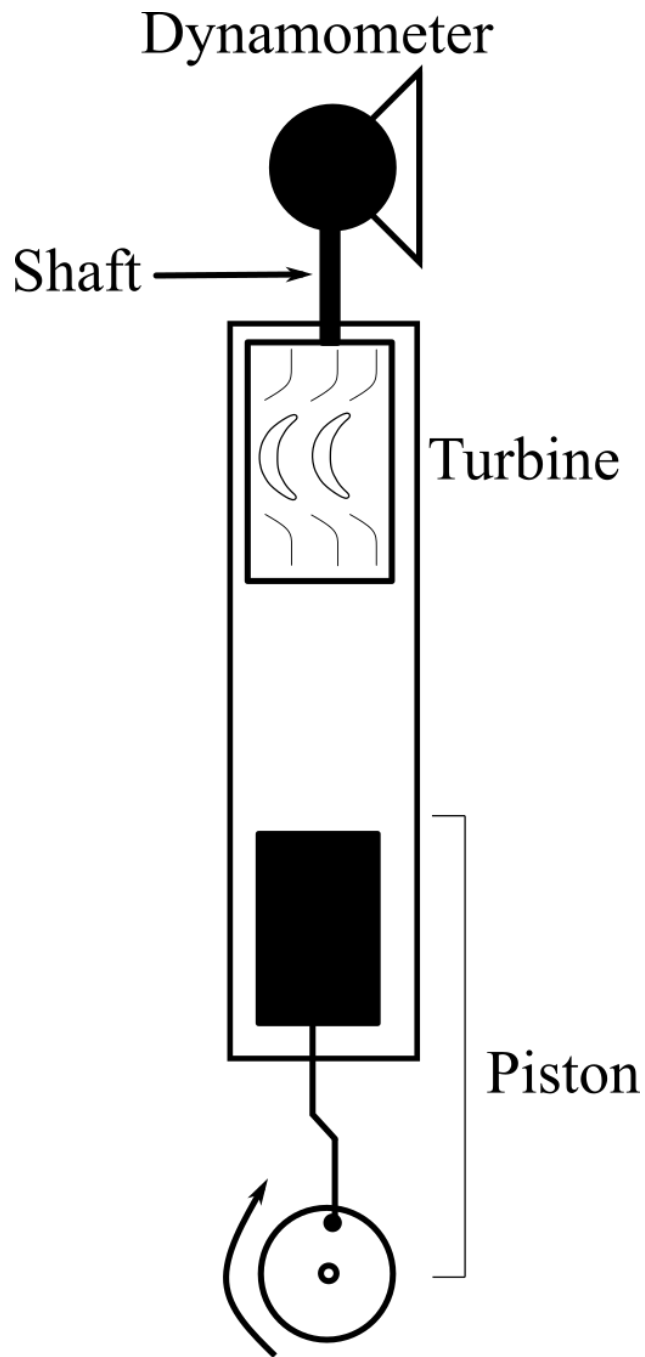


Figure 4.11. Proposed experimental design to test each turbine concept. The turbine will be installed in a tube filled with water, a piston will be used to simulate thermoacoustic pressure fluctuations, and a dynamometer will be used to measure the torque and speed of the shaft.

Figure 4.11 shows the experiment which will be designed to test each turbine concept. A clear plastic pipe will be outfitted with a piston on one end and the turbine will be installed at the other. The shaft of the turbine will be attached directly to the dynamometer. The pipe will be filled with water to simulate R-218.

To simulate thermoacoustic oscillations, the piston will push the water back and forth at a prescribed frequency and wavelength depending on the length of the tube and the piston control. Video will be taken of the turbine rotating through the clear tube and speed and torque measurements will be taken via the dynamometer. It would be ideal to test the turbine in both its on-design condition and a variety of off-design conditions, given that over its life, the turbine will be operating in off-design conditions most of the time.

5. CONCLUSION

The aim of this research was to verify the repeatability of Martinez’s results, develop understanding of the effects of resonator geometry on thermoacoustic production, and to design a power extraction device for testing and eventual integration into the TTE. These objectives were met, it was confirmed that Martinez’s results on characterizing the thermoacoustic response of R-218 were repeatable to a reasonable degree of accuracy, the effects of both resonator length and diameter on the thermoacoustic production of R-218 were characterized, and the influence of coils in the resonator section was investigated. Finally, two bi-directional turbine concepts and an experiment with which to test them were created. In section 5.1 a brief summary of experimental results obtained and a summary of the turbine design is presented, in section 5.2, suggestions for future research on the TTE technology is discussed, and in section 5.3, a brief discussion on lessons learned and suggestions for future improvements to the experiment are laid out.

5.1 Project Summary

Two major projects were undertaken over the part year. One was to use the current TTE to verify that Martinez’s results were repeatable and to investigate the effects of resonator geometry and the influence of coils on thermoacoustic production in the TTE. The second was to design a bi-directional impulse turbine for power extraction from the TTE.

5.1.1 Testing Results

The repeatability of Martinez’s results was investigated. 22 tests were carried out with $\frac{P}{P_{cr}}$ ranging from 0.9 to 1.1 and ΔT ranging from 79 to 120K. It was found that $\frac{P}{P_{cr}}$ varied from Martinez’s reported condition by an average of 1.4%, and ΔT varied an average of 0.68%. The pressure amplitude recorded varied by an average of 16.6% and the frequency by an average of 8.6%. The large percentage variation in pressure amplitude can be attributed to the inaccuracy of the Kulite pressure transducer which was used to measure maximum

pressure amplitude. Although the percentage variation is large, the frequency only varied by approximately ± 0.4 - 0.5 Hz and pressure amplitude varied by ± 40 - 80 kPa.

Next, a study investigating the effects of resonator geometry were performed. Resonator length was varied between 55.88 and 177.8cm, resonator diameter was varied between 0.457 and 0.704cm, and coils were removed from the resonator section. Measurements show increasing diameter increases frequency and decreases pressure amplitude and increasing length increases pressure amplitude and decreases frequency. It was observed, however, that these trends were not linear. The non-linear trend can be explained by three different mechanisms. One, engine geometry and fluid performance are strongly coupled in thermoacoustic devices and this parametric study does not capture all of the variable interactions happening when changing geometry. Two, increasing the diameter of the resonator significantly increases the mass of R-218 in the system, a larger mass of fluid requires more thermal energy to excite a thermoacoustic response. Three, varying the diameter of the resonator also changes the ratio of $\frac{A_{res2}}{A_{res3}}$ which modifies the pressure drop experienced across this area change. Using data obtained throughout this study, the effects of coils on the thermoacoustic production in the TTE can also be inferred. Comparing results between Martinez's study and this study, it was determined that viscous losses incurred by flowing fluid through coils does attenuate the pressure signal by approximately 11%.

5.1.2 Turbine Design

A bi-directional turbine was designed for power extraction from the TTE. A comprehensive literature review was performed to gain understanding of the current technology. Once a knowledge base was established, several preliminary analyses were performed to develop curves which could be used to design a turbine based on inlet conditions and desired power output. Two designs were created, one moderate design to extract a small amount of power, and one aggressive design to extract a large amount of power. To characterize the performance of these turbines, an experiment was proposed using water as a simulant for R-218. The water will be housed in a clear PVC pipe and oscillations in the water will be driven by

a piston at one end of the pipe. The turbine will be installed at the other end of the pipe and the shaft will be attached to a dynamometer to measure power output.

5.2 Future Work

5.2.1 Bi-Directional Turbine Testing

The most pressing work which still needs to be performed is the manufacture and test of the two bi-directional turbine designs. To mature the TTE technology enough to be used in practical applications, a reliable and efficient power extraction device needs to be designed. The current, first iteration design of the turbine is the first step into developing that power extraction device. The experiment concept needs to be fleshed out with technical details, drawings, and material requirements. Using data from the characterization of the turbine, design changes to optimize its performance should be suggested, and, once sufficiently optimized, the turbine should be integrated into a new, larger TTE, and tested with thermoacoustically responding R-218 as the working fluid.

5.2.2 Direct Measurement of Acoustic Power

Another study which would be useful for the development of the TTE is a direct experimental investigation into the acoustic power developed by the rig in various geometric configurations. It has been shown that the rig is flexible, it can excite thermoacoustic instabilities in various resonator length and diameter configurations, and the removal of coils from the resonator section has been shown to increase pressure amplitude.

A new experiment with the TTE could add measurements for both flow velocity inside the resonator section and heat required to sustain thermoacoustic instabilities. Using these measurements, a map of acoustic power generated in various geometric configurations could be produced and used to inform future designs and tune the predictive model created by Migliornio and Scalo [33].

5.3 Lessons Learned

In future experiments, several procedure and hardware changes could be made to improve testing process efficiency and allow for better measurement and analysis of the physics of the TTE.

Issues were encountered with heat exchanger sealing, as discussed earlier. In future iterations of the TTE, a new heat exchanger should be designed both to optimize its performance and improve its sealing ability. When under a high heat load from the Duratherm G, the seal on the heat exchanger tended to weaken and leak.

If more data is desired from the current TTE, or if the same instrumentation is to be used in the future, the cable for DPT-TA-05 needs to be replaced, and DPT-TA-06 itself needs to be inspected for damage as both instruments provided unreliable measurements in testing.

If more data is desired on the influence of coils or on the effects of geometry on the TTE, the experiment should be modified so that it lays horizontally, this would eliminate the effects of gravity on the TTE and could provide a more complete picture of the physical phenomena in the TTE.

REFERENCES

- [1] B. Higgins, “On the sound produced by a current of hydrogen gas passing through a tube,” *Journal of natural philosophy, chemistry and the arts*, vol. 1, no. 129, p. 2, 1802.
- [2] C. J. Lawn and G. Penelet, “Common features in the thermoacoustics of flames and engines,” *International Journal of Spray and Combustion Dynamics*, vol. 10, no. 1, pp. 3–37, Mar. 2018, ISSN: 1756-8277, 1756-8285. DOI: [10.1177/1756827717743911](https://doi.org/10.1177/1756827717743911). [Online]. Available: <http://journals.sagepub.com/doi/10.1177/1756827717743911>.
- [3] C. Sondhauss, “Ueber die Schallschwingungen der Luft in erhitzten Glasröhren und in gedeckten Pfeifen von ungleicher Weite,” *Annalen der Physik und Chemie*, vol. 155, no. 1, pp. 1–34, 1850, ISSN: 00033804, 15213889. DOI: [10.1002/andp.18501550102](https://doi.org/10.1002/andp.18501550102). [Online]. Available: <http://doi.wiley.com/10.1002/andp.18501550102>.
- [4] N. Rott, “A simple theory of the sondhauss tube,” in *Recent Advances in Aeroacoustics*, A. Krothapalli and C. A. Smith, Eds., New York, NY: Springer New York, 1986, pp. 327–338, ISBN: 978-1-4612-9324-8 978-1-4612-4840-8. DOI: [10.1007/978-1-4612-4840-8_8](https://doi.org/10.1007/978-1-4612-4840-8_8). [Online]. Available: http://link.springer.com/10.1007/978-1-4612-4840-8_8.
- [5] P. L. Rijke, “LXXI. Notice of a new method of causing a vibration of the air contained in a tube open at both ends,” *The London, Edinburgh, and Dublin Philosophical Magazine and Journal of Science*, vol. 17, no. 116, pp. 419–422, Jun. 1859, ISSN: 1941-5982, 1941-5990. DOI: [10.1080/14786445908642701](https://doi.org/10.1080/14786445908642701). [Online]. Available: <https://www.tandfonline.com/doi/full/10.1080/14786445908642701>.
- [6] K. Matveev and F. Culick, “A study of the transition to instability in a rijke tube with axial temperature gradient,” *Journal of Sound and Vibration*, vol. 264, no. 3, pp. 689–706, Jul. 2003, ISSN: 0022460X. DOI: [10.1016/S0022-460X\(02\)01217-8](https://doi.org/10.1016/S0022-460X(02)01217-8). [Online]. Available: <https://linkinghub.elsevier.com/retrieve/pii/S0022460X02012178>.
- [7] Rayleigh, *The theory of sound*, 2nd ed. Macmillan, 1896, 504 pp.
- [8] K. Taconis, J. Beenakker, A. Nier, and L. Aldrich, “Measurements concerning the vapour-liquid equilibrium of solutions of he3 in he4 below 2.19°k,” *Physica*, vol. 15, no. 8, pp. 733–739, Sep. 1949, ISSN: 00318914. DOI: [10.1016/0031-8914\(49\)90078-6](https://doi.org/10.1016/0031-8914(49)90078-6). [Online]. Available: <https://linkinghub.elsevier.com/retrieve/pii/0031891449900786>.
- [9] J. R. Clement and J. Gaffney, “Thermal oscillations in low temperature apparatus,” in *Advances in Cryogenic Engineering*, K. D. Timmerhaus, Ed., Boston, MA: Springer US, 1960, pp. 302–306, ISBN: 978-1-4684-3101-8 978-1-4684-3099-8. DOI: [10.1007/978-1-4684-3099-8_53](https://doi.org/10.1007/978-1-4684-3099-8_53). [Online]. Available: http://link.springer.com/10.1007/978-1-4684-3099-8_53.

- [10] K. Feldman, “Review of the literature on sondhauss thermoacoustic phenomena,” *Journal of Sound and Vibration*, vol. 7, no. 1, pp. 71–82, Jan. 1968, ISSN: 0022460X. DOI: [10.1016/0022-460X\(68\)90158-2](https://doi.org/10.1016/0022-460X(68)90158-2). [Online]. Available: <https://linkinghub.elsevier.com/retrieve/pii/0022460X68901582>.
- [11] W. Marrison, “Heat-controlled acoustic wave system,” U.S. Patent 2836033A, May 27, 1958.
- [12] N. Rott, “Thermoacoustics,” in *Advances in applied mechanics*, vol. 20, Elsevier, 1980, pp. 135–175.
- [13] P. H. Ceperley, “A pistonless stirling engine—the traveling wave heat engine,” *The Journal of the Acoustical Society of America*, vol. 66, no. 5, pp. 1508–1513, Nov. 1979, ISSN: 0001-4966. DOI: [10.1121/1.383505](https://doi.org/10.1121/1.383505). [Online]. Available: <http://asa.scitation.org/doi/10.1121/1.383505>.
- [14] S. Backhaus and G. W. Swift, “A thermoacoustic stirling heat engine,” *Nature*, vol. 399, no. 6734, pp. 335–338, May 1999, ISSN: 0028-0836, 1476-4687. DOI: [10.1038/20624](https://doi.org/10.1038/20624). [Online]. Available: <http://www.nature.com/articles/20624>.
- [15] R. Yang, Y. Wang, T. Jin, Y. Feng, and K. Tang, “Performance optimization of the regenerator of a looped thermoacoustic engine powered by low-grade heat,” *International Journal of Energy Research*, vol. 42, no. 14, pp. 4470–4480, Nov. 2018, ISSN: 0363907X. DOI: [10.1002/er.4192](https://doi.org/10.1002/er.4192). [Online]. Available: <http://doi.wiley.com/10.1002/er.4192>.
- [16] S. Dong, G. Shen, M. Xu, S. Zhang, and L. An, “The effect of working fluid on the performance of a large-scale thermoacoustic stirling engine,” *Energy*, vol. 181, pp. 378–386, Aug. 2019, ISSN: 03605442. DOI: [10.1016/j.energy.2019.05.142](https://doi.org/10.1016/j.energy.2019.05.142). [Online]. Available: <https://linkinghub.elsevier.com/retrieve/pii/S0360544219310242>.
- [17] J. Tan, J. Luo, Y. Wang, J. Wei, and T. Jin, “Performance of an air-cooled looped thermoacoustic engine capable of recovering low-grade thermal energy,” *International Journal of Energy Research*, vol. 44, no. 4, pp. 2682–2692, Mar. 25, 2020, ISSN: 0363-907X, 1099-114X. DOI: [10.1002/er.5034](https://doi.org/10.1002/er.5034). [Online]. Available: <https://onlinelibrary.wiley.com/doi/abs/10.1002/er.5034>.
- [18] W. Bou Nader, J. Chamoun, and C. Dumand, “Thermoacoustic engine as waste heat recovery system on extended range hybrid electric vehicles,” *Energy Conversion and Management*, vol. 215, p. 112912, Jul. 2020, ISSN: 01968904. DOI: [10.1016/j.enconman.2020.112912](https://doi.org/10.1016/j.enconman.2020.112912). [Online]. Available: <https://linkinghub.elsevier.com/retrieve/pii/S0196890420304507>.

- [19] T. Biwa, T. Watanabe, and G. Penelet, “Flywheel-based traveling-wave thermoacoustic engine,” *Applied Physics Letters*, vol. 117, no. 24, p. 243 902, Dec. 14, 2020, ISSN: 0003-6951, 1077-3118. DOI: [10.1063/5.0022315](https://doi.org/10.1063/5.0022315). [Online]. Available: <http://aip.scitation.org/doi/10.1063/5.0022315>.
- [20] D. Alexander, “Experimental study of a standing-wave transcritical thermoacoustic device,” PhD thesis, Purdue University, Aug. 2018.
- [21] A. Martinez, “Experimental study of a low-frequency thermoacoustic device,” PhD thesis, Purdue University, Nov. 25, 2019. [Online]. Available: https://hammer.figshare.com/articles/EXPERIMENTAL_STUDY_OF_A_LOW-FREQUENCY_THERMOACOUSTIC_DEVICE/10292951/1.
- [22] P. A. P. Justino and A. F. de O. Falc~ao, “Rotational speed control of an OWC wave power plant,” *Journal of Offshore Mechanics and Arctic Engineering*, vol. 121, no. 2, pp. 65–70, May 1, 1999, ISSN: 0892-7219, 1528-896X. DOI: [10.1115/1.2830079](https://doi.org/10.1115/1.2830079). [Online]. Available: <https://asmedigitalcollection.asme.org/offshoremechanics/article/121/2/65/434937/Rotational-Speed-Control-of-an-OWC-Wave-Power>.
- [23] (2019). Wavenergy.it s.r.l., Wavenergy, [Online]. Available: <https://www.wavenergy.it/about/>.
- [24] R. Soltanmohamadi and E. Lakzian, “Improved design of wells turbine for wave energy conversion using entropy generation,” *Meccanica*, vol. 51, Nov. 2015. DOI: [10.1007/s11012-015-0330-x](https://doi.org/10.1007/s11012-015-0330-x).
- [25] C. A. Velez, “Cfd analysis of a uni-directional impulse turbine for wave energy conversion,” PhD thesis, University of Central Florida, 2011, 93 pp.
- [26] T. Setoguchi and M. Takao, “Current status of self rectifying air turbines for wave energy conversion,” *Energy Conversion and Management*, vol. 47, no. 15, pp. 2382–2396, Sep. 2006, ISSN: 01968904. DOI: [10.1016/j.enconman.2005.11.013](https://doi.org/10.1016/j.enconman.2005.11.013). [Online]. Available: <https://linkinghub.elsevier.com/retrieve/pii/S0196890405003158>.
- [27] K. de Blok, P. Owczarek, and M.-X. Francois, “Bi-directional turbines for converting acoustic wave power into electricity,” p. 6, 2014.
- [28] M. A. G. Timmer and T. H. van der Meer, “Characterization of bidirectional impulse turbines for thermoacoustic engines,” *The Journal of the Acoustical Society of America*, vol. 146, no. 5, pp. 3524–3535, Nov. 1, 2019, Publisher: Acoustical Society of America, ISSN: 0001-4966. DOI: [10.1121/1.5134450](https://doi.org/10.1121/1.5134450). [Online]. Available: <https://asa.scitation.org/doi/full/10.1121/1.5134450>.

- [29] M. Suzuki, M. Takao, E. Satoh, S. Nagata, K. Toyota, and T. Setoguchi, “Performance prediction of OWC type small size wave power device with impulse turbine,” *Journal of Fluid Science and Technology*, vol. 3, no. 3, pp. 466–475, 2008, ISSN: 1880-5558. DOI: [10.1299/jfst.3.466](https://doi.org/10.1299/jfst.3.466). [Online]. Available: <http://joi.jlc.jst.go.jp/JST.JSTAGE/jfst/3.466?from=CrossRef>.
- [30] S. A. Hunt, “Thermoacoustic oscillations in supercritical fluid flows,” PhD thesis, Purdue University, May 2016.
- [31] *Guide: assessing experimental uncertainty: supplement to AIAA S-071A-1999*. Reston, VA: American Institute of Aeronautics and Astronautics, 2003, 83 pp., ISBN: 978-1-56347-663-1 978-1-56347-664-8.
- [32] A. G. Martinez, B. Kuras, M. Tindaro Migliorino, C. Scalo, and S. D. Heister, “Experimental demonstration of high-amplitude thermoacoustic instabilities under transcritical temperature conditions in a standing-wave device,” in *AIAA Scitech 2021 Forum*, VIRTUAL EVENT: American Institute of Aeronautics and Astronautics, Jan. 11, 2021, ISBN: 978-1-62410-609-5. DOI: [10.2514/6.2021-1175](https://doi.org/10.2514/6.2021-1175). [Online]. Available: <https://arc.aiaa.org/doi/10.2514/6.2021-1175>.
- [33] M. T. Migliorino and C. Scalo, “Real-fluid effects on standing-wave thermoacoustic instability,” *Journal of Fluid Mechanics*, vol. 883, A23, Jan. 25, 2020, ISSN: 0022-1120, 1469-7645. DOI: [10.1017/jfm.2019.856](https://doi.org/10.1017/jfm.2019.856). [Online]. Available: https://www.cambridge.org/core/product/identifier/S0022112019008565/type/journal_article.
- [34] D.-Y. Peng and D. B. Robinson, “A new two-constant equation of state,” *Industrial & Engineering Chemistry Fundamentals*, vol. 15, no. 1, pp. 59–64, Feb. 1976, ISSN: 0196-4313, 1541-4833. DOI: [10.1021/i160057a011](https://doi.org/10.1021/i160057a011). [Online]. Available: <https://pubs.acs.org/doi/abs/10.1021/i160057a011>.
- [35] A. J. Glassman, “NASA SP-290 turbine design and application,” *NASA Special Publication*, vol. 290, 1972.
- [36] S. D. Heister, W. E. Anderson, T. Pourpoint, and J. Cassady, *Rocket propulsion*, First edition. New York: Cambridge University Press, 2018, ISBN: 978-1-108-42227-7.

A. APPENDIX

Printed: 3/10/2021

Transcritical Thermoacoustic Engine Test Procedures

Last Updated 3/10/2021



Zucrow Laboratories - Combustion Lab (ZL1-102)

Rolls-Royce Transcritical Thermoacoustic Engine Project

PROJECT: _____

DATE: _____

TEST CONDUCTOR: _____

PROJECT ENGINEER: _____

TEST OPERATOR(S): _____

DATA SYSTEM OPERATOR: _____

TC Test Conductor: In charge of all aspects of the test. Directs test operations through use of the test procedures.

TOP Test Operator: Performs all test stand related activities associated with loading propellants and pressurant gases. Receives instructions from the Test Conductor during operation of the test procedures.

DSO	Data System Operator: Responsible for the installation and operability of all instrumentation and controls consistent with the requirements for each test. Operates the computer control and data acquisition system during tests.
SAF	Site Safety: Responsible for insuring all test site safety equipment is in place and functioning properly. Is responsible for keeping the site clear of unauthorized personnel during test operations.
Rec	Reclamation
Ref	Refrigerant
Iso	Isolation
PG	Pressure Gauge
PT	Pressure Transducer
TC	Termocouple
RV	Relief Valve
MV	Manual Valve
MR	Manual Regulator
RP	Reclamation Pump
RM	Refrigerant Manifold
TA	Test Article

REQUIRED PPE: Safety Glasses

Attachments: Test Data Sheet; P&ID; Instrumentation List

SECTION 1: PRE-TEST SETUP									
Step #	Action By	Operation	Test Numbers						
0. Prepare Test Area									
1.001	SAF	PUT testing sign on door							
1.002	SAF	TURN ON testing light							
1.003	TOP	VERIFY cart wheels are locked							
1.004	DSO	CONNECT transducer cable to connector 0							
1.005	TOP	VERIFY all wiring is connected correctly							
1.006	TOP	VERIFY oil bath contains enough oil to submerge oil pump and heater							
1.007	TOP	ATTACH N2 flex hose to N2 Regulator (MR-N2-01)							
1.008	DSO	TURN ON 28V DC regulated power supply							
1.009	DSO	TURN ON 12V DC regulated power supply							
1.010	DSO	PLUG IN CFM power supply							
1.011	DSO	TURN ON Computer and login (pass: Purdue_Pete)							
1.012	DSO	OPEN LabVIEW							
1.013	DSO	START LabVIEW VI (run program)							
1.014	DSO	LOAD Config (data wiring) files: datawiring_TTE_pc.xlsx & datawiring_TTE_tc.xlsx in TTE folder							
1.015	DSO	VERIFY sampling rate 2 kHz							
1.016	DSO	START acquire all to see live data							
1.017	DSO	START the GUI schematic							
1.018	DSO	if ref is unloaded: ACQUIRE zeroing data for PT_TAs by clicking ACQUIRE ZEROING DATA							
1.019	DSO	if ref is unloaded: SAVE zero data							
1.020	DSO	if ref is loaded: LOAD zero data							
1.021	DSO	VERIFY all data channels are reading properly							
1.022	TOP	VERIFY all hoses and tubes connected (per P&ID)							
1.023	TOP	VERIFY Reclamation Pump Liquid Valve (RPV-R218-01) closed							
1.024	TOP	VERIFY Reclamation Pump Gas Valve (RPV-R218-02) closed							
1.025	TOP	VERIFY Reclamation Manual Liquid Valve (MV-R218-03) closed							
1.026	TOP	VERIFY Reclamation Manual Gas Valve (MV-R218-02) closed							
1.027	TOP	VERIFY Vacuum Iso Valve (MV-R218-04) closed							
1.028	TOP	VERIFY Fill Iso Valve (MV-R218-05) closed							
1.029	TOP	VERIFY Reclaim Iso Valve (MV-R218-06) closed							
1.030	TOP	VERIFY Circulation Line Close-Off Valve (MV-R218-10) open							
1.031	TOP	VERIFY Hot Side Run Valve (MV-R218-08) open							
1.032	TOP	VERIFY Cold Side Run Valve (MV-R218-09) open							

1.033	TOP	VERIFY Pressure Isolation Valve (MV-ISO-01) open							
1.034	TOP	VERIFY Vacuum Jacket Valve (MV-VAC-01) is closed							
1.035	TOP	VERIFY all valves closed on Refrigerant Manifold (RM-R128-01, RM-R218-02, RM-R218-03, RM-R218-04)							
1.036	TOP	VERIFY Oil Direction Control Valve (DCV-OIL-01) is in direction of oil pump (handle perpendicular to incoming flow)							
1.037	TOP	VERIFY Water Supply Valve (MV-H2O-01) closed							
1.038	TOP	VERIFY N2 Iso Valve (MV-N2-02) closed							
1.039	TOP	VERIFY N2 Hammer Valve (MV-N2-03) closed							
1.040	TOP	VERIFY Nitrogen Regulator (MR-N2-01) is unloaded							
1.041	TOP	OPEN N2 Supply Valve (MV-N2-01)							
1.042	TOP	OPEN N2 Iso Valve (MV-N2-02)							
1.043	TOP	OPEN N2 Hammer Valve (MV-N2-03) (if system not already filled with refrigerant)							
1.044	TOP	IF REF ALREADY IN: SKIP to Section 2.1							
1. Vacuum Cycle									
1.100a	N/A	DO these steps if there isn't already refrigerant in the system (otherwise skip to Section 2)							
1.100b	N/A	WARNING: Vacuum pump gets hot during use							
1.100c	N/A	WARNING: Vacuum Pump may exhaust water/oil vapor until all is gone from lines							
1.100e	N/A	REFER to operation manual for oil replacement procedure if needed							
1.101	TOP	VERIFY all hoses and tubes connected (per P&ID)							
1.102	TOP	Verify Vacuum Pump is connected to Refrigerant Manifold (RM-R218-03)							
1.103	TOP	VERIFY Reclamation Pump Liquid Valve (RPV-R218-01) closed							
1.104	TOP	VERIFY Reclamation Pump Gas Valve (RPV-R218-02) closed							
1.105	TOP	VERIFY Reclamation Manual Gas Valve (MV-R218-02) closed							
1.106	TOP	VERIFY Reclamation Manual Liquid Valve (MV-R218-03) closed							
1.107	TOP	PLUG IN extension cord							
1.108	TOP	PLUG IN Vacuum Pump							
1.109	TOP	VERIFY exhaust cap removed							
1.110	TOP	CHECK oil level on vacuum pump							
1.111	TOP	FILL if low (should fill half of sight glass while running)							
1.112	TOP	TURN ON Vacuum Pump							
1.113	TOP	OPEN Vacuum Valve (RM-R218-03)							
1.114	TOP	RUN Vacuum Pump for about 1 minute to warm up							
1.115	TOP	OPEN Low Pressure Valve (RM-R218-01)							
1.116	TOP	OPEN High Pressure Valve (RM-R218-02)							
1.117	TOP	OPEN Reclamation Valve (RM-R218-04)							
1.118	TOP	CLOSE Reclamation Valve (RM-R218-04) after vacuuming for a few seconds							
1.119	TOP	OPEN Vacuum Iso Valve (MV-R218-04)							

1.120	TOP	OPEN Reclaim Iso Valve (MV-R218-06)							
1.121	TOP	OPEN Fill Iso Valve (MV-R218-05)							
1.122	TOP	IF Test Article Seal Was Broken: Open MV-ISO-01, MV-R218-08, MV-R218-09, MV-R218-10							
1.124	TOP	VACUUM until vacuum is reached (30 in Hg) on Low Pressure Gauge (PG-R218-05)							
1.125	TOP	VERIFY instrumentation is reading correct values							
1.126	TOP	CLOSE Reclaim Iso Valve (MV-R218-06)							
1.127	TOP	CLOSE Fill Iso Valve (MV-R218-05)							
1.128	TOP	CLOSE Vacuum Valve (RM-R218-03)							
1.129	TOP	CLOSE Low Pressure Valve (RM-R218-01)							
1.130	TOP	CLOSE High Pressure Valve (RM-R218-02)							
1.131	TOP	TURN OFF Vacuum Pump							
1.132	TOP	UNPLUG Vacuum Pump							
2. Refill from Rec Tank									
A.201	TOP	DO these steps to refill the test article with already reclaimed refrigerant							
A.202	TOP	DO these steps AFTER the entire rig and output side of Reclamation Pump have been vacuumed							
1.201	TOP	VERIFY all hoses and tubes connected (per Fill/Vacuum P&ID)							
1.202	TOP	VERIFY all valves closed on Refrigerant Manifold							
1.203	TOP	VERIFY Reclamation Pump Liquid Valve (RPV-R218-01) closed							
1.204	TOP	VERIFY Reclamation Pump Gas Valve (RPV-R218-02) closed							
1.205	TOP	VERIFY Reclamation Manual Liquid Valve (MV-R218-03) closed							
1.206	TOP	VERIFY Reclamation Manual Gas Valve (MV-R218-02) closed							
1.207	TOP	VERIFY Vacuum Iso Valve (MV-R218-04) closed							
1.208	TOP	VERIFY Fill Iso Valve (MV-R218-05) closed							
1.209	TOP	VERIFY Reclaim Iso Valve (MV-R218-06) closed							
1.210	TOP	VERIFY Hot Side Run Valve (MV-R218-08) open							
1.211	TOP	VERIFY Cold Side Run Valve (MV-R218-09) open							
1.212	TOP	VERIFY Pressure Isolation Valve (MV-ISO-01) open							
1.213	TOP	VERIFY Nitrogen Regulator (MR-N2-01) is unloaded							
1.214	TOP	OPEN N2 Hammer Valve (MV-N2-03)							
1.215	TOP	SET Nitrogen Regulator (MR-N2-01) to loading pressure ~80psig							
1.216	TOP	VERIFY High Pressure Tube (red tube) is connected to Rec Manual Liquid Valve (MV-R218-03)							
1.217	TOP	PLUG IN Extension cord							
1.218	TOP	OPEN High Pressure Valve (RM-R218-02)							
1.219	TOP	VERIFY Reclamation Pump is Plugged in							
1.220	TOP	OPEN Rec Tank Manual Liquid Valve (MV-R218-03)							

1.221	TOP	OPEN Reclamation Valve (RM-R218-04)							
1.222	TOP	OPEN Fill Iso Valve (MV-R218-05)							
1.223	TOP	OPEN circulation line Close-Off Valve (MV-R218-10)							
1.224	TOP	OPEN Rec Pump Gas Valve (RPV-R218-01)							
1.225	TOP	OPEN Rec Pump Gas Valve (RPV-R218-02)							
1.226	TOP	TURN ON Reclamation Pump							
1.227	TOP	VERIFY differential pressures on DPTs do not exceed 150 Psi							
1.228	TOP	FILL Rig to desired pressure –150 Psi (adjust N2 pressure if needed)							
1.229	TOP	CLOSE Fill Iso Valve (MV-R218-05)							
1.230	TOP	TURN OFF Reclamation Pump							
1.231	TOP	VERIFY rig pressure increases with Nitrogen Regulator (MR-N2-01), repeat pump if not							
1.232	TOP	CLOSE Rec Pump Gas Valve (RPV-R218-01)							
1.233	TOP	CLOSE Rec Pump Gas Valve (RPV-R218-02)							
1.234	TOP	CLOSE Rec Tank Manual Liquid Valve (MV-R218-03)							
1.235	TOP	CLOSE High Pressure Valve (RM-R218-02)							
1.236	TOP	CLOSE Reclamation Valve (RM-R218-04)							
1.237	TOP	INCREASE N2 ullage pressure to test pressure (per test data sheet) (MR-N2-01)							
1.238	TOP	CLOSE N2 Hammer Valve (MV-N2-03)							
1.239	TOP	UNPLUG Reclamation Pump							
1.240	TOP	UNPLUG extension cord							
SECTION 2: ENGINE TEST									
Step #	Action By	Operation	Test Numbers						
2.100a	N/A	WARNING: Do not over pressurize Low Pressure Gauge (RM-R218-05)							
2.001	TOP	IF SECTION 1.1 & 1.2 SKIPPED: INCREASE N2 ullage pressure to match rig pressure (MR-N2-01)							
2.002	TOP	IF SECTION 1.1 & 1.2 SKIPPED: OPEN N2 Hammer Valve (MV-N2-03) slowly							
2.003	TOP	IF SECTION 1.1 & 1.2 SKIPPED: INCREASE N2 ullage pressure to test pressure (MR-N2-01)							
2.004	TOP	IF SECTION 1.1 & 1.2 SKIPPED: CLOSE N2 Hammer Valve (MV-N2-03)							
2.005	TOP	WAIT for rig cool down							
2.006	DSO	UPDATE and VERIFY test settings on test data sheet							
2.007	TOP	VERIFY all tubes and hoses connected (per P&ID)							
2.008	TOP	VERIFY Pressure Isolation Valve (MV-ISO-01) open							
2.009	TOP	VERIFY Fill Iso Valve (MV-R218-05) closed							
2.010	TOP	VERIFY Vacuum Iso Valve (MV-R218-04) closed							
2.011	TOP	VERIFY Reclaim Iso Valve (MV-R218-06) closed							
2.012	TOP	VERIFY N2 Hammer Valve (MV-N2-03) closed							

2.013	TOP	VERIFY Hot Side Run Valve (MV-R218-08) open							
2.014	TOP	VERIFY Cold Side Run Valve (MV-R218-09) open							
2.015	TOP	VERIFY Recirculation Line Close-Off Valve (MV-R218-10) open							
2.016	TOP	DO NOT RUN TEST WITH HAMMER VALVE OPEN							
2.017	TOP	VERIFY PT-TA-01, PT-TA-02, and PT-R218-01 are all reading desired test pressure							
2.018	TOP	VERIFY DPTs are reading 0 differential pressure							
2.019	TOP	If running standing wave configuration: CLOSE MV-R218-08							
2.020	TOP	If running standing wave configuration: CLOSE MV-R218-09							
2.021	TOP	PARTIALLY OPEN Water circulation Valve (MV-H20-01)							
2.022	TOP	VERIFY Water pressure does not exceed 10 psi							
2.023	TOP	MEASURE water mass flow rate using catch-and-weigh							
2.024	TOP	RECORD mass flow rate in test data sheet							
2.025	TOP	VERIFY TC-H20-01 and TC-H20-02 are reading ambient temperature							
2.026	TOP	PLUG IN Oil Heater							
2.027	TOP	VERIFY lid is placed on oil bath							
2.028	TOP	SET circuit protector to 'on' position							
2.029	TOP	PRESS power button							
2.030	TOP	SET desired temperature based on test data sheet							
2.031	TOP	SET speed to 'high'							
2.032	TOP	PRESS 'Enter' button to begin circulation							
2.033	TOP	VERIFY heating symbol and pump symbol are displayed on screen							
2.034	TOP	VERIFY TC-OIL-01 and TC-OIL-02 are reading desired temperature							
2.035	TOP	MONITOR PT-TA-01, TC-TA-01, TC-TA-02, TC-TA-03, TC-TA-04, and TC-TA-05							
2.036	TOP	When Oil temperature reaches 75 C: CLOSE Pressure Isolation Valve (MV-ISO-01)							
2.037	TOP	MONITOR DPTs to verify differential pressure does not exceed 150psid							
2.038	TOP	If differential Pressure exceeds 150 psid: OPEN Pressure Isolation Valve (MV-ISO-01)							
2.039	TOP	BEGIN data recording							
2.040	TOP	MONITOR PT-TA-01, and PT-TA-02							
2.041	TOP	If pressure increases rapidly: OPEN Cold Side Run Valve (MV-R218-09)							
2.042	DSO	SAVE .tds files onto home drive							
2.043	DSO	UPDATE test data sheet							
2.044	TOP	When testing is done: Open MV-ISO-01							
2.045	TOP	PRESS 'Enter' button on oil to stop circulation							
2.046	TOP	SET oil bath heater setting to 'OFF'							
2.047	TOP	SET circuit protector to 'off' position							
2.048	TOP	CLOSE water supply valve (MV-H20-01)							
2.049	TOP	EQUALIZE N2 pressure on N2 Regulator (MR-N2-01) To PT-TA-01							

2.050	TOP	IF LEAVING REF IN: OPEN N2 Hammer Valve slowly (MV-N2-03)							
2.051	TOP	if standing wave configuration: OPEN MV-R218-08 and MV-R218-09							
2.052	TOP	if traveling wave configuration: OPEN circulation line Close-Off Valve (MV-R218-10)							
2.053	TOP	RELIEVE N2 Regulator to (MR-N2-01) ~230 psi							
2.054	TOP	IF LEAVING REF IN: CLOSE N2 Hammer Valve (MV-N2-01)							
2.055	TOP	IF LEAVING REF IN: SKIP to Section 3.2							
SECTION 3: SHUT DOWN									
Step #	Action By	Operation	Test Numbers						
0. Reclamation Cycle									
3.001a	N/A	WARNING: Do not over pressurize Low Pressure Gauge (RM-R218-05)							
3.001	TOP	VERIFY all tubes and hoses connected (per P&ID)							
3.002	TOP	VERIFY Vacuum Iso Valve closed (MV-R218-04)							
3.003	TOP	VERIFY Fill Iso Valve closed (MV-R218-05)							
3.004	TOP	VERIFY Reclaim Iso Valve closed (MV-R218-06)							
3.005	TOP	VERIFY Hot Side Run Valve open (MV-R218-08)							
3.006	TOP	VERIFY Cold Side Run Valve open (MV-R218-09)							
3.007	TOP	VERIFY Pressure Isolation Valve (MV-ISO-01) is Open							
3.008	TOP	VERIFY circulation line Close-Off Valve (MV-R218-10) is open							
3.009	TOP	VERIFY all valves closed on Refrigerant Manifold							
3.010	TOP	PLUG IN extension cord if not already plugged in							
3.011	TOP	PLUG IN Reclamation Pump							
3.012	TOP	INCREASE N2 Regulator to equalize pressure (MR-N2-01)							
3.013	TOP	OPEN N2 Hammer Valve (MV-N2-03) slowly							
3.014	TOP	DECREASE N2 Regulator to ~ 100 psia (MR-N2-01)							
3.015	TOP	OPEN Reclamation Manual Gas Valve (MV-R218-02)							
3.016	TOP	OPEN Reclamation Pump Liquid Valve (RPV-R218-01)							
3.017	TOP	OPEN Reclamation Pump Gas Valve (RPV-R218-02)							
3.018	TOP	OPEN Reclamation Valve (RM-R218-04)							
3.019	TOP	OPEN High Pressure Valve (RM-R218-02)							
3.020	TOP	OPEN Low Pressure Valve (RM-R218-01)							
3.021	TOP	OPEN Vacuum Iso Valve (MV-R218-04) slowly							
3.022	TOP	OPEN Reclaim Iso Valve (MV-R218-06)							
3.023	TOP	VERIFY pressure doesn't exceed limit on Reclamation Pump Liquid Gauge							
3.024	TOP	TURN ON Reclamation Pump							
3.025	TOP	RECLAIM refrigerant until Rec Pump Liquid Valve (RP-R218-01) reaches 28 in Hg							

3.026	TOP	TURN OFF Reclamation Pump							
3.027	TOP	CLOSE Vacuum Iso Valve (MV-R218-04)							
3.028	TOP	WAIT a few minutes for fluid in Reclamation tank to condense							
3.029	TOP	OPEN Vacuum Iso Valve (MV-R218-04)							
3.030	TOP	TURN ON Reclamation Pump and reclaim for another 30 seconds							
3.031	TOP	TURN OFF Reclamation Pump							
3.032	TOP	CLOSE Reclamation Manual Liquid Valve (MV-R218-02)							
3.033	TOP	CLOSE Reclamation Pump Liquid Valve (RPV-R218-01)							
3.034	TOP	CLOSE Reclamation Pump Gas Valve (RPV-R218-02)							
3.035	TOP	CLOSE Reclamation Valve (RM-R218-04)							
3.036	TOP	CLOSE High Pressure Valve (RM-R218-02)							
3.037	TOP	CLOSE Low Pressure Valve (RM-R218-01)							
3.038	TOP	CLOSE Vacuum Iso Valve (MV-R218-04)							
3.039	TOP	CLOSE Reclaim Iso Valve (MV-R218-06)							
3.040	TOP	UNPLUG Reclamation Pump							
3.041	TOP	UNPLUG extension cord							
3.042	TOP	BACK OFF N2 Regulator (MR-N2-01)							
1. Rig/Instrumentation Shut Down									
3.101	TOP	VERIFY N2 Hammer Valve (MV-N2-03) closed							
3.102	TOP	UNLOAD N2 Regulator (MR-N2-01)							
3.103	TOP	VERIFY all valves closed on Refrigerant Manifold							
3.104	TOP	VERIFY MV-R218-08 and MV-R218-09 are open							
3.105	TOP	VERIFY MV-ISO-01 is open							
3.106	TOP	VERIFY MV-R218-10 is open							
3.107	TOP	SHUT OFF N2 Supply (MV-N2-01)							
3.108	TOP	REMOVE fitting from downstream side of N2 Regulator (MR-N2-01)							
3.109	TOP	INCREASE N2 Regulator (MR-N2-01) until nitrogen vented							
3.110	TOP	UNLOAD N2 Regulator (MR-N2-01)							
3.111	TOP	REPLACE fitting on downstream side of N2 Regulator (MR-N2-01)							
3.112	TOP	CLOSE N2 Iso Valve (MV-N2-02)							
3.113	TOP	RECORD current bulk pressure if leaving ref in							
3.114	DSO	STOP Acquire All on LabView VI							
3.115	DSO	CLOSE LABView VI							
3.116	DSO	CLOSE all other windows							
3.117	DSO	TURN OFF 28V DC regulated power supply							
3.118	DSO	TURN OFF 12V DC regulated power supply							

3.119	DSO	UNPLUG CFM power supply							
3.120	DSO	TURN OFF computer							
3.121	TOP	DISCONNECT wires for storage							
3.122	TOP	UNPLUG extention cord (if plugged in)							
3.123	TOP	UNPLUG oil heater							
3.124	SAF	TURN OFF testing light							
3.125	SAF	TAKE DOWN testing sign							
APPENDIX A: AS NEEDED PROCEDURES									
Step #	Action By	Operation	Test Numbers						
1. Vent and Vacuum Rec Tank and Tubes									
A.100a	N/A	WARNING: Vacuum pump gets hot during use							
A.100b	N/A	WARNING: Vacuum Pump may exhaust water/oil vapor until all is gone from lines							
A.100c	N/A	WARM UP pump before vacuuming anything (run about a minute)							
A.100d	N/A	REFER to operation manual for oil replacement procedure if needed							
A.101	TOP	VENT Rec tank of N2 using Rec Relief Valve (MV-R218-05) (Schrader Valve)							
A.102	TOP	CHECK oil level on vacuum pump; FILL if low							
A.103	TOP	VERIFY all valves closed on Refrigerant Manifold							
A.104	TOP	VERIFY all tubes and hoses connected (per P&ID)							
A.105	TOP	VERIFY Vacuum Iso Valve closed (MV-R218-04)							
A.106	TOP	VERIFY Fill Iso Valve closed (MV-R218-05)							
A.107	TOP	VERIFY Reclaim Iso Valve closed (MV-R218-06)							
A.109	TOP	TURN ON Vacuum Pump							
A.110	TOP	OPEN Ref Tank Liquid Valve (MV-R218-03)							
A.111	TOP	OPEN Ref Tank Gas Valve (MV-R218-02)							
A.112	TOP	VACUUM until vacuum (28 in Hg) is reached on Low Pressure Gauge (RM-R218-05)							
A.113	TOP	TURN OFF Vacuum Pump							
A.114	TOP	CLOSE Ref Tank Liquid Valve (MV-R218-03)							
A.115	TOP	CLOSE Ref Tank Gas Valve (MV-R218-02)							
2. Leak Check									
A.200a	N/A	DO these steps after a re-assembly and when no ref is in the system							
A.201	TOP	VERIFY N2 Regulator unloaded (MR-N2-01)							
A.202	TOP	OPEN N2 Supply Valve (MV-N2-01) if not already open							
A.203	TOP	VERIFY Pressure Isolation Valve (MV-ISO-01) is open							
A.204	TOP	VERIFY Hot Side Run Valve (MV-R218-08) is open							
A.205	TOP	VERIFY Cold Side Run Valve (MV-R218-09) open							

A.206	TOP	VERIFY Vacuum Iso Valve closed (MV-R218-04)							
A.207	TOP	VERIFY Fill Iso Valve closed (MV-R218-05)							
A.208	TOP	VERIFY Reclaim Iso Valve closed (MV-R218-06)							
A.209	TOP	VERIFY Rig Close-Off Valve open (MV-R218-10)							
A.210	TOP	DISCONNECT manifold from Vacuum Iso Valve (MV-R218-04)							
A.211	TOP	DISCONNECT N2 hose from N2 line							
A.212	TOP	CONNECT N2 hose to Vacuum Iso Valve (MV-R218-04)							
A.213	TOP	OPEN Vacuum Iso Valve (MV-R218-04)							
A.214	TOP	INCREASE N2 Regulator (MR-N2-01) to desired pressure (500 psi)							
A.215	TOP	SNOOP for leaks							
A.216	TOP	FIX leaks							
A.217	TOP	BACK OFF N2 Regulator (MR-N2-01)							
A.218	TOP	CLOSE Vacuum Iso Valve (MV-R218-04)							
A.219	TOP	DISCONNECT N2 hose from Vacuum Iso Valve (MV-R218-04)							
A.220	TOP	CONNECT N2 hose to N2 Hammer Valve (MV-N2-03)							
A.221	TOP	OPEN N2 Hammer Valve (MV-N2-03)							
A.222	TOP	REPEAT steps A.209-A.211 to leak check N2 side if needed							
A.223	TOP	CLOSE N2 Supply Valve (MV-N2-01) if no longer needed							
A.224	TOP	REMOVE fitting from downstream side of N2 Regulator (MR-N2-01)							
A.225	TOP	INCREASE N2 Regulator (MR-N2-01) until nitrogen vented							
A.226	TOP	UNLOAD N2 Regulator (MR-N2-01)							
A.227	TOP	REPLACE fitting on downstream side of N2 Regulator (MR-N2-01)							
A.228	TOP	CLOSE N2 Iso Valve (MV-N2-02)							
3. Vacuum Jacket Heat Exchanger									
A.301a	TOP	DO these steps when center of heat exchanger needs to be vacuumed for insulation							
A.301b	N/A	WARNING: Vacuum pump gets hot during use							
A.301c	N/A	WARNING: Vacuum Pump may exhaust water/oil vapor until all is gone from lines							
A.301d	N/A	REFER to operation manual for oil replacement procedure if needed							
A.301	TOP	Disconnect Vacuum Pump line from Refrigerant Manifold (RM-R218-03) and connect to vacuum jacket isolation valve (MV-VAC-01)							
A.302	TOP	PLUG IN extension cord							
A.303	TOP	PLUG IN Vacuum Pump							
A.304	TOP	VERIFY exhaust cap removed							
A.305	TOP	CHECK oil level on vacuum pump							
A.306	TOP	FILL if low (should fill half of sight glass while running)							
A.307	TOP	TURN ON Vacuum Pump							

A.308	TOP	RUN Vacuum Pump for about 1 minute to warm up							
A.309	TOP	OPEN Vacuum Jacket Isolation Valve (MV-VAC-01)							
A.310	TOP	VACUUM for approximately 30 s							
A.311	TOP	CLOSE Vacuum Jacket Isolation Valve (MV-VAC-01)							
A.312	TOP	TURN OFF Vacuum Pump							
A.313	TOP	UNPLUG Vacuum Pump							
APPENDIX B: EMERGENCY PROCEDURES									
Step #	Action By	Operation	Test Numbers						
1. In Case of Vacuum Pump Oil Spill									
B.101	ALL	VERIFY oil drain fitting and oil tank cap are closed and secure							
B.102	ALL	WIPE UP oil spill with soap, water and paper towels							
B.103	ALL	DRY area to ensure oil is cleaned up							
B.104	ALL	DISPOSE OF paper towels in a trash can							
B.105	ALL	VERIFY Vacuum Pump is cleaned of oil							
B.106	ALL	VERIFY floor, hands and testet rig is clear of oil							
2. In Case of Heat Exchanger Oil Spill									
B.201	ALL	TURN OFF oil pump circulation and heat (get exact proc. For pump)							
B.202	ALL	WAIT for oil to cool down to room temperature							
B.203	ALL	WIPE UP oil spill with soap, water and paper towels							
B.204	ALL	DRY area to ensure oil is cleaned up							
B.205	ALL	DISPOSE OF paper towels in a trash can							
B.206	ALL	VERIFY floor, hands and testet rig is clear of oil							
B.207	ALL	VERIFY lid is placed on oil bath							
3. In Case of R-218 Spill									
B.301	ALL	PLUG leaks if possible (vacuum putty in control room)							
B.302	ALL	Reclaim R-218							
B.303	ALL	OPEN Exhaust Vent							
B.304	ALL	TURN ON Exhaust Fan							
B.305	ALL	STOP all leaks							
B.306	ALL	DO NOT breathe or vent R-218 if possible							
4. In Case of leak under Ref pressure									
B.301	ALL	TURN OFF oil pump circulation and heat							
B.302	ALL	CLOSE Water valve (MV-H2O-01)							
B.303	ALL	CLOSE rig close-off valve (MV-R218-10)							
B.304	ALL	OPEN Exhaust Vent							
B.305	ALL	TURN ON Exhaust Fan							

B.306	ALL	STOP all leaks							
B.307	ALL	USE vacuum putty to block leaks							
B.308	ALL	RECLAIM refrigerant							
5. In Case of R-218 Over-Pressurization (>650 psi)									
B.501	ALL	SET circuit protector to the 'o' position							
B.502	ALL	UNLOAD MV-N2-03							
B.503	ALL	VERIFY pressure in test article has equalized							
B.504	ALL	DIAGNOSE cause of over-pressurization and select appropriate path moving forward							